UNIVERSITY OF SALERNO

Department of Civil Engineering

PhD Course in

Risk and Sustainability in Civil, Architecture and Environmental Engineering Systems

XXXIII Cycle

SLOW-MOVING LANDSLIDES IN URBAN AREAS: KINEMATIC CHARACTERIZATION BY NUMERICAL MODELLING AND MULTI-SOURCE MONITORING DATA

Mariantonia Santoro

Supervisor:
Prof. Dario Peduto

Coordinator:
Prof. Fernando Fraternali

Co-Supervisor:
Dr. Eng. Giovanni Gullà

INDEX

LIST OF FIGURES

LIST OF TABLES

ABSTRACT

The slow-moving landslides, being able to develop in different geological contexts, yearly induce huge damages on structures and/or infrastructures interacting with them with consequent losses of economic nature. For this reason, studies aimed at analysing landslides and predicting the aforementioned damages are of great interest for Scientific Community and Authorities in charge of identifying the most suitable strategies for management and the land-use planning of urban areas affected by slow-moving landslides. Obviously, the carrying out of activities related to the pursuit of those objectives requires very high costs linked to the large amount of information to be acquired for the generation of landslides analysis models. In addition, the reconnaissance, mapping and analysis of kinematic features of slow-moving landslides evolving along medium-deep sliding surfaces in urban areas can be a difficult task due to the presence and interactions of/ with anthropic structures/ infrastructures and human activities that can conceal morphological signs of landslide activity. In this PhD thesis an original methodology is proposed for the kinematic characterization of slow-moving landslides in urban areas. In particular, the proposed empirical procedure is based on the full integration of conventional monitoring data (such as on-site tests and damage severity surveys) and DInSAR remote sensing data (deriving from the processing of images acquired by synthetic aperture radars installed on satellite platforms using differential interferometry techniques). This procedure was developed with reference to the case study of the historic center of Lungro (Calabria, Southern Italy). The analyzes were carried out exclusively at a *detailed scale* (on the single landslide) with a multi-scalar approach.

The results obtained highlight the potential of the proposed methodology which, thanks to a full integration of the monitoring data, allows the development of an advanced geotechnical-structural modelling useful for territorial planning and the management of urban areas affected by slow-moving landslides.

SOMMARIO

I fenomeni franosi a cinematica lenta, essendo in grado di svilupparsi in molteplici contesti geologici, annualmente causano ingenti danni su strutture e/o infrastrutture con essi interagenti con conseguenti perdite di natura economica. Per tale motivo, gli studi volti ad analizzare i fenomeni franosi e a prevedere i possibili danni sono di grande interesse per le Comunità e gli Enti impegnati nella gestione delle aree urbanizzate soggette a fenomeni franosi e all'individuazione delle più idonee strategie di pianificazione.

Ovviamente, lo svolgimento delle attività connesse al perseguimento di tali obiettivi richiede dei costi molti elevati legati alla grande quantità di informazioni da acquisire per la generazione dei modelli di analisi dei fenomeni franosi. Inoltre, in caso di fenomeni franosi medio-profondi a cinematica lenta che si sviluppano all'interno di aree densamente urbanizzate la loro ricognizione, mappatura e analisi può essere un compito difficile a causa della presenza di attività umane, che possono nascondere segni di attività franosa, e delle interazioni con edifici e/o infrastrutture.

La presente Tesi di Dottorato propone una metodologia originale per la caratterizzazione cinematica di frane con basse velocità di movimento che si sviluppano all'interno di aree urbane.

In particolare, la procedura empirica proposta si basano sull'utilizzo congiunto dei dati di monitoraggio convenzionali (quali prove in sito e rilievi della severità del danno) e dei dati di telerilevamento DInSAR (ovvero derivanti dalla elaborazione di immagini acquisite da radar ad apertura sintetica installati su piattaforme satellitari mediante tecniche di interferometria differenziale). Tale procedura è stata sviluppata con riferimento al caso studio del centro storico di Lungro (Calabria, Sud Italia). Le analisi sono state svolte esclusivamente a *scala di dettaglio* (sulla singola frana) con un approccio multi-scalare.

I risultati ottenuti evidenziano la potenzialità della metodologia di analisi proposta che, grazie ad una piena integrazione dei dati di monitoraggio, permette di sviluppare una modellazione avanzata geotecnica-strutturale utile alla pianificazione territoriale e alla gestione di aree urbane affette da fenomeni franosi a cinematica lenta.

ACKNOWLEDGEMENTS

In primis, desidero rivolgere un profondo ringraziamento al mio tutor *Prof. Ing. Dario Peduto* per la fiducia che ha riposto in me. Con la sua profonda pazienza e grande disponibilità mi ha guidato in questo lungo e tormentato percorso di studi.

In secundis, ringrazio l'Ing. Giovanni Gullà del CNR IRPI di Cosenza che mi ha permesso di affrontare e approfondire tematiche di grande originalità. Con grande professionalità mi ha supportata nei momenti di studio e di analisi più complessi.

Un ringraziamento particolare va al Prof. Ing. Settiminio Ferlisi, responsabile del Laboratorio di Geotecnica, sempre presente a rincuorare noi ragazzi con parole di conforto e incoraggiamento.

Ringrazio tutto il gruppo del Laboratorio di Geotecnica "Giuseppe Sorbino" a partire dal Prof. Ing. Leonardo Cascini, il Prof. Ing. Michele Calvello e il Prof. Ing. Sabatino Cuomo, i Tecnici, i Dottorandi e gli Assegnisti con i quali ho condiviso questa esperienza.

Ringrazio mia madre Rita, mio padre Raffaele, mio fratello Dante e mia sorella Mara per credere sempre in me ed essere sempre al mio fianco in ogni mia sfida.

Ringrazio l'Ing. Mario, collega e compagno di vita, sempre presente al mio fianco dai tempi dell'Università. In lui trovo forza, coraggio e speranza nei momenti di sconforto.

Infine, ringrazio il CNR IREA che mi ha ospitato nel mio primo anno di ricerca e tutte le belle persone che ho incontrato durante questo percorso di studi.

ABOUT THE AUTHOR

Mariantonia Santoro graduated in March 2017 in Engineering for the Environment and the Territory at the University of Salerno with 110/110 cum laude. In November 2017 she passed the admission exam to the PhD course in Risk and Sustainability in Civil, Architectural and Environment Engineering Systems (Cycle XXXIII) at the University of Salerno. In May 2020 she obtained the specialization for support activities in lower secondary school and from 2021 she teaches at the Comprehensive Institute "F.lli Linguiti" in Giffoni Valle Piana. During the PhD Course she developed her research activities on the kinematic characterization of slow-moving landslides present within urban areas. To deepen this topic, she carried out part of her study and research activities at the CNR-IREA of Naples and the CNR-IRPI of Cosenza; she attended several seminars and courses, among which the LARAM International School on "Landslide Risk Assessment and Mitigation". Some of the obtained results have been already published in the Landslides International Journal.

Mariantonia Santoro si laurea nel Marzo 2017 in Ingegneria per l'Ambiente ed il Territorio presso l'Università degli Studi di Salerno con voti 110/110 e lode. Nel Novembre 2017 supera l'esame di ammissione al Corso di Dottorato di Ricerca in Ingegneria Civile, Edile-Architettura, Ambiente e del Territorio (XXXIII Ciclo) presso l'Università degli Studi di Salerno. Nel Maggio 2020 consegue la specializzazione per le attività di sostegno nella scuola secondaria di primo grado e dal 2021 svolge attività di insegnamento presso l'Istituto Comprensivo "F.lli Linguiti" di Giffoni Valle Piana. Durante il Corso di Dottorato sviluppa ricerche incentrate sulla caratterizzazione cinematica delle frane a cinematica lenta presenti all'interno di centri urbani. Per approfondire tale tema, svolge parte delle attività di studio e ricerca presso il CNR-IREA di Napoli e il CNR-IRPI di Cosenza; segue, inoltre, numerosi seminari e corsi tra cui quello della Scuola Internazionale di Alta Formazione su "LAndslide Risk Assessment and Mitigation" (LARAM). Alcuni risultati ad oggi conseguiti, sono stati oggetto di pubblicazione su rivista internazionale Landslides.

1. INTRODUCTION

Problem statement

Landslides are very common and abundant phenomena in different areas of the world, which can represent a threat not only to private and public properties but also to human lives, with significant socio-economic losses (Brabb & Harrod,1989; Petley, 2012). Therefore, understanding the temporal and spatial evolution of landslides is of major importance for both hazard assessment and risk management that can require the design and implementation of effective prevention through adequate risk mitigation strategies (Calò et al., 2014; Guzzetti et al., 2005; VanWesten et al., 2006).
The study of landslide phenomena requires an appropriate investigation of the history of slope deformation that is possible only through appropriate modelling. A well-established methodology of analysis in the scientific literature consists of three consecutive levels: phenomenological analysis, simplified analytical analysis and advanced shear-stress analysis (Cotecchia et al, 2015). All these phases of analysis need an adequate monitoring system for a correct modelling. Such systems must ensure the availability of a wide range of historical measures of both earth surface displacement subsidence and horizontal displacement and of the levels of groundwater level in the area of interest. Multi-source conventional monitoring techniques, such as inclinometers, GPS, total stations, strain gauges and distance meters, allow the monitoring the displacements on unstable slopes (Calò et al., 2014; Angeli et al., 2000; Giordano et al., 2013; Petley et al., 2005). However, when the landslide affects very large or built-up areas, the reconnaissance,

mapping and analysis of kinematic features of slow-moving landslides evolving along sliding surfaces at medium depth can be a difficult task due to the presence and interactions of/with anthropic structures/infrastructures and human activities that can conceal morphological signs of landslide activity (Peduto et al., 2020; Gullà et al., 2017). Indeed, urbanization can limit or make it difficult the reconnaissance of geomorphological features (via both conventional image interpretation and in situ surveys) that usually help in landslide mapping (Guzzetti et al. 2012; Antronico et al. 2015; Jaboyedoff et al. 2019).

For these reasons, remote sensing techniques represent useful complementary tools for landslide monitoring (Bovenga et al. 2012; Cascini et al., 2009 and 2010; Guzzetti et al., 2009; Hilley et al., 2004). For instance, the use of images collected by space-borne Synthetic Aperture Radar (SAR) sensors and processed through Differential SAR Interferometry (DInSAR) techniques, allows overcoming constraints of conventional techniques in monitoring topographic earth surface.

Up to day, many literature contributions describe DInSAR techniques and their advantageous use for the studying the temporal evolution of ground displacements caused by different natural hazards and human activities. However, their use for the calibration and validation of geotechnical parameters used in numerical slope models is still under development.

Objectives

This PhD Thesis aims to provide a contribution to existing analysis methodologies for the kinematic characterization of slow-moving landslides in urban areas. To this end, a multi-level analytical methodology has been developed using both numerical modelling and multi-source monitoring data.

In particular, this goal is purposed through the joint use of conventional monitoring techniques (inclinometric and pluviometric data), remote sensing data (DInSAR data) and damage surveys data (available from previous studies). Indeed, all these data were used in a combined manner to calibrate and validate geotechnical model of slow-moving landslides in urban areas.
In the following, the main research questions are summarized:

- How to recognize slow-moving landslides in urban area?
- How to monitor these phenomena?
- How to model slow-moving landslides in urban areas?

In order to answer these research questions, the landslide that affect the historic center of Lungro, Calabria region (southern Italy), was chosen as a case study. This study represents a step forward compared with the state of the art as no numerical modelling is available for this landslide. Therefore the following objectives have been set:

- Multi-source landslide characterization via the combination of conventional and remote sensing monitoring data with respect to kinematics and geometry to overcome difficulties in reconnaissance and monitoring these phenomena in urban area.

- Definition of an updated landslide model based on the full integration of geological-geomorphological criteria and conventional and innovative monitoring data as well. To this end, a synergic analysis of kinematics and effects on the exposed structures was used.

- Slope stability analysis via Limit Equilibrium Method for the calibration of soil mechanical parameters: cohesion and friction angle (c and ϕ). The results obtained from these analyses were used in the subsequent FEM analysis.
- Stress-strain analysis via Plaxis software for the calibration of Young Modulus E. The results obtained from the finite element analysis were compared with innovative monitoring data (DInSAR data) and damage survey.

Thesis Outline

Chapter 2 addresses the main characteristics, the classification and the related effects of landslides and the definition of landslide risk.

Chapter 3 focuses on the conventional and innovative monitoring techniques for slow-moving landslides. DInSAR techniques are covered with a description of their basics, potential, limitations and their most relevant applications to slow-moving landslides available in scientific literature.

In Chapter 4 the methodological approach of slow-moving landslides analysis, available in the literature and articulated on several levels, is illustrated.

Chapter 5 illustrates the proposed methodology for modelling slow-moving phenomena affecting densely urbanized areas. In particular, the analyses carried out have allowed the development of a multi-level analysis methodology using monitoring and damage surveys data.

In Chapter 6, the case study of Lungro landslide (in Calabria) and the available data from previous studies are presented. Moreover, in this chapter the geomorphological and geological characterization, the conventional and innovative monitoring systems and damage survey data available in the area are illustrated.

In Chapter 7 the results of the simplified limit equilibrium analysis and the finite element modelling, that led to the development of a new kinematic model of the analysed slow-moving landslide in Lungro urban area, are described.

Finally, in Chapter 8 considerations relating to the topics discussed are set out and the possible future deepening and developments are outlined.

2. Landslide classification

2.1 Types and kinematics

Over the years, in literature various landslide definitions have been provided, which can be synthesized as follows:

• "Rapid movement of a mass of rock, residual soil or sediment, adjacent to a slope, with movement of the center of gravity of the mass itself downwards and outwards." (Terzaghi, 1950).

• "Downward and outward movement of materials (rocks and natural soils, fill materials, or combinations of several materials) forming a slope." (Varnes, 1958).

• "Movement of masses of soil or rock along a slope, resulting from shear failure at the limits of the moving mass." (Skempton & Hutchinson, 1969).

• "Transport along a slope, by gravitational action, of earthy or rocky material in bulk, along a confined area or a cut surface." (Bates & Jackson, 1987).

• "Movement of a mass of rock, soil or debris along a slope under the action of gravity." (Cruden, Varnes 1996).

The factors or causes that produce a landslide or a mass movement are different and can be divided into two factors (Cruden, Varnes 1996):

- ***Internal causes*** (that is, specific to the natural environment): nature of the ground, lithology, position, topographical trend, steepness of the slopes, climate, precipitation, thermal excursions, hydrogeology;

- ***External causes***: deforestation, rainfall, water erosion, strong winds, abundant rains, water erosion, earthquakes, anthropogenic actions.

Very often landslides are consequence of a combination of meteorological-climatic, geological and anthropic factors. Landslide phenomena can have very different characteristics as regards the material involved and the type of movement, as well as their extension and depth, and their velocity and duration. For this reason, various classification systems are proposed in the literature. The most widely used landslide classification system is the one proposed by Varnes in 1958 and subsequently revised by the same author in 1978 (Table 2.1), which basically involves the type of movement and the type of material affected by the landslide phenomenon. Varnes' classification distinguishes six type of movement namely: falls, topples, slides (rotational or translational), lateral spreads, flows and complex in the case of combination of two or more different type of movement. Then the Author differentiates three groups of involved material called "debris" (with a significant proportion of coarse material, in fact from 20% to 80% of particles are greater than 2 mm and the remaining are smaller than 2 mm), "earth" (in case of material in which 80% or more of the particles are smaller than 2 mm) and "rock" (for intact firm or hard mass and in its natural place before the origination of movement).

Movement type	Rock	Debris	Earth
Fall	1. Rock fall	2. Debris fall	3. Earth fall
Topple	4. Rock topple	5. Debris topple	6. Earth topple
Rotational sliding	7. Rock slump	8. Debris slump	9. Earth slump
Translational sliding	10. Block slide	11. Debris slide	12. Earth slide
Lateral spreading	13. Rock spread	–	14. Earth spread
Flow	15. Rock creep	16. Talus flow	21. Dry sand flow
		17. Debris flow	22. Wet sand flow
		18. Debris avalanche	23. Quick clay flow
		19. Solifluction	24. Earth flow
		20. Soil creep	25. Rapid earth flow
			26. Loess flow
Complex	27. Rock slide-debris avalanche	28. Cambering, valley bulging	29. Earth slump-earth flow

Table 2.1: Summary of Varnes' 1978 classification system (from Hungr et al., 2014).

The Varnes' classification system (1978) has been updated by Hungr et al. in 2014 to adapt it to the current knowledge and understanding of landslides phenomena (Hungr et a., 2014). It involves the type of movement and the type of material affected by the landslide phenomenon. The new version of Varnes' classification distinguishes six types of movement (Table 2.2) namely: falls, topples, slides (rotational or translational), spreads, flows and slope deformation in the case of a very slow rate of movement and the absence of a well-defined rupture surface. In addition, the Authors provide a list of materials involved in landslides (Table 2.3) based on geotechnical material terminology, as it is more useful to understand the behavior of landslides. The terms "debris" and "mud" are used to describe material modified by geomorphic processes. The names of the materials involved in the first column of the table can be used to define the names of the landslides (Hungr et al., 2014).

Type of movement	Rock	Soil
Fall	1. *Rock/ice* fall[a]	2. *Boulder/debris/silt* fall[a]
Topple	3. Rock block topple[a]	5. *Gravel/sand/silt* topple[a]
	4. Rock flexural topple	
Slide	6. Rock rotational slide	11. *Clay/silt* rotational slide
	7. Rock planar slide[a]	12. *Clay/silt* planar slide
	8. Rock wedge slide[a]	13. *Gravel/sand/debris* slide[a]
	9. Rock compound slide	14. *Clay/silt* compound slide
	10. Rock irregular slide[a]	
Spread	15. Rock slope spread	16. *Sand/silt* liquefaction spread[a]
		17. Sensitive clay spread[a]
Flow	18. *Rock/ice* avalanche[a]	19. *Sand/silt/debris* dry flow
		20. *Sand/silt/debris* flowslide[a]
		21. Sensitive clay flowslide[a]
		22. Debris flow[a]
		23. Mud flow[a]
		24. Debris flood
		25. Debris avalanche[a]
		26. Earthflow
		27. Peat flow
Slope deformation	28. Mountain slope deformation	30. Soil slope deformation
	29. Rock slope deformation	31. Soil creep
		32. Solifluction

Table 2.2: New version of the Varnes Classification system. ([a]) Movement types that usually reach extremely rapid velocities as defined by Cruden &Varnes (1996). The other landslide types are most often (but not always) extremely slow to very rapid (from Hungr et al., 2014).

Material name	Character descriptors (if important)	Simplified field description for the purposes of classification	Corresponding unified soil classes	Laboratory indices (if available)
Rock	Strong	Strong—broken with a hammer		UCS>25 MPa
	Weak	Weak—peeled with a knife		2<UCS<25 MPa
Clay	Stiff	Plastic, can be molded into standard thread when moist, has dry strength	GC, SC, CL, MH, CH, OL, and OH	I_p> 0.05
	Soft			
	Sensitive			
Mud	Liquid	Plastic, unsorted remolded, and close to Liquid Limit	CL, CH, and CM	I_p>0.05 and I_l>0.5
Silt, sand, gravel, and boulders	Dry	Nonplastic (or very low plasticity), granular, sorted. Silt particles cannot be seen by eye	ML	I_p<0.05
	Saturated		SW, SP, and SM	
	Partly saturated		GW, GP, and GM	
Debris	Dry	Low plasticity, unsorted and mixed	SW-GW	I_p<0.05
	Saturated		SM-GM	
	Partly saturated		CL, CH, and CM	
Peat		Organic		
Ice		Glacier		

Table 2.3: Landslide-forming material types (from Hungr et al., 2014).

Another widespread classification is based on the landslide movement velocity. In fact, according to Cruden and Varnes (1996), it is possible differentiate fast and slow-moving landslides. The Authors identify seven velocity classes (Figure 2.1), from extremely rapid to extremely slow, that refer to the landslide velocity and the probable destructive significance. The velocity of landslide movement depends on various factors, such as the type of the movement, the involved material and the stage of the movement.

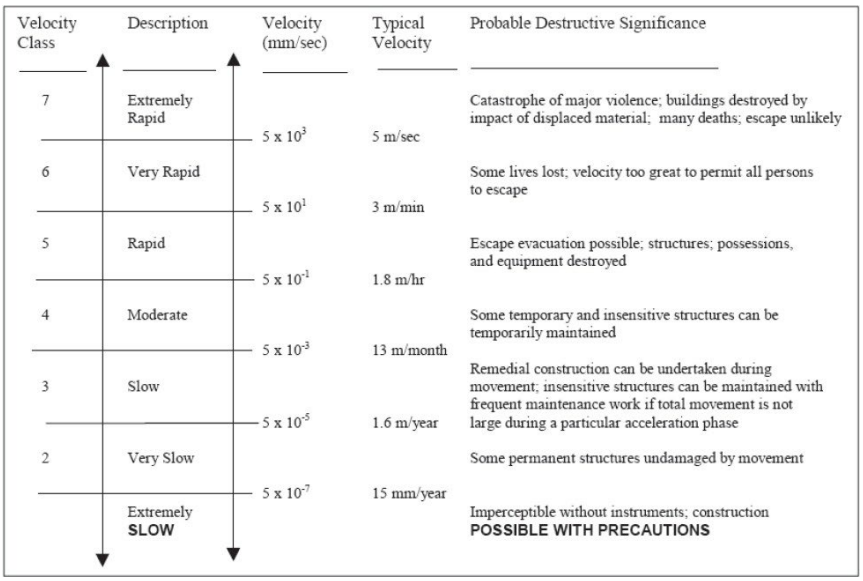

Figure 2.1: Landslide velocity classification according to Cruden and Varnes (1996)

Leroueil et al. (1996) provides a more complex classification of landslides based on the involved material type (Figure 2.2a), a 3-D matrix which refers to movement stages, materials and slope movement (Figure 2.2b) and the stage of movement (Figure 2.2c). This schematization identifies (Figure 2.2c) a pre-failure phase in which the displacement velocity increases and the material is in elastic conditions. When shear zone in the soil mass are created, the landslide phenomenon is triggered and the failure occurs.

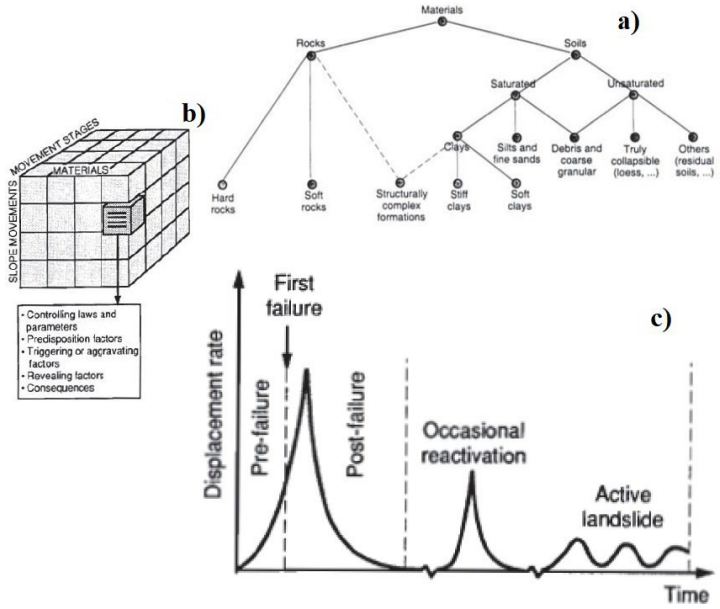

Figure 2.2: Landslide classification according to Leroueil et al. (1996).

Once these processes are completed, the soil mass moves along one or more shear zone areas that have been generated inside it until a new equilibrium configuration is identified. This phase, called post-failure, has a speed of movement that increases, until a maximum value, and then decreases. The last part of the Leroueil's diagram concerns occasional reactivations or active landslides moving along one or several pre-existing shear zones. In fact, over time, there may be extraordinary events (e.g., an anthropogenic activity) that can lead to an imbalance condition and the reactivation of the pre-existing shear bands. These occasional reactivations refer to episodic movements that are not controlled by the seasonal fluctuations of the pore-water pressures as well as by active landslides. In fact, active landslides have different displacement rate values that depend on the variation of pore-water pressures within the mobilized soil mass.

This PhD Thesis focuses on (very to extremely) slow-moving landslide with a typical velocity not exceeding 1.6 m/year (classes 1 and 2 of Cruden and Varnes (1996)'s classification). These phenomena are widespread in different geological and geomorphological contexts over the world. In the scientific literature, many slow-moving landslides are witnessed within Italian territory and they are classified as earth flows (Angeli et al, 1989; Pellegrino et al., 2004; Iovine et al., 2006), earth slides (Nicodemo et al. 2017a,b; Cotecchia, 1989; Casciniet al., 1992 a,b; 1994; Gulla et al., 2004; Tommasi et al., 2006; Comegna et al., 2013; Di Maio et al., 2018; Forte et al., 2019) and rotational-translational landslides (Cotecchia, 2006; Agostini, 2013; Antronico et al., 2013, 2014; Abolmasov et al., 2015; Gullà et al., 2017). Generally, such landslides are slow kinematic phenomena of first activation or reactivation along existing sliding surfaces with rotational, translational or complex movements.

2.2 Landslide Risk

In the present Thesis, it will be referred to the landslide risk analysis proposed by Fell et al. (2008) that is part of a wider landslide risk management process. The methodological path consists of 3 fundamental sub-processes (Figure 2.3), namely: the hazard analysis (with the aim of the landslide characterization and analysis of their frequency/annual probability of occurrence), the consequence analysis (for identifying and quantifying the elements at risk and assessing their spatial-temporal probability and vulnerability), and the risk estimation (it can be estimated in qualitative or quantitative terms, depending on the scale and the scope of work).

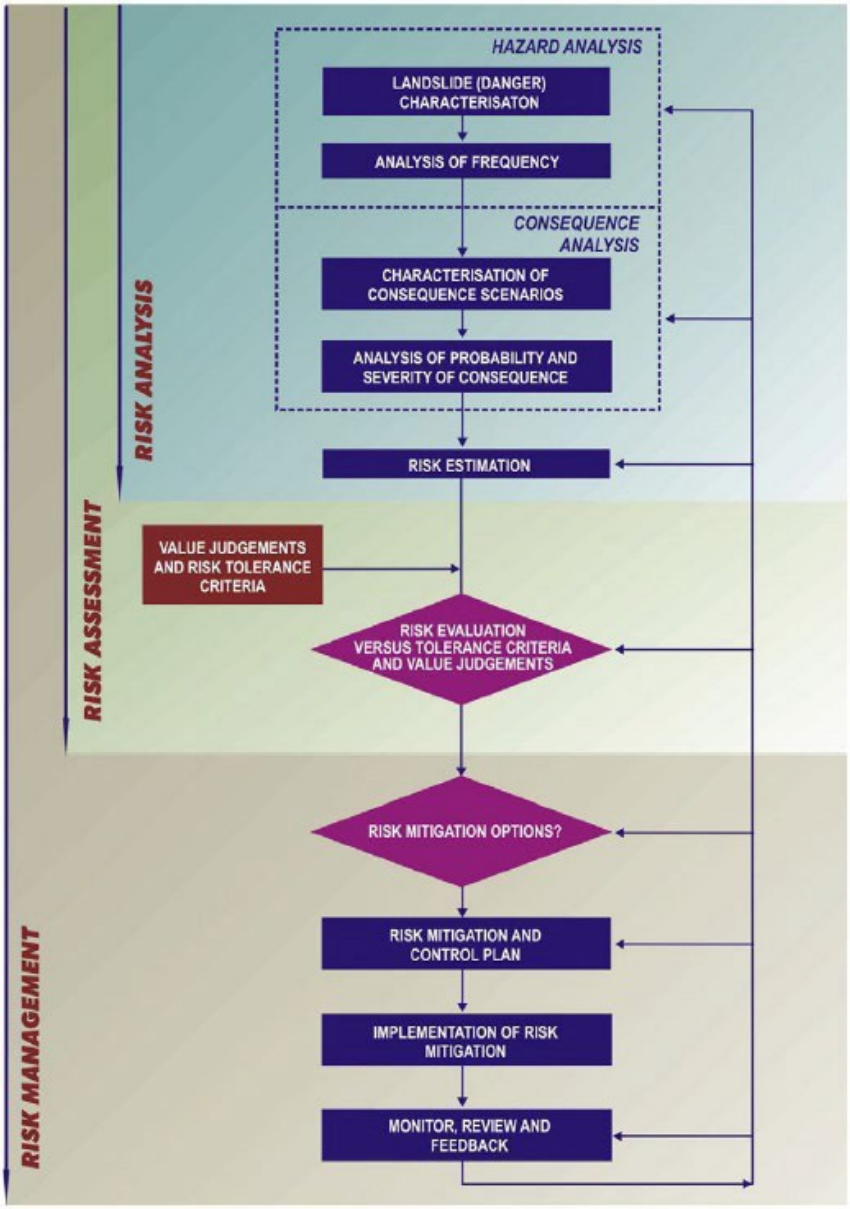

Figure 2.3: Framework for landslide risk management (from Fell et al. 2008)

The analyses carried out focus on the first phase of the Fell's framework for landslide risk management. In particular, the study aims to provide a methodology that allows the hazard analysis of slow-moving landslides in urban area.

Indeed, the results obtained may be a tool for qualitative landslide risk analysis, that according to Fell “uses word form, descriptive or numeric rating scales to describe the magnitude of potential consequences and the likelihood that those consequences will occur” (Fell et al., 2008).

Each landslide phenomenon can be associated with a risk factor that expresses the "expected damage" and depends on the "potential damage" and the probability of occurrence of a landslide phenomenon. The risk assessment can be obtained by crossing the "danger" and "potential damage" (Fell et al.,1997). The definition of risk most used in the literature is that provided by Varnes 1978 in which the risk is established as follows:

$$R = H \times V \times E$$

- ***Hazard or Danger (H)***: probability of occurrence, within a certain area and in a certain time interval, of a natural phenomenon of assigned intensity;
- ***Elements at Risk (E)***: people and / or goods (homes, structures, infrastructures, etc.) and / or activities (economic, social, etc.) exposed to “risk” in a certain area;
- ***Vulnerability (V)***: degree of loss of a certain element or groups of exposed elements "at risk", resulting from the occurrence of a natural phenomenon of assigned intensity, expressed on a scale ranging from 0 (no loss) to 1 (total loss);
- ***Total risk (R)***: expected number of victims, injured people, damage to property, destruction or interruption of economic activities, as a result of a natural phenomenon of assigned intensity.

The identification of the elements exposed to landslide risk depends on the used analysis scale (Figure 2.4). Particularly, in the case of risk analyses with a small (1:100.000) and medium (1:25.000) scale, difficulties are encountered in collecting data at the level of individual buildings and therefore the definition of a homogeneous groups of elements at risk (in terms of number of floors, type of structure, intended use, etc.) are used. Instead, in the risk analysis with a large scale (≥1:5.000) the element exposed to landslide risk coincides with the single structure interacting with the body of landslide (Pisciotta, 2008).

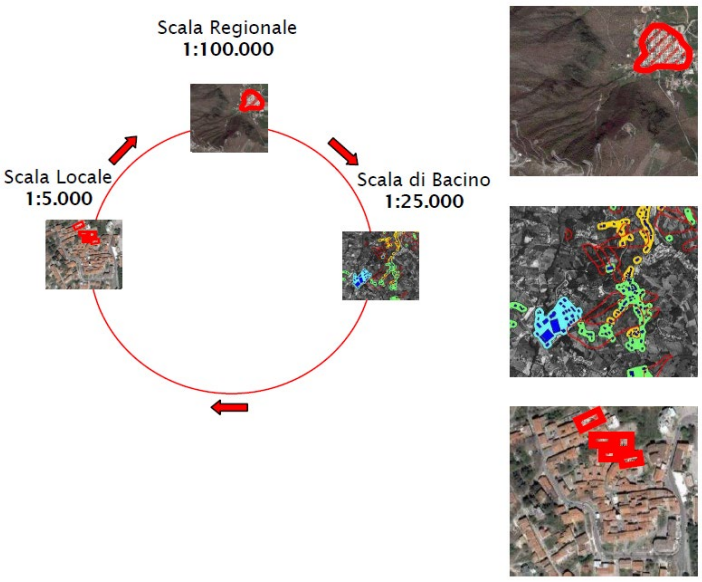

Figure 2.4: Identification of elements exposed to landslide risk a different scale (Pisciotta, 2008)

From this definition, it derives that the triggering of landslides in areas close to inhabited centers, due to their high vulnerability and elements at risk, presents a very high risk and therefore, in order to safeguard human lives, requires careful studies and continuous monitoring.

2.3 Slow-moving landslide effects

Although slow–moving landslides do not directly threaten human lives, the damage to the structures and infrastructures involves relevant economic losses for the owners and managing agencies/authorities. Slow-moving landslides cause different damage to environmental assets and cultural heritages, such as cracking and tilting of buildings (Nicodemo et al. 2017, Infante et al.,2018, Gullà et al. 2017) and cracks, dislocations and interruption of roads (Ferlisi et al, 2019; Nappo et al., 2021).

As highlighted in the "*Dissesto idrogeologico in Italia: pericolosità e indicatori di rischio"* (ISPRA, 2018) in Italy the total number of buildings at risk in areas with high and very high hazard has increased by 3.8% since 2011 and is equal to 1614 buildings (see Figure 2.5). For this reason, modelling slow–moving landslides in urban areas becomes increasingly important for hazard analyses and landslide mitigation. In the scientific literature, are several cases that have shown how the effects induced by slow-moving landslides on structures depend on the type of landslide, its intensity and the characteristics of the construction.

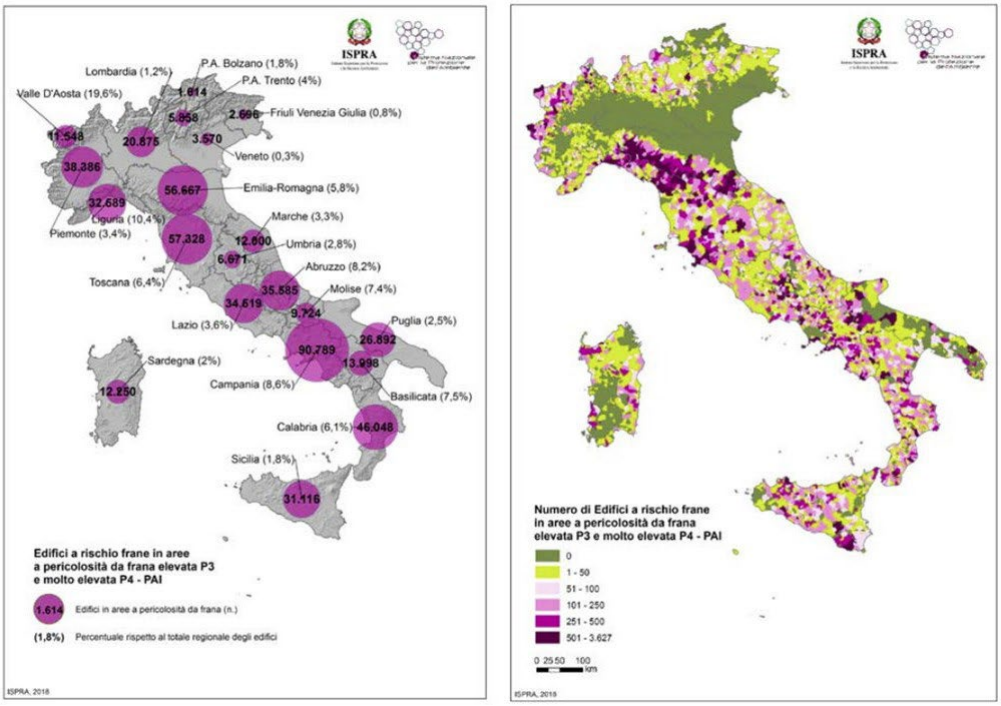

Figure 2.5: Italian buildings located in high and very high landslide hazard areas on a regional andmunicipal basis (ISPRA, 2018).

Some examples of damage to structures induced by slow-moving landslides in Italy are: the San Francesco landslide, in the little town of San Pietro in Guarano, where some public and private buildings have been evacuated as a result of instability and subsequently partially or totally demolished (Cascini et al., 2008, Viscardi et al.,2010). The case of Assisi city, located in Central Italy, where a deep-seated landslide causes damage to the town infrastructure (Calò et al., 2014). Many cases in Calabria region (southern Italy) such as in Catanzaro Province, where in February 2010 damage to buildings, infrastructure and productive activities wasrecorded (Gullà et al., 2014). The landslide in Cavallerizzo, where several buildings were damaged; the slow-moving landslides in the municipalities of Lungro (Antronico et al., 2013, 2014; Gullà et al., 2016; Peduto et al. 2020)

and Verbicaro (Nicodemo et al., 2018; Ferlisi et al., 2019, Borelli et al., 2018), which caused damages to the buildings located in the historic centres and new developed areas. The slow movements of deep and complex active landslides in the Latronico village (Di Maio et al., 2018), located within the Pollino National Park in the Italian southern Apennines, that damaged several buildings including the school and its gym, the military building, the cemetery and a water reservoir. The San Fratello landslides, in the Messina Province (South Italy), where several people were evacuated over the years and many cultural sites of the village have been destroyed (Bianchini et al., 2014). The case of Bovino town (Palmisano et al., 2014), located within the Daunia Apennines (South Italy), where the landslide activity is evident by cracks and bulging in the green field during spring and cracks and fissures visible on structures and infrastructures.

The development of these landslides within the urban areas makes it more difficult to define the boundary conditions necessary for analysis and modelling. For this reason, this PhD Thesis aims to contribute to the development of a methodological approach for slow-moving landslides modelling in urban area to support risk mitigation strategies.

3. Monitoring techniques

The modelling of slow moving landslides requires the definition of boundary conditions that can only be achieved with adequate monitoring systems. For this reason, the analysis of landslides, and therefore the risks associated with them, cannot be conducted without an adequate database of conventional and innovative monitoring data. The monitoring methods can be classified in six main categories (Calvello et al. 2017, Pecoraro, 2019):

I. *Geodetic* that allow to measure the displacements of the ground through the tracking of the distances with the GPS or the horizontal and vertical measurements of the angles.
II. *Hydrologic* to quantify the movement and the distribution of the water on and below ground level.
III. *Geotechnical* to identify ground geomorphologic evolution and provide ground displacements measurements, soil deformation data, groundwater level and total stress database in the soil.
IV. *Geophysical* to investigate physical parameters of rock or soil mass (e.g. acoustic/elastic parameters, density, resistivity, etc.) and to monitor changes in the landslide mass.
V. *Meteorological* to measure the weather parameters that may trigger a landslide (e.g., rainfall, snowmelt) and/or influence its behaviour (e.g., wind, air temperature).
VI. Remote sensing to monitor surface displacements and characterize the slope instability factors without any physical contact with the landslide mass.

In particular, the monitoring of slow moving landslides can concern several factors (e.g. displacements affecting the slope, variation of the piezometric levels, pluviometric data and damage buildings survey) that influence the instability phenomenon. However, the choice of data to be used must necessarily take into account the kinematics of the landslide and the triggering factors. In particular, with regard to the Lungro landslide, the pluviometric data were not taken into account as they are not landslides induced by rain events. In fact, being a densely urbanized area almost all the rain water stream superficially without affecting the stability of the slope. Furthermore, as the variations of the ground-water levels turnout to be limited, the studies focus on the most significant data, such as displacements measured both with conventional techniques and with SAR remote sensing.

3.1 Conventional techniques

Surface deformation measurements based on in situ research (inclinometers, levelling GPS and LIDAR) are necessary to model slow-moving landslides. These technologies allow detecting and mapping landslides for the instability study (Lollino et al., 2007).

The most traditional monitoring system to measure on-site ground displacements is the inclinometer. It is an instrument that allows to determine and measure deep deformations through the use of an inclinometric pipe placed inside a vertical inserted in the ground. These tubes can be of different diameters and materials (aluminum or pvc) depending on the characteristics of the soil in which the measurements are to be made. The inclinometer tube has four guides in correspondence of the four quadrants, which allow to orient the tube with respect to the cardinal points, allowing to carry out repeatable measurements.

Inside the inclinometer tube are present the inclinometric sensors that are composed of two servoaccelerometric sensors, placed on perpendicular planes (one parallel to the guide grooves of the tube and the other planes perpendicular to them) in order to measure angles with respect to the vertical, along the two perpendicular directions. The probes are formed by a stainless steel structure on which are mounted two trolleys with wheels, necessary to slide the sensors along the inclinometric tube and carry out the measurements. The inclinometers allow to obtain a remarkable precision, of the order of 0.01 mm / m, although it is worth pointing out that the final precision of the measurements is conditioned by a number of other factors, such as: the method of installing the column of inclinometer tubes, the measurement methods and data processing procedures. The start of the measurements must be preceded by some preliminary operations consisting of: cleaning the inclinometer tube, marking the reference guide which, generally, coincides with the one closest to the slope downstream direction, orientation with respect to the north of the downstream direction and the direction identified by the reference guide. For each measurement, at least two series of readings must be provided, the second of which is conducted by rotating the probe 180° with respect to its main axis. The reading step generally varies from 0.5 m, for shallow survey or when a high level of definition of the deformation is required, to 1.0 m, for high depths or where no particular detailed information is required. The first reading (zero reading) is necessary to use a step equal to 0.5 m. The displacement data are read and saved in real time thanks to the connection of the sensor with an electric cable to a digital portable control unit. The latter collects the measurements of the tube inclination angles with respect to the vertical projected on the two planes perpendicular to each other, multiplied by an instrumental constant ($10.000 < K < 25.000$).

The data collected shall take the form of:

$$K \cdot \sin\theta + b$$

The term b is defined as “zero offset” and represents a systematic error (different for the two directions from which the angles are measured) related to the construction defects and the loss of rectification that determines a non perfect verticality of the inclinometric tube. The unit of measurement of the displacements measured by the inclinometers is the "digit", whose conversion factor at millimeters is 0,01 mm/digit. In addition, to switch from angular values to displacements a trigonometric function $L \cdot \sin \theta$ is used, with L equal to the sensor pitch.

Another widespread technology for monitoring the movements of the Earth’s surface is that of the fixed GPS network. This technology consists of three devices powered by solar panels that ensure the operation in full autonomy and operating in single frequency. These tools are connected to each other through a GMS modem that allows the transmission of data and the reception of static session acquisition parameters. The network consists of a sensor installed within landslide body and two reference sensors located in a stable area. However, due to the operation in single frequency and logistical difficulties related to the installation of such sensors in areas subjected to concealment of the GPS network due to the presence of rocky walls, the reciprocal baselines may have a maximum length of 4 km (Lollino et al.,2005). However, if landslides occur in densely urbanised areas, on-site installation of monitoring systems is difficult to apply (Gullà et al. 2017; Peduto et al., 2020) leading to an increase in data acquisition times data and costs. For this reason, the combined use of conventional and traditional monitoring data is necessary for the modelling of slow-moving landslides in urban areas (multi source kinematic landslides characterization).

A monitoring technology that allows to overcome the limits of the on-site monitoring systems is that of the terrestrial laser scanner or LIDAR. This remote sensing technique allows to monitor geomorphological phenomena thanks to the use of infrared laser technology with very high spatial resolutions and operating both during day and night. The main advantages of LIDAR are the rapid data acquisition, the high accuracy in altimetric measurements, a wide spatial distribution of the measuring points and a vertical and horizontal resolution in the order of decimeter. This technology allows the realization of high resolution digital soil models (DTM) or the production of 3D rendering of urban areas, slopes and rocky fronts. Several scientific studies have shown the effectiveness of LIDAR technology for the construction of active slow landslide phenomena DTM (e.g. Jaboyedoff et al., 2012). In fact, through the comparison of DTM acquired in different time it is possible to identify the displacements of the soil and to determine the velocities of deformations. Generally, LIDAR data is used with two single acquisitions, before and after the event. On the other hand, studies on the Montaguto landslide (Avellino) in the period 2006-2010 have shown that a multi-temporal use of LIDAR data from airplane allows highlighting the complexity of the movement and the roto traslation mechanisms of landslides (Terranova et al., 2011).

3.2 Damage surveys

Monitoring of damage on structures and infrastructure fallig within a landslide phenomeno is an essential to study slow-moving landslide cinematics. Indeed, as reported by Fell in the framework for landslide risk management (Figure 2.3) the analysis of the consequences induced on the exposed elements is a fundamental part of the analysis of the landslide risk (Fell et al., 2008). In particular, the analysis of the consequences must include two consequential phases: the first which aims at identifying the elements exposed to risk and characterising the scenario of the consequences,

and the subsequent phase that must provide the analysis of the probability and severity of the damage. In the case of landslides in urban areas, buildings are the elements most exposed to the risk and their study requires the implementation of a suitable census with a damage classification through field surveys (Remondo et al., 2005; van Westen, 2004,2008; Nicodemo, 2017). These measurements shall be made taking into account reliable information such as the age of construction of the building, the designated use, structural and foundation typologies or the number floors and considering the scale of analysis. In fact, in the case of smaller study scales, due to the large number of buildings, it is necessary to use a grouping of buildings that must take into account their structural characteristics. The analysis of the consequences includes the definition of the vulnerability, defined as the expected degree of loss of a given element or set of elements within an area actually or potentially affected by a hazard of a given intensity (Varnes 1984; Léone et al. 1996; Guzzetti et al., 2000; Buckle et al. 2000; Remondo et al. 2008; Bonachea et al. 2009). In particular, in the case of buildings or infrastructure the vulnerability is called "physical" and depends on both the extent of the damage and the costs of reconstruction. Obviously this vulnerability is linked to many factors related to both the characteristics of the element exposed to the phenomenon and the intensity of thephenomenon.

The physical vulnerability of buildings is related to the building damage and to the types and magnitude of vertical and horizontal displacements that occur at the foundationlevel. Indeed, in the case of prevailing horizontal displacement the building can undergo extensions or support loss (Figure 3.1) leading to increased stress in some areas of the building and the formation of the first cracks at the weaker areas such as windows, corners and doors (National Coal Board, 1975; The Institution of Structural Engineers,1994).

On the other hand, if both horizontal and vertical displacements coexist, the due difference deformations may occur (Figure 3.1):

1. *Sagging*: in the case of convex bending deformation.
2. *Hogging*: deformation with concave upward bending.

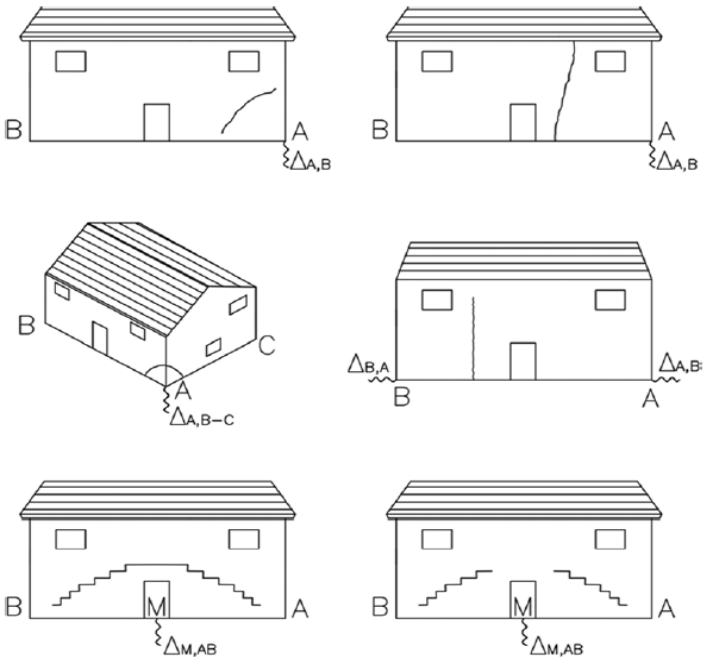

Figure 3.1: Building damage linked to different type of foundation settlements (from Plamisano et al, 2016).

In the scientific literature there are several systems of buildings damage classification that can be based on pattern of stress and damage (Audell,1996; Johnson, 2005), earthquake intensity (Wood and Neumann, 1931; Grunthal, 1998), amount of distortion of structures (NCB, 1975; Bhattachraya and Singh, 1985; Chiocchio et al., 1997) and visual building damage (Burland et al., 1977; Alexander, 1986; Van Rooy, 1989; Geomorphological Services Ltd. 1991; Humphreys and Partners, 1993; Freeman et al., 1994; Palmisano et al., 2016).

Among the visual building damage schemes the most adopted classification system is that of Burland et al. (1977). In particular, five classes (D0 = negligible, D1= very slight, D2 = slight; D3 = moderate; D4 = severe; D5 = very severe) were identified (Table 3.1) that, based on the width of cracks on building facades and their distribution as well as the easy of repair, mainly reflect the attainment of damage affecting the building aesthetics (D1–D2), causing a loss of functionality (D3) or even compromising their stability (D4–D5). As stated by the authors the classification system is based on the visible damage at a given time and it has been developed for stone masonry and brickwork.

Category of damage	Normal degree of severity	Description of typical damage
0	Negligible	Hairline cracks less than about 0.1 mm.
1	Very Slight	Fine cracks which are easily treated during normal decoration. Damage generally restricted to internal wall finishes. Close inspection may reveal some cracks in external brickworks or masonry. Typical crack widths up to 1 mm.
2	Slight	Cracks easily filled. Re-decoration probably required. Recurrent cracks can be masked by suitable lining. Cracks may be visible externally and some repainting may be required to ensure weathertightness. Door and windows may stick slightly. Typical crack width up to 5 mm.
3	Moderate	The cracks require some opening up and can be patched by mason. Repainting of external brickwork and possibly a small amount of brickwork to be replace. Door and windows sticking. Service pipes may fracture. Weathertightness often impaired. Typical crack widths are 5 to 15 mm or several up to 3 mm.
4	Severe	Extensive repair work involving breaking-out and replacing sections of walls, especially over doors and windows. Windows and door frames distorted, floor sloping noticeably[1]. Walls leaning[1] or building noticeably, some loss of bearing in beams. Service pipes disrupted. Typical crack widths are 15 to 25 mm but also depends of the number of cracks.
5	Very severe	This requires a major repair job involving partial or complete rebuilding. Beams lose bearing, walls lean badly and require shoring. Windows broken with distortion. Danger of instability. Typical crack widths are greater than 25 mm but deepens of the number of cracks.

[1] Note: Local deviation of slope, from the horizontal and vertical, of more than 1/100 will normally be clearly visible. Overall deviations in excess of 1/150 are undesirable.

Table 3.1: Classification of visible damage to walls with particular reference to ease of repair of plaster and brickwork masonry (from Burland et al., 1977)

3.3 Remote sensing techniques

Remote sensing is the science that allows to monitor the earth's surface displacement without direct contact, but processing and analysing the reflected and emitted energy (Lillesand and Kiefer, 1987). This is achieved by sensor on satellites (space borne) or using aircraft (air born). The remote sensing process includes an interaction between the surveyed targets and incident radiation and exploits electromagnetic radiation. The main characteristics of electromagnetic energy are wavelength (the length of one wave cycle, which can be measured as the distance between successive wave crests) or equivalently frequency (the number of cycles of a wave passing a fixed point per unit of time). Therefore, the two characteristics are inversely related to each other. The higher the wavelength, the shorter the frequency. Remote sensors can be divided in (Figure 3.2):

- ***Active***: active sensor provides their own energy source for illumination. The sensor emits radiation which is directed toward the target to be investigated. The radiation reflected from that target is detected and measured by the sensor. Advantages for this type of sensors are the ability to obtain measurements anytime, regardless of the time of day or season. A valuable active sensor is the Synthetic Aperture Radar (SAR);
- ***Passive***: remote sensing systems measure energy that is naturally available (such as sun energy).

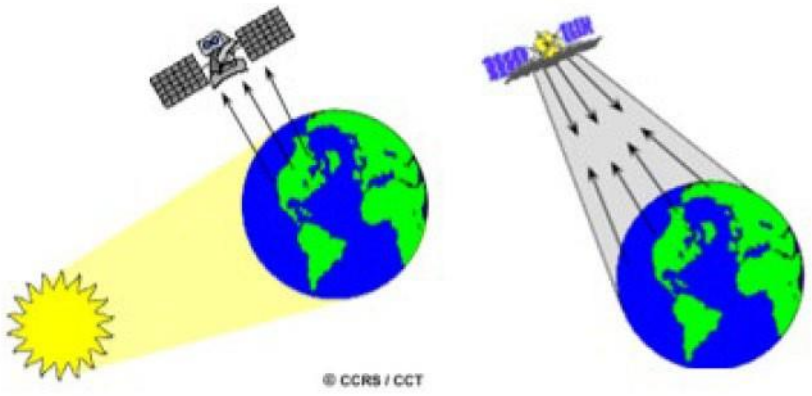

Figure 3.2: Active (right) and Passive (left) remote sensing (http:// www.ldeo.columbia.edu.)

3.3.1 Synthetic Aperture Radar

Synthetic Aperture Radar (SAR) is an active microwave remote sensing imaging system, which monitors the earth's movement during both the night and the day and in all weather conditions (Henderson and Lewis, 1998; Franceschetti and Fornaro, 1999). These sensors measure the distance between the sensor platform and the target on the ground, mounted on-board to an aircraft and/or a satellite. The SAR operation principle is the repeated observation of a given target, in a certain number of echoes, during the passage of the sensor. In particular, the radar system transmits electromagnetic energy with high power and receives the echoes of the backscattered signal from the lighted target in a sequential way, whereas microwave pulses are transmitted by an antenna towards the Earth surface. The microwave energy scattered back to the spacecraft is measured. The typical SAR geometry is illustrated in Figure 3.3. The platform moves in the along-track direction or azimuth, while the direction perpendicular to the radar's flight path is the slant range. The swath width represents the ground-range extent of the radar scene, whereas SAR length depends on the data take duration.

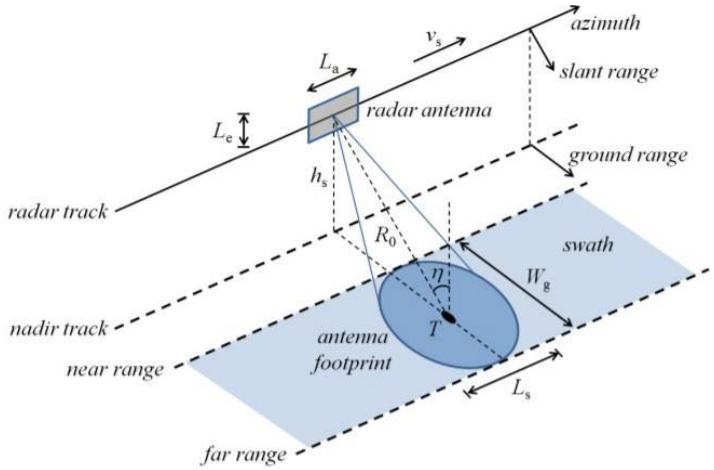

Figure 3.3: SAR acquisition geometry (from Martone, 2019)

The SAR is based on the radar principle to form an image and uses the time delay of the backscattered signals. In particular, electromagnetic waves are sequentially transmitted, and the backscattered echoes are collected by the radarantenna. The time interval measured from the transmission to the reception of the reflected signal represents the different positions due to the platform movement. With an appropriate coherent combination of the received signals it is possible to build a virtual aperture longer than the physical antenna length. From this principle derives the name of "synthetic aperture", allowing to the SARto be an imaging radar (Moreira et al., 2013). According to the satellite platformhosting the SAR sensor, all satellites equipped with SAR sensors orbit the Earth on a near-polar orbit at an altitude ranging from 500 to 800 km above the Earth's surface. Satellite technology provides two different trajectories (Figure 3.4):

- *ascending orbit*: satellite travels from the south towards the North Pole;
- *descending orbit*: satellite travels from the North Pole towards the South Pole.

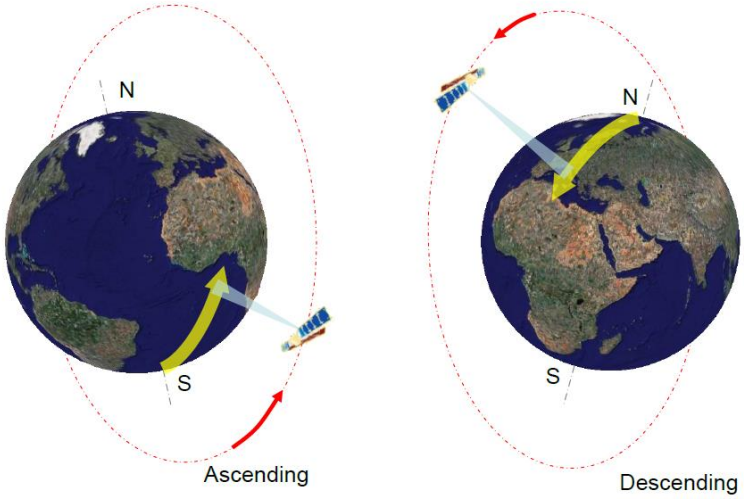

Figure 3.4: Illustration of ascending and descending satellite orbits (from ESA GMES, 2009)

In this way, the same area is revisited along the two orbits, collecting ascending and descending imageries. The interval of time that a satellite takes to revise in the same area is called "*revisiting time*". This time interval changes depending on the type of satellite, ranging from 35 days for old SAR sensors (such as ERS or ENVISAT) to around 4 days for newer sensors, such as Cosmo SkyMed. During its journey a satellite emits millions of radar signals along the LOS (radar beam's line of sight) toward the Earth's surface. A very important geometric parameter of the sensors is the inclination of the antenna with respect to the nadir, that is called the look angle or off-nadir angle. According to the satellite platform the off-nadir angle can range from values of 20° to 50°, for example the look angle of the ERS satellites is fixed at about 23°; but all subsequent satellites are fitted with the means to vary the viewing angle of the sensors. A very important feature of the sensors is the possibility to change the look angle, that allow to improve the relationship between viewing geometry and terrain slope in case of impediments to SAR data acquisitions (such as mountainous or hilly earth's surface). The first types of satellites, such as Radarsat-1, ERS and ENVISAT, were able to emit and receive the signal only on the right side of the satellite. For

this reason, they were called *right-looking satellites*. Instead newer satellites, such as Radarsat-2, TerraSAR-X and COSMO-SkyMed, are able to emit and receive the microwave beam in the right or in the left of the craft.

Nowadays, satellite SAR operating systems can be distinguished mainly for band, maximum measurable displacement, revisiting time, period of acquisition, and resolution (Figure 3.5). The microwave bands that sensors can use are given below:

- X band – 9.6 GHz of the German-Italian X-SAR on the shuttle missions, corresponding to wavelengths of about 3.1 cm;
- C band – 5.3 GHz of ESA's ERS, ENVISAT, the Canadian Radarsat, and the US shuttle missions, corresponding to wavelengths of about 5,6 cm;
- L band – 1.2 GHz of the Japanese J-ERS and ALOS, corresponding to wavelengths of about 18 cm.

SAR sensors with X and C band have a better ground resolution than L-band and they can monitor, especially in built-up environment, small-scale movements of small objects.

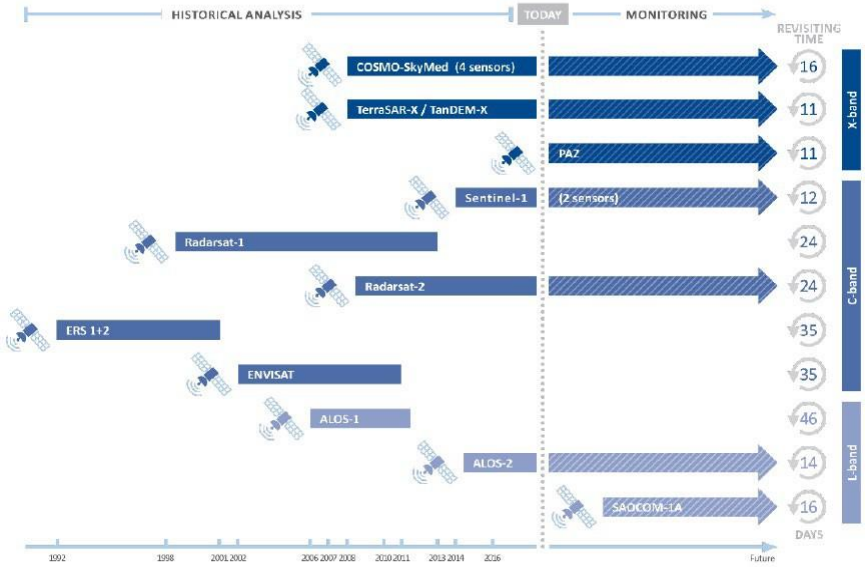

Figure 3.5: Main characteristics of most used SAR sensors (https://site.tre-altamira.com/insar/)

The main properties of SAR signal, that are related to the energy of the backscattered signal are:

- *Amplitude*: depends on reflective quality of materials. Increasing the reflective capacity of the material increases the amplitude of the reflected signal. Then the metals generate a reflected signal with a greater amplitude of the softer marks. Amplitude can be visualized ina digital SAR image (made up of small picture element, called pixels,that represent a small area of the Earth and whose resolution is strictly connected to the sensor characteristics and is typically slightly smaller than the pixel dimension) in black, when the reflective quality of the observed object is low or in white, if the reflective quality of the observed object is high. When areas are with strong backscattered radiation (e.g. urban areas) there are bright pixels, whereas in case of low backscattered radiation (e.g. a quiet water basin) in SAR image there are dark pixels (ESA, 2013).
- *Phase*: depends on the sensor-to-target distance and it is the parameter at the base of the differential interferometry that allows tomeasure the target displacement. The phase of each pixel of a SAR image is composed by: the interaction between the incident waves and the scatterer within the ground resolution cell, the two-ways travel path (sensor-target-sensor: hundreds of kilometres in the satellite case) and the phase shift $\Delta\varphi$, which is equivalent to a phase change induced by the processing system used to focus the image. In particular, the Interferometric technology SAR (acronym InSAR) exploits differences of phase between two or more SAR acquisition from different orbits (and therefore spatial baseline) to derive digitalelevation models (DEMs) (Madsen et al., 1993, Mora et al., 2003). Instead using SAR observation acquired at different times or different temporal baseline is possible to estimate surface displacements.

3.3.2 SAR Interferometry

The SAR Interferometry (InSAR) technique is one of the major applications of the SAR technology which exploits, in its basic form, the phase difference of at least two complex valued SAR images (Rosen et al., 2000). SAR Interferometry allows measuring the displacements of the earth's surface through the phase difference between two or more complex radar images acquired at different times and from slightly different sensor positions. Indeed, each SAR image pixel, that represents the coherent sum of all scattering elements within a resolution cell, contains amplitude and phase information. This information allows detecting for each SAR image the sensor-target path length. Therefore, using two or more SAR images it is possible to retrieve the phase difference called *"interferometric phase"*, which represents any changing in sensor-target distance with sub-centimetric accuracy. This interferometric phase is obtained pixel by pixel fixing a reference image called master and comparing the conjugated secondary image (slave). The interferometric phase is derived from the combination of several terms that can be divided in two main categories: stochastic and deterministic (geometrics) terms. Therefore, with reference to a generic pixel, the interferometric phase difference $\Delta\varphi$ can be expressed as:

$$\Delta\varphi = \Delta\varphi_{geo} + \Delta n_{high}$$

where, $\Delta\varphi_{geo}$ is the deterministic term and Δn_{high} is the stochastic term.

The geometric contributions are associated with the target-to-radar path difference that can be caused by the associated target topography (an angular view difference due to the spatial baseline) and a possible target displacement.

Therefore, the formulato derive the geometric component is as follows:

$$\Delta\varphi_{geo} = \Delta\varphi_{topo} + \frac{4\pi}{\lambda} d$$

with λ the transmitted signal wavelength.

Instead, the stochastic terms are caused by several factors such as the temporal decorrelation (changes of the scattering properties due to temporal modification), the spatial decorrelation (different interaction mechanisms between the electromagnetic wave and the ground surface), the presence of atmospheric agents causing a receiver noise contributions (also called thermal noise decorrelation) or a delay in the signal propagation (Atmospheric Phase Screen, or briefly APS) and inaccuracies in the processing of artifacts and orbital information. In order to reduce these source errors, accurate algorithms have been implemented for the alignment of the two images before comparing the phase difference. Mathematically the stochastic term can be derived with the following formula:

$$\Delta n = \Delta n_{low} + \Delta n_{high}$$

Where Δn_{low} depends from the atmospheric agents and to the orbital errors, while Δn_{high} is related to the decorrelation effects, the thermal noise and processing artefacts.

At the beginning, InSAR technique was used in order to compare few SAR images and provided only qualitative information on deformations (Fruneau et al., 1996, 2003, Rott et al.,1999; Kimura and Yamaguchi, 2000). More recently, the use of Multipass Differential SAR Interferometry allows overcoming the limits of InSAR technology by processing more than 30 images.

As reported in the literature, the main fields of application of SAR data can be summarized as follows (Casagli et al., 2018):

- *Identification and mapping of subsidence areas*: SAR data are ideal in the case of subsidence in urban areas. In fact, the slow vertical movements of the buildings related to the lowering of the ground surface are perfectly measurable by the DInSAR technique;
- *Identification and mapping of landslides*: with the remote sensing technique it is possible to monitor only landslides with slow kinematics (very slow and extremely slow landslides according to the classification of Cruden & Varnes, 1996) and only in the presence of reflectors inside the landslide body;
- *Large-scale mapping of deformation areas*: thanks to the numerous information provided on a regional scale, it is possible to identify deformation areas on a large scale. Deformation maps allow to identify areas with major deformations on a given date;
- *Evaluation of the deformation trend over time*: the time series of SAR data allows to retrace the deformation history of a measurement point back in time.

Instead, the main limits of SAR Interferometry are related to both the physics of the radar signal and the type of data processing and can be summarized as follows (Casagli et al., 2018):

- *Absence of measures in woods, agricultural areas, zone with perennial snow cover or in humid areas*: this limitation is linked to the choice of the permanent scatterer (PS hereafter) which must refer to surfaces that must not change over time. In the case of wooded or agricultural areas, the surfaces to which the PS refer are the vegetation that is affected by strong seasonal variations. On the other hand, in the case of humid areas or areas with snow cover, it is impossible to reflect the radar signal;

- *Absence of displacement information in the N-S direction*: given the acquisition geometry and the orbital trajectory of the satellites in orbit, it is possible to appreciate only deformations along the LOS direction (E-W and vertical components);
- *Non-linear movements*: in the case of movements that do not follow the linear model, there are strong losses of coherence which can lead to the loss of PS. Therefore in such cases it is necessary to use non linear models that require a considerable computational calculation;
- *Revisit time:* the displacement data are linked to the revisit time of the satellites. This limits the use of the data to only the static mapping of the deformations updated to the latest available acquisition;
- *Detectable velocity fields*: the PS technique can only identify deformations within a precise velocity field (velocity of the component along the sensor-target Line of Sight, LOS);
- *Perspective deformations*: the acquisition of data not perpendicular to the earth's surface but according to an angle of view θ gives rise to perspective deformations in the images used. Therefore the orography greatly affects the quality of the measurements and the possibility of obtaining PS points. In fact, due to the perspective deformations linked to the topography of the ground surface, there are areas that are not visible to the satellite and therefore do not contain PS, as for example in the mountainous areas or the slopes facing North and South.

3.3.3 DInSAR Interferometry

In the last decade, the Differential Synthetic Aperture Radar Interferometry (DInSAR) techniques became a valid tool for monitoring the temporal and spatial evolution of slow ground displacements. In several case studies (De Novellis, 2016; Peduto et al., 2017; Peduto et al., 2019; Peduto et al. 2020; Wasowski et al., 2019; Cascini et al., 2009; Cascini et al., Cascini et al., 2013; Castaldo etal., 2015; Davalillo et al., 2013; Gullà et al., 2018; Herrera et al., 2012; Lou et al., 2014; Ezquero et al., 2017; Mateos et al., 2017; Carlà et al., 2016; Casagli et al., 2012; Tapete et al., 2012; Cigna et al., 2014; Ciampalini et al., 2014; Bianchini et al., 2012; Wasowski et al., 2014; Novellino et al., 2014; De Novellis et al., 2016) this technique has been used to detect, study and monitor with centimeter and millimeter accuracy the slow earth movement related to slope instabilities or mass movement. These studies have shown that the remote sensing technique allows to simultaneously observe very large areas with high accuracy and to build long series of homogeneous and coherent data in order to follow the temporal evolution of the movements and therefore to identify any changes.

The main strengths of advanced DInSAR techniques that have favored their development and encouraged their use in various risk scenarios are:

- *Accuracy in measuring surface displacements*: very high accuracy can be achieved, of about 1-2 mm / year on average deformation speed measurements and of about 5-10 mm on deformation measurements;

- *The ability to analyze large portions of the earth's surface*: compared to in situ monitoring techniques, advanced DInSAR techniques allow analyzing areas from a few hundred to tens of thousands of km^2, ensuring a high spatial density of the measurement points. Therefore, in the case of spatially extended deformation phenomena, such as those potentially related to subsoil exploitation activities, the advanced DInSAR techniques are particularly effective in terms of costs/ benefits, especially when compared to the extent of the analysable area.

The DInSAR analysis technique has several limitations which can be summarized as follows (Casagli et al., 2018):

- *The phenomena of temporal decorrelation*: depend on the variability of the electromagnetic properties (reflectivity) of the radar targets between the different days of data acquisition, indicated by the time baseline parameter. Areas covered by vegetation are more subject to decorrelation phenomena than urban centers and exposed rocks that remain more stable over time;
- *Geometric decorrelation*: the quality of the interferogram also depends on the distance between the two orbits traveled by the sensor during the acquisition of the two images (called normal or geometric baseline). In particular, the higher the absolute value of the baseline, the smaller the common band between the two signals and therefore the lower the signal-to-noise ratio relative to the interferogram generated by them. In particular, as the absolute value of the baseline increases, the normal band between the two signals decreases and therefore also the signal-to-noise ratio relative to the interferogram generated by them;

- *The variation of atmospheric conditions*: the interpretation of the data is affected by the atmospheric conditions during the two acquisitions which can generate an additional phase term that is difficult to discriminate from the contribution related to the movement.

At the base of DInSAR technology there is the development of innovative algorithms such as those adopted for multipass Differential Interferometric Synthetic Aperture Radar (DInSAR) image processing, which allows the retrieval of more than 20- year displacements of the topographic surface at fairly affordable costs and overlarge areas. Their increasing diffusion in the scientific literature testified the potential of DInSAR data for several different applications (e.g. European Space Agency's (ESA) projects MASMOV, ALPS, SLAM, TERRAFIRMA, etc.). In the last decades, images acquired by Synthetic Aperture Radar (SAR) sensors and processed via Differential Interferometry algorithms (DInSAR) have been increasingly applied by the scientific community to study the measurable effectsof natural or anthropogenic phenomena in different fields of geosciences, including geology, geophysics and glaciology (Crosetto et al., 2015), and in the civil and environmental engineering. As a result, the scientific community analyzed a number of case studies that successfully investigated potential and limits of the DInSAR techniques for the risk management of slow moving landslides. Depending on the techniques used for the analysis of phase signals in interferometric stacks it is possible to identify two different techniques:

- *Persistent Scatterers technique* (PSInSAR) that allows to operate at full resolution (Ferretti et al., 2000, 2001; Costantini et al., 2008; Crosetto etal., 2008).
- *Small Baseline Subset technique* (SBAS) useful to measure ground displacements over large areas (Berardino et al., 2002; Fornaro et al., 2009).

3.3.4 Permanent Scatterers in Interferometry

In the SAR interferometric technique, atmospheric disturbances greatly influence the accuracy of the results. In order to improve the results obtained and to reach on each pixel a submeter DEM accuracy and a millimetric terrain motion detection (Ferretti et al., 2001) a permanent scatterers procedure can be used. Indeed, starting from long time series of interferometric SAR images, this technique identifies and exploits the stable natural reflectors called permanent scatterers (PS), coherent over long time intervals. The identification of permanent scatterers depends on the coherence maps associated with the interferograms. In fact, if a target has a coherence always greater than a certain adequate value, it could be selected as a possible PS. Therefore, there are two variables to be optimized: the size of the estimationwindow (the larger the window size, the greater the precision of the estimator but the lower the resolution) and the coherence threshold. Thus, the coherence threshold and the window size are derived from a trade-off between the probability of detection and the false alarm rate. Moreover, the satellite data coherence depends on the size of the PS, in particular when the size of the PS is lower than the resolution cell, the coherence is good and all available images of the satellite data set can be exploited successfully.

3.3.5 DInSAR application to slow-moving landslides

In recent years the application of DInSAR technology has experienced strong growth (Berardino et al., 2003; Canuti et al., 2006; Cascini et al.,2007; Stramondo et al., 2008; Vilardo et al., 2009; Milone et al., 2011; Herrera et al., 2011; Peduto et al., 2015; Nicodemo et al., 2016; Gullà et al. 2017; Peduto et al., 2019; Peduto et al., 2020) for monitoring slow moving landslides such as deep-seated gravitational movements, creep phenomena, slides and earth flows (Tofani et al., 2014).

Studies in the literature have shown that DInSAR technology is a valuable tool for monitoring and studying the displacements of the earth's surface at differentscales: detailed (>1:5000) (Colesanti et al., 2003; Herrera et al., 2011), large (1:25 000 to 1: 5000) (Notti et al., 2010); medium (1 : 100 000 to 1 : 25 000) (Cataniet al., 2005; Cascini et al., 2009a,b, 2010a, Lu et al., 2012) and small scale (<1 :100 000) (Meisina et al., 2008). In particular, in the case of small and medium- scale studies, DInSAR technology is used to update the landslide inventory mapby combing conventional monitoring data and remote sensing data. However, as for traditional monitoring techniques, also remote sensing technology has some limitations for field applications.

Firstly, the ability to measure only the projection of the displacement along the Line of sight (LOS) (Rocca, 2003; Manzo et al., 2006) and secondly the ability to monitor landslides ranging from extremely to very slow phenomena, according to the velocity classification of Cruden and Varnes (1996) result in the impossibility of detecting LOS displacement rates exceeding 8-10 cm/ yr in the presence of low density of stable scatterers (Nicodemo,2017).

In order to monitor with SAR technology all three displacement components, studies carried out in the present PhS Thesis aimed at the development of multi-source monitoring techniques. In particular, through the combined use of SAR and inclinometric data, which provide information about the azimuth and the direction of the displacement, it was possible to reconstruct the three-dimensional displacement vector of the landslide phenomenon (Peduto et al., 2021).

4. Slow-moving landslide modelling

In the scientific literature there are several case studies (Table 4.1) of slow-moving landslides modelling such as the Portalet landslide in Central Spanish Pyrenees that has been reactivated by the construction of a parking area (Merodo et al., 2014; Bru et al., 2018), the Ivancich landslide that affects the historical center of the Assisi town (Calò et al., 2014; De Novellis,2016), the slow-moving landslides and earthflow in Apennines chain (South Italy) that are influenced by climatic scenarios and geotechnical parameters (Comenga et al., 2012) and the ancient Volturino landslide in Puglia that is a reactivation landslide in the summer periods (Lollino et al.,2014).

Case study	Landslide type	Author
Portalet landslide (Central Spanish Pyrenees)	Slow-moving landslide – secondary creep	Merodo et al. (2014) Bru et al. (2018)
Ivancich landslide (Assisi town, Central Italy)	Deep-seated landslide	Calò et al. (2013) De Novellis (2016)
San Francesco landslide (S. Pietro in Guarano, Sud Italy)	Debris flow	Cascini et al. (1986) Cascini et al. (1992)
Fontana Monte landslide (Puglia, South Italy)	Earth-slide active landslides	Lollino et al. (2014)
Lucera landslide (South Italy)	Quarry slopes in stiff clays	Lollino et al. (2011)
Umka landlside (Belgrade, Serbia)	Slow-moving landslide in marly clay sediments	Abolmasov et al. (2012)
Apennines landslides (South Italy)	Slow-moving landslides and earthflows	Comenga et al. (2012)

Subiaco landslide (Rome, Central Italy)	Flow-type landslides	Sangirardi et al. (2020)
San Fratello landslide (Messina, Sicily-Italy)	Debris flows, complex slides and shallow and deep-seated landslides	Bianchini et al. (2014)
Latronico landslide (South Italy)	Deep and complex landslide system	Di Maio et al. (2018)
Pisciolo landslide (Melfi, Pz, Italy)	Multiple retrogressive landslide	Vitone et al. (2011)
Lattari Mts. (Southern Italy)	Shallow flow-slide	Forte et al. (2019)
Jinpingzi debirs slide (South China)	Deep-seated slow-moving debris slide	Shu et al. (2018)

Table 4.1: Some case study of slow-moving landslide in the scientific literature

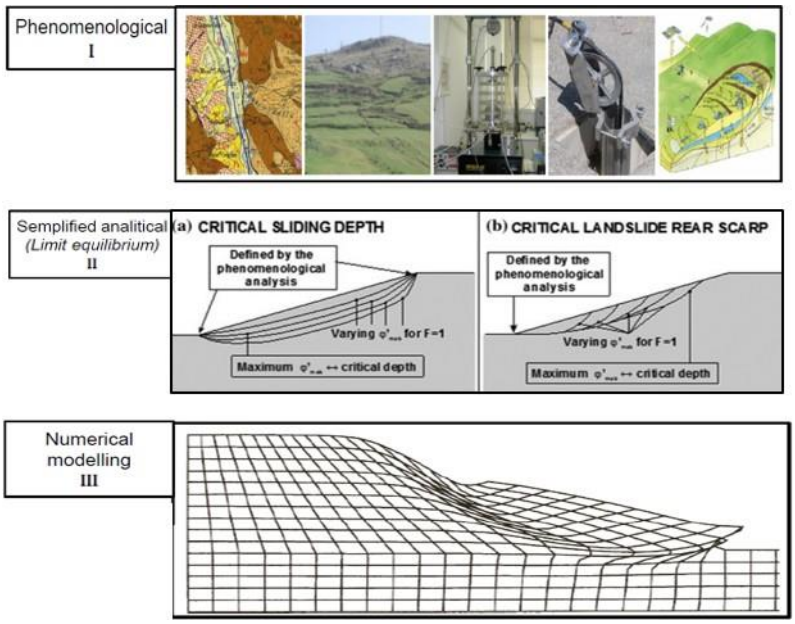

Figure 4.1: Methodological approach for slow-moving landslides modelling (modified from Cotecchia et al, 2014)

All these case studies follow a consolidated methodological approach for the set up and implementation of the geotechnical model of slow moving landslides. This approach (Figure 4.1), consists of 3 Phases (from "*La diagnosi del meccanismo di frana nell'analisi del rischio*", Cotecchia et al., Panel XXV Convegno AGI, 2014):

- ***Phenomenological analysis (I level):*** it is the first level of analysis and is aimed at the phenomenological interpretation of the factors and mechanism of the landslide. The objective of this qualitative analysis is to characterize the typical features of the landslide phenomenon. This analysis makes use of all possible investigation methods for the survey of slope factors and its movements. The survey of slope factors and boundary conditions, both on the surface and in depth, requires an accuracy appropriate to the modelling, so that *I level* analyses should not be confused with heuristic analyses adopted for the zonation of landslide susceptibility at medium and small scales, which only use data on surface factors, typically found in online archives and detected at a regional scale (Cotecchia et al., 2014). Such analyses require inclinometric and piezometric monitoring data, topography and tectonic structure information, surface and deep lithology data, hydrological data, land use knowledge, surface morphological characters, the presence of interacting structures and the soil alteration due to current and past slope movements. Then, with this analysis it is possible for example to identify the geology characterization of the site, the geomorphology, the evolutionary model of the slope and the predisposing factors to the landslide.

- ***Simplified analytical analysis (II level):*** after identifying the geomorphology of the site with the first level of analysis it is possible to move to the second phase of simplified analysis. These analyses use the data of the I level and verify the phenomenological interpretation achieved. Then, it is a quantitative verification of the phenomenological interpretation. Considering the results of the I level, it is possible to carry out simplified analyses for the identification of geomechanical parameters. In the case of landslide, they are intended to identify the geometry of the landslide body, its state of activity and the predisposing and triggering causes. When the objective of the analysis is to identify residual resistance parameters or the critical sliding surface, simplified analyses at limit equilibrium may be carried out. In fact, this type of analysis allow to implement the hydraulic boundary conditions, the geometry of the slope, the different characteristics of resistance and permeability of the soil. Moreover, in case of lack of information about the characteristics of the landslide process, for example about the location of landslide, the piezometric levels or the maximum depth of the landslide body. Limit equilibrium analyses may be conducted to identify uncertain parameters (Cotecchia et al., 2014). For example, if both the foot and the escarpment of the landslide are known, but its maximum depth is uncertain, it is possible to carry out backward analyses for landslide bodies with different depths, but with common foot and escarpment (Figure 4.2.a). Alternatively, if both the foot and the depth of the sliding surface are known, but the main landslide escarpment is uncertain, sliding surfaces characterized by different positions of the escarpment can be analysed (Figure 4.2.b). In the case of multiple active landslides the same parametric approach can be used to identify a hierarchy of instability, which suggests the sequence of activation.

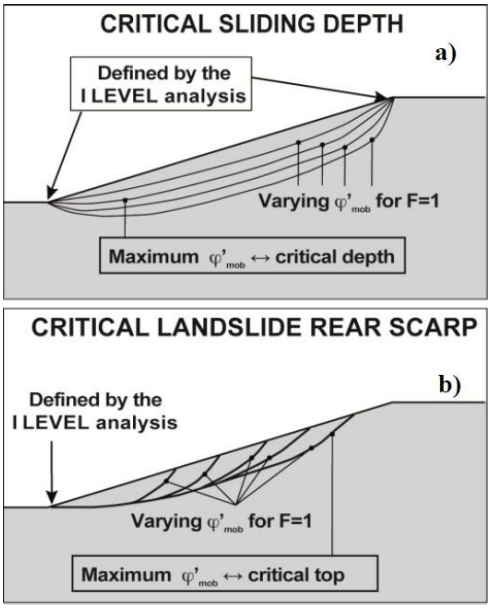

Figure 4.2: II Level of analysis (from Cotecchia et al., 2014)

- ***Advanced shear-stress analysis (III level):*** a final level of analysis is that of advanced modelling that makes use of the results obtained from the first two phases of analysis (Figure 4.3). These analyses allow verifying the previous interpretations and also to add information about the activity in the time of the mechanism. This analysis solves the boundary problemby algorithms that simulate the different processes that affect the equilibrium in the slope. In the scientific literature there are numerous contributions about the application of numerical methods to the prediction of the triggering and propagation of the mechanisms of landslide (for example Cotecchia et al., 2014; Cascini et al., 2005a, 2009, 2010a-b; Duncan, 1996; Gens and Alonso, 2006; Griffiths and Lane, 1999; Lollino et al. 2010, 2011; Morgenstern, 1995; Olivares and Picarelli L., 2006; Pastor et al., 2009; Merodo et al., 2014; Bru et al., 2018; Conte et al., 2020).

An example of advanced modelling is the finite element modelling (FEM), that has the following advantages (Griffiths et al., 1999):

- Possibility to monitor progressive failure up to and including overall shear failure.
- Failure is generated autonomously without the assumption of the shape or location of the failure surface.
- The global equilibrium is preserved until the failure is reached.

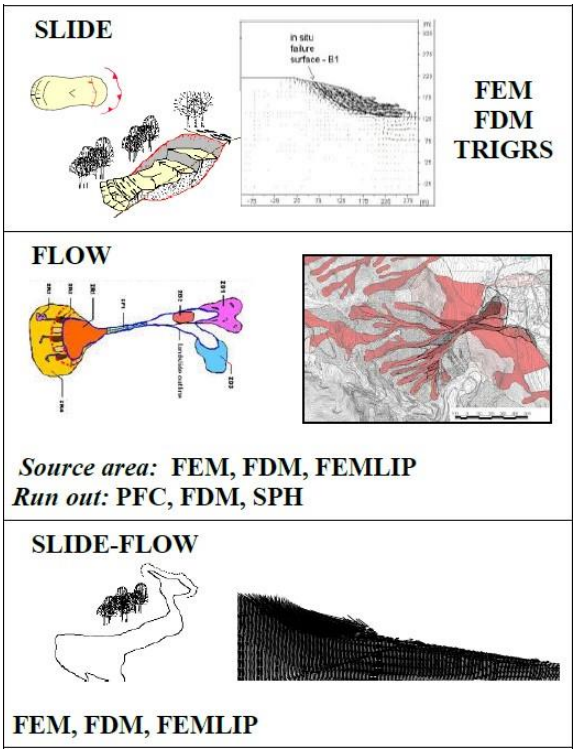

Figure 4.3: Different techniques of advanced shear-stress analysis: FEM (finite element method), FDM (finite difference method), TRIGRS (transient rainfall infiltration and grid-based plane slip analysis), PFC (particle flow code), SPH (smooth-particle hydrodynamics) and FEMLIP (finite element method with agrangian interpolation points) (from Cotecchia et al., 2014).

This approach is widely used in literature for the study of slow-moving landslides, but it presents difficulties related to the recognition and monitoring slow-moving phenomena in urban area (Guzzetti et al., 2007, 2014; Antronico etal., 2015; Jaboyedoff et al., 2019). Indeed, the human activity makes it difficult to install adequate in-situ monitoring networks and often impossible to take undisturbed samples. All these complications imply increases in terms of time and costs with consequent limitations for a correct phenomenological analysis of the site. For this reason, the present studies intend to provide an original contribution to the adaptation of the conventional methodological approach for the for slow-moving landslides modelling in urban areas thanks to the combined use of conventional monitoring data with remote sensing data. In particular, with reference to the Lungro historic center landslide (Calabria), in order to apply the methodological approach on the 3 levels of analysis, a combined use of conventional monitoring and remote sensing data was used to overcome the limits found in densely urbanised areas.

5. Methodology

The proposed methodology has enriched the widely used three-level approach presented in Section 4 with innovative ingredients that via numerical modelling and multi-source monitoring data improves the kinematic characterization of slow-moving landslides in built-up areas.

To this end, the following analysis were performed:

- Multi-source landslide characterization via the combination of conventional and remote sensing monitoring data.
- Synergistic analysis of kinematics and effects on the exposed structures.
- Comparison of FEM modelling results with SAR monitoring data and damage survey data.

With specific reference to the analysed case study of Lungro landslide a step forward is represented by:

- The definition of an updated landslide model based on the full integration of both geological-geomorphological criteria and conventional and innovative monitoring data;
- the creation of landslide DInSAR-geotechnical velocity maps (DGV maps) starting from the combined use of inclinometer measurements and A-DInSAR data;
- the calibration of the soil shear strength parameters c and ϕ through the slope stability analysis via Limit Equilibrium Method;
- the calibration of soil mechanical parameters E through the stress-strain analysis via Plaxis software.

In particular, the proposed methodology consists of the four levels (Figure 5.1).

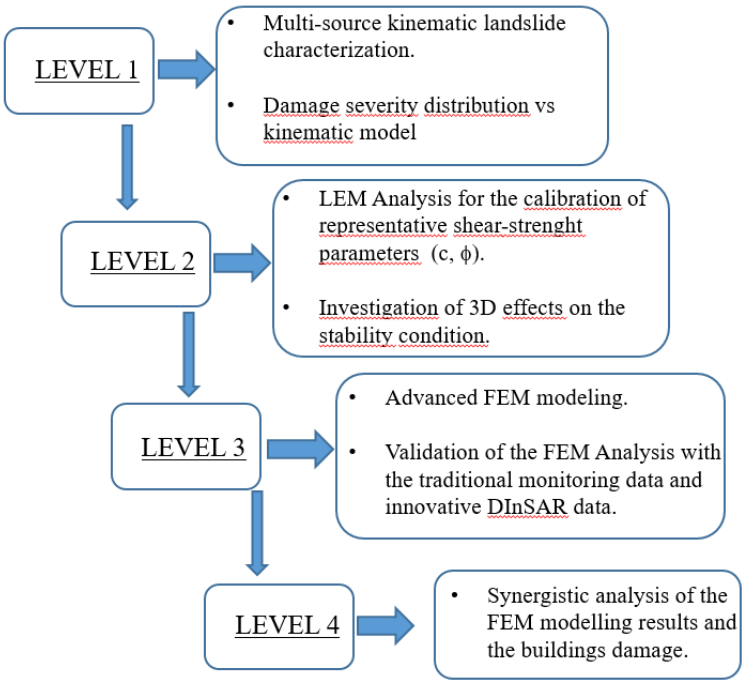

Figure 5.1: The proposed methodology

Level 1: (1) the objective of this phase is the kinematic landslide characterization with the combined use of conventional monitoring data (inclinometers, GPS), remote sensing DInSAR data and the distribution of damage severity to the buildings in the landslide-affected area. An original product of this phase is the A-DInSAR-Geotechnical velocity (DGV) map that, starting from a joint analysis of inclinometer measurements and A-DInSAR data (examples in literature are provided by Tofani et al. 2013; Calò et al. 2014; Del Soldato et al. 2018; Wasowski and Pisano, 2019) carries out a novel quantitative comparison allowing for the assessment of the prevailing local velocity versus/direction and the related projected modulus that are jointly represented as easy-to-read velocity vectors (at the ground surface) over the landslide-affected area.

(1) based on D. Peduto et al. 2021

The followed approach helps in distinguishing those portions of the landslide that exhibit either mainly rotational or translational displacements. Furthermore, the quantitative information provided by the projected velocity values is synergistically analysed with respect to the severity and distribution of the damage recorded to buildings located in different portions of the analysed landslide. Finally, a few detected anomalous damage levels locations are investigated taking into account possible additional conditioning factors of the building performance associated with the presence of buried sub-services whose interaction with landslide mechanism is not yet adequately proved.

In particular to this end, the followed procedure at Level 1 consists of two phases pursuing respectively i) the retrieval of both geometric and kinematic features from multi-source monitoring data and information on related effects (i.e., damage) on buildings, ii) a synoptic analysis of all available data aimed at pointing out the factors conditioning the evolution and the interaction with the exposed elements (Fig. 5.2).

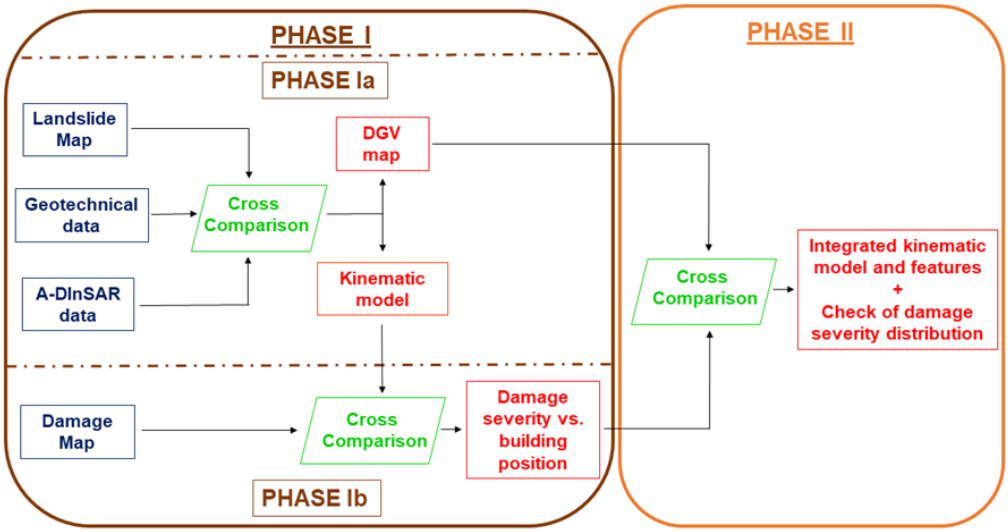

Figure 5.2: Framework of the procedure at Level 1 (from Peduto et al., 2021)

Phase I is twofold. In Phase Ia, the landslide map, inclinometric data and A-DInSAR data are used to validate the kinematic model of the landslide defined on geological-geomorphological basis. Then, A-DInSAR and inclinometric data are fully integrated to derive the A-DInSAR-Geotechnical Velocity (DGV) map, which provides 3D velocity vectors (with assigned moduli, direction and versus) of the landslide based on the joint analysis of landslide boundaries and slip surfaces derived from geomorphological criteria and inclinometers together with information on digital elevation model (DEM), orbit and acquisition geometry of DInSAR data. In particular, the direction of the 3D velocity vector and its angles in the horizontal and vertical plane are described by the three types shown in Figure 5.3 (Type I, Type IIa, Type IIb, hereafter).

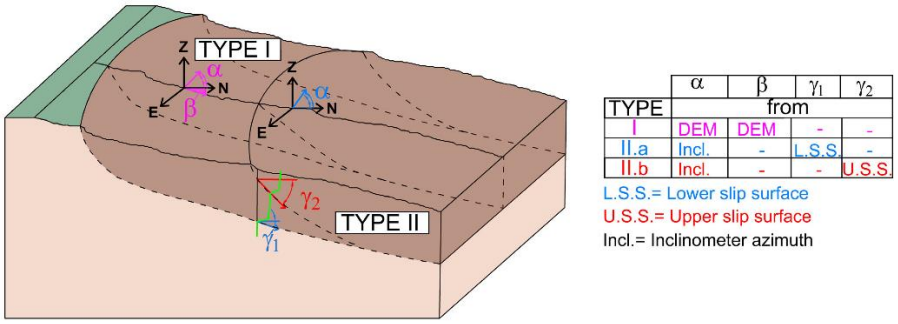

TYPE	α	β	γ1	γ2
	from			
I	DEM	DEM	-	-
II.a	Incl.	-	L.S.S.	-
II.b	Incl.	-	-	U.S.S.

L.S.S.= Lower slip surface
U.S.S.= Upper slip surface
Incl.= Inclinometer azimuth

Figure 5.3: Sketch of the conceptual models (kinematic types) used for A-DInSAR data projection based on the inclinometer data, the digital elevation model and the position of the PS with respect to the cross-section of the landslide (from Peduto et al., 2021)

The background idea is that inclinometer and A-DInSAR data (constrained by their respective 1D measurement directions, i.e. horizontal along the azimuth for inclinometers and along the LOS for A-DInSAR, see (Figure 5.4), if properly combined, can help in reconstructing the "real" velocity vector of the landslide.

This is of key importance when quantitative analyses concerning both the kinematics and related effects on structures/infrastructures are to be performed.

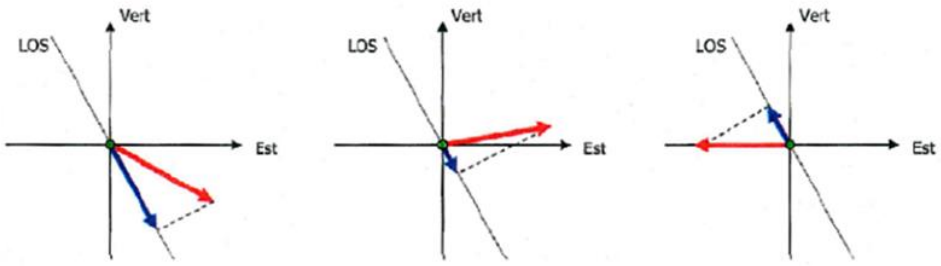

Figure 5.4: Change in value and sign of the strain component measured along the LOS (arrow blue) according to the orientation of the real direction of movement (red arrow) (from Casagli et al., 2018)

In previous works carried out at the basin scale (Bianchini et al., 2012; Cascini et al., 2010), projections of A-DInSAR data from the LOS to the steepest slope direction were adopted; in this study, a procedure at the scale of the single slope is proposed to accomplish the full integration of A-DInSAR and inclinometer data to reconstruct roto-translational displacements. In particular, firstly A-DInSAR data and the available inclinometric measurements are projected along the same directions, which are identified as the ones pertaining to the specific portion of the landslide where both measurement points are located (see Fig. 5.3). Then, the representative velocity direction is defined as the direction providing the best cross-fitting in terms of (minimum) ΔV between the projected A-DInSAR and inclinometer velocity moduli. To this aim (see Fig.5.3), adapting the procedure proposed by Cascini et al (2010, 2013), the representative velocity vector has an inclination with respect to the vertical plane equal to the angle of either the steepest slope direction (β) or the sliding surface (in some cases considering either the lower (γ_1) or the upper (γ_2) slip surface should both of them be detected along the inclinometer vertical). As for the reference direction on the horizontal axis (α), it is assumed as either the inclinometer azimuth direction or the aspect slope angle derived from the digital elevation model (DEM). This allows defining three different types of projections. When both inclinometer and PSs are located within the landslide body (where the translation movement is

assumed to prevail), both measurements are projected along the steepest slope direction (Type I in Fig. 5.3) with the aspect (α, in the horizontal plane) and the slope (β, in the vertical plane) angles both derived from the DEM. Then, for measurement points (i.e., inclinometers and PSs) both located in the head of the landslide - where the rotational movements prevail - measurements follow Type II (Fig.5.3) projection for which α (the angle in the horizontal plane) is assumed equal to the azimuth angle of the inclinometer and γ represents the inclination angle (in the vertical plane) of the sliding surface. In this latter case, where the inclinometer shows the presence of two sliding surfaces, two angles are considered (i.e., γ_1 or γ_2) representing the inclination angles (in the vertical plane) of the lower or upper sliding surface respectively. In particular, in case of projections along the lower sliding surface (see Figure 5.3) the landslide movement is mainly translational evolving along a sliding surface sub-parallel to the ground surface, thus the angle γ_1 is approximated to the slope angle derived from the DEM. Instead, in case of projections along the upper slip surface the rotational component prevails and the γ_2 angle is equal to the inclination angle of the upper sliding surface detected by the inclinometer (Fig. 5.3).

It is noteworthy that, for the case study at hand, the above assumptions are cross-checked and the projection type providing the best fitting between A-DInSAR and inclinometric measurements within different portions of the landslide is finally adopted to project each A-DInSAR LOS velocity to the representative velocity directions represented in the DGV map. Furthermore, taking into account that the projection operations of A-DInSAR data from the LOS to the representative direction can be biased by errors (see for instance Cascini et al, 2010; Colesanti and Wasowski, 2006; Wasowski and Pisano 2019) related to the sensitivity of SAR sensor acquisition geometry with respect to the topography (slope and aspect angles) as well as to the movement direction provided by the azimuth inclinometer (Wasowski and Pisano 2019), A-DInSAR projected

velocity vectors considered in the DGV map are selected among those for which the projection coefficient from the V_{LOS} modulus to the representative direction are below the threshold value of 3.33, as proposed in literature by some authors (Bianchini et al., 2013; Cascini et al. 2013; Herrera et al. 2013; Plank et al. 2010). In fact, in the case of a projection coefficient greater than 3.33, the velocity movement along the slope "V_{SLOPE}" would tend to infinity (Herrera et al. 2013). In Phase Ib of Level 1, the map of damaged buildings is compared with the kinematic model of the landslide in order to develop an evolutionary geomorphological model. In particular, the distribution of damage severity level is analysed with respect to the position of the building within the landslide-affected area. Indeed, the performance of the exposed building (Palmisano et al., 2016) or infrastructure (Nappo et al., 2019) on the unstable slope is influenced by its position in the landslide area and its kinematic model as well as by the interaction between the building foundations and the unstable soil volumes.
In Phase II of Level 1, the consistency of the A-DInSAR-geotechnical velocity (DGV) map (resulting from Phase Ia) and the distribution of building damage severity (resulting from Phase Ib) is cross-checked also addressing further investigations aimed at deepening observed discrepancies, if any.

Level 2: based on the results of the previous phenomenological analysis, LEM Analysis were carried out for the calibration of representative shear-strenght parameters (c, ϕ) and for the investigation of 3D effects on the stability condition. These studies were carried out for all the different groundwater conditions measured by the piezometers present within the landslide area. LEM Analysis were carried out with the SLOPE/W product of the Geostudio software.

The most common limit-equilibrium analyses include those conducted with "methods of slices ". The basic assumptions of these methods are as follows:

- deformation problem in the plane;
- simultaneous failure at all points of the sliding surface;
- the soil behaviour is schematized as a perfectly plastic rigid type (Figure 5.5b) with Mohr-Coulomb failure criterion (Figure 5.5a).

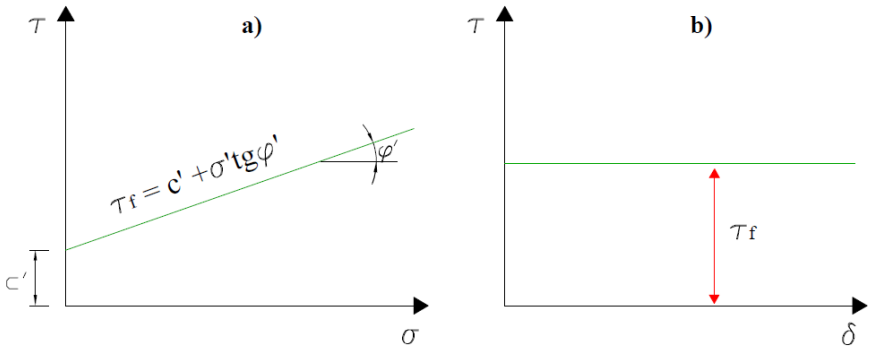

Figure 5.5: Assumptions made in LEM analysis: a) Mohr-Coulomb failure criterion; b) perfectly plastic rigid stress-strain law

Forces acting on a single strip can be synthesized as follows (Figure 5.6):

- W = strip weight of width b and height h;
- N = normal force at the base of the strip;
- S_m = shear force at the strip base;
- E_L e E_R = normal forces between the strips;
- X_L e X_R = shear forces between the strips;
- K_W = seismic load applied in the center of the strip;
- A_n = resulting force of external hydraulic loads;
- D = external load.

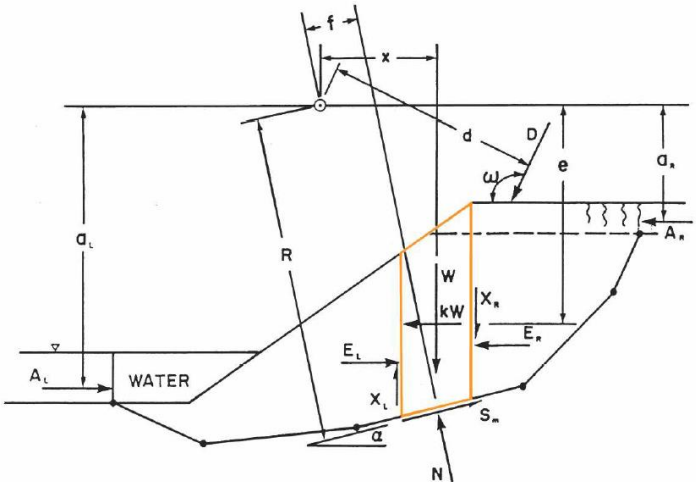

Figure 5.6: Forces acting on a single strip

In the analysis of slope stability the available equations are ***4n*** while the number of unknowns is equal a ***6n-2*** (Table 5.1 and Tab. 5.2). So the number of unknowns exceeds that of the equations and the problem is ***2n-2*** times indeterminate. It is therefore necessary to introduce simplified assumptions depending on the type of method used. Depending on the assumptions used, the methods of analysis at limit equilibrium may be divided into:

- *Approximate Methods*: in case the forces acting on the strips are neglected or their direction and point of application are assumed. This reduces the number of unknowns and consequently also the number of equations to be used. However, this method results in an unbalanced solution, since the calculated forces do not meet all equilibrium conditions. Within these methods it is possible to distinguish two different types: one that considers only the balance of forces and neglects the balance of moments (the equilibrium at the vertical translation or in the normal direction at the base of each strip are not satisfied at the same time) and another that neglects the verification of horizontal equilibrium

and uses the equation of the rotation equilibrium of the entire body for the calculation of the safety coefficient (Simplified Bishop's Method).

- *Strict Methods*: that respect the conditions of global equilibrium of the soil. Among these methods are those of Morgestern-Price, Price and Sarma.

Equation number	Description
n	Equilibrium of forces in the horizontal direction.
n	Equilibrium of forces in the vertical direction.
n	Equilibrium of bending moments.
n	Mohr–Coulomb failure criterion.
4n	**Total number of equation**

Table 5.1: Description of equation number

Unknown number	Description
n	Normal force acting at the base of the strip [N].
n	Point of application of the normal force at the bottom of the strip.
n	Horizontal normal forces between strips [E_L and E_R].
n	Shear force between the strips [X_L and X_R]
n	Point of application of the forces between the strips.
n	Shear force at the bottom of the strip [S_m]
6n-2	**Total number of incognita**

Table 5.2: Description of incognita

In scientific literature there are numerous studies on the influence of hypotheses assumed on the safety factor value (Hanse, 1996; Fredlund and Krahn, 1977; Duncan and Wright, 1980). In particular, in case of an inappropriate choice of the calculation method according to the kinematic characteristics of the phenomenon, Simplified Methods accentuate differences. In addition, limit equilibrium methods take on a constant safety factor value throughout the sliding surface. Obviously this assumption is a great simplification especially if this surface intersects several layers with different mechanical characteristics.
With reference to the case study of the Lungro landslide, the LEM analysis were carried out with the method of Morgersten and Price in order to identify the strenght parameters (c, ϕ) mobilized within the shear band. The calibration was carried out with a *trial and error* procedure by identifying the pair of parameters c and ϕ which corresponded to a safety factor FS equal to unity. These analysis were carried out for all the different groundwater conditions measured by the piezometers and for the longitudinal section A-A '. After identifying the strength parameters (c, ϕ) with FS = 1 for the different groundwater conditions, some (c, ϕ) pairs were identified to be used to carry out the LEM analysis of the other longitudinal sections (B-B ', I-I' and L-L '). These LEM analysis were carried out to identify possible three-dimensional effects within the landslide phenomenon. From the comparisons of the results it was possible to identify very similar trends in the safety factor FS and, therefore, deduce that the three-dimensional effect on the stability conditions of the landslide are slight. Therefore it was possible to carry out two-dimensional FEM analysis.

***Level 3**:* with the aim of identifying the mechanical parameters representative of the landslide phenomenon with references to the results obtained from the second level of analysis, advanced FEM modelling was carried out. The validation of the FEM Analysis results has been performed with the traditional monitoring data and innovative DInSAR data.
In particular, for the reconstruction of the landslide body stress-strain state, the analyses were conducted with the finite elements modeling software Plaxis 2D. In the scientific literature there are numerous examples of numerical analysis applications that identify the requirements for obtaining the most accurate results (Duncan, 1996). These requirements include, firstly a correct choice of the material constitutive model and an exact definition of the initial stress state, which must take into account the various factors such as the pore pressure regime, the stratigraphy of the soil and the presence of structures and infrastructures interacting with the landslide phenomenon.
In particular, in the analyses carried out the ***Gravity Loading*** method has been used to define the initial stress state. This latter is generated by the increase in the gravity force and uses a value of the lateral thrust coefficient "*Ko*" expressed by the relation ν'/(1- ν').
Above the groundwater level, the vertical and total effective stress coincide because the result of negative pore water pressures is zero. However, as regards the choice of the constitutive model to be assigned to the materials involved, it is necessary to take into account that the mechanical behaviour of the soil is very complex (Nova, 2003). In fact, the soils have an irreversible, non-linear behaviour that depends on the load path followed (path dependent). In particular, for the analyses carried out, an ***elastic-perfectly plastic constitutive law with Mohr Coulomb's failure criterion*** and ***the law of the non-associated plastic***

flow (in this case the friction angle ϕ coincides with the dilation angle)ψ were assumed.

The conditions of constraint along the boundaries were represented by horizontal and vertical settlements blocked along the lower edge and by free vertical displacements and impeded horizontal displacements along the lateral edges (Figure 5.7).

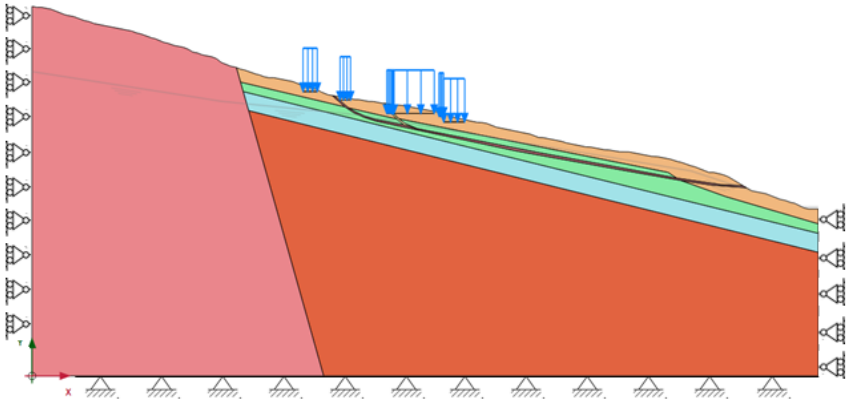

Figure 5.7: The conditions of constraint used in the FEM Analysis

From the pluviometric monitoring data present within the Lungro historic center, it was possible to identify 4 different groundwater conditions to be used in finite element modelling. For all these different groundwater conditions, plastic analysis were carried out and the relative plastic displacements were calculated. Subsequently, in order to reconstruct the temporal trend of the landslide, a cumulative over time displacement was defined equal to the sum of the plastic displacements associated with each event. In this way it was possible to compare the results obtained from the finite element modelling with the inclinometric and SAR data.

Level 4: in order to identify a correspondence between the kinematics of the landslide phenomenon and the buildings damage severity level synergistic analysis of the FEM modelling results and the buildings damage was carried out. To this end, it was necessary to check whether higher buildings damage levels corresponded to higher displacement values and vice versa. Therefore, some diagrams have been made to correlate differential modelled displacement (maximum difference of vertical settlement between any two points on the single building's foundation) with the buildings damage severity. From the results obtained, a good match was found for a large number of buildings.

After validating the results of finite element modelling, the "*empirical fragility curves"*, made by previous studies, have been used (Peduto et al., 2017). The fragility curves (Figure 5.8) are a valid tool in different fields of engineering and the probability is calculated as follows:

$$P\ (\text{Damage} \geq Di|\Delta) = \Phi\ [\frac{1}{\beta}\ \ln\ \frac{\Delta}{\bar{\Delta}}] \quad (i=0,\ldots\ldots 5)$$

With:

- P(·) the probability of reaching or exceeding a particular damage level Di for a fixed intensity of differential settlement D;
- Φ[_] the standard normal cumulative distribution function;
- $\bar{\Delta}$ is the median value of Δ where the building reaches each Di;
- β is the standard deviation of the natural logarithm of Δ for each Di.

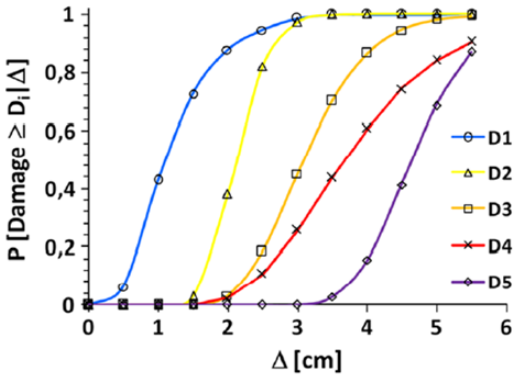

Figure 5.8: Example of fragility curves (from Peduto et al., 2017)

The median values of Δ, corresponding to each Di, are those that give 50% probability of exceeding each damage level; whereas the standard deviation β describes the variability associated with each fragility curve. Furthermore, for the purposes of the analysis of Level 4, the vulnerability curves (Figure 5.9) present in the literature and created for some masonry buildings in the historic center of Lungro were used. These curves allow to calculate the weighted average of the equivalent damage (μD) for a given intensity value of the settlement Δ (Peduto et al., 2017).

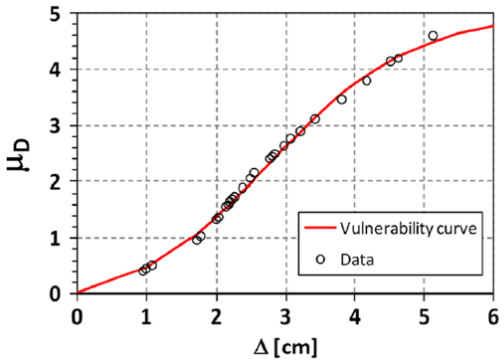

Figure 5.9: Empirical vulnerability curve of Lungro (from Peduto et al., 2017)

These curves were made for each Δ value obtained from the analysis DInSAR data relating to the sample of masonry buildings available and calculating μD (Δ) with the obtained fragility curves according to the formula (adapted from Pitilakis and Fotopoulou 2015):

$$\mu_D(\Delta) = \sum_{i=1}^{5} P_i \cdot d_i$$

with:

-P_i the discrete probability associated to a damage severity level (Di);

- d_i numerical index equals to 1, 2, 3, 4, and 5 for D1, D2, D3, D4, and D5.

In particular in the case study, empirical vulnerability curves were a valuable tool for identifying maximum time intervals within which buildings achieve moderate damage (D3), often associated to losses of functionality (Peduto et al., 2017, Nicodemo et al., 2020, Burland et al., 2004). In fact, from the empirical vulnerability curves it is possible to obtain the displacement value of a building to which the damage level D3 expected to occur, whereas the annual displacement is obtained from the results of the finite element modelling. Therefore, by comparing these displacement values, it is possible to know after how many years a building reaches the moderate damage level (D3) and to intervene before it reaches conditions of collapse or loss of functionality.

6. Case study

The historic centre of Lungro (Calabria region, southern Italy), chosen as case study, has been severely affected by very slow to slow-moving (Cruden and Varnes, 1996) landslides for many years, as highlighted by both conventional and innovative monitoring data available since early 2000s (Guerricchio et al., 2012; Antronico et al., 2015, Gullà et al., 2017; Peduto et al. 2017, 2018). Over time these landslides have led some buildings in the historic center to reach a very high level of damage (D5) (Nicodemo et al, 2020; Peduto et al., 2021). The presence in the Lungro historic center of some urban-architectural units called "*gjitonie*" (Figure 6.1 b), built by the Albanian colonies after their settlement in the Italian peninsula around 1468 (Fiorentino, 2019), makes this urbane center a high quality historical-architectural context that needs to be studied in order to preserve the heritage of gjitonia. Moreover, the presence inside the town of Lungro of the main church of the Eparchy (the Cathedral of San Nicola di Mira (Figure 6.1 a)) makes Lungro a town of particular importance.

Figure 6.1: a) St. Nicolas Cathedral of Lungro (from Google Maps) b) an example of Lungro's Gjitonia

6.1 Geological and geomorphological context

(based on D. Peduto et al. 2021)

The north-western portion of the study area presents the Lungro-Verbicaro Unit (Figure 6.2), consisting of metapelites and metacarbonates (Iannace et al., 2005; Antronico et al., 2015). Close to the urban area, the upper portion of the Diamante-Terranova Unit (Lower Jurassic-Cretaceous), made up of phyllites and slates, crops out. Both lithotypes form a "melange structure" made up of blocks and fragments of different nature (e.g., phyllites, slates and metacarbonates) in a prevalently clayey matrix, originating from phyllites degradation (Antronico et al. 2015, 2013). An Upper Tortonian–Messinian sequence composed by coarse sandstone and shale interbedded with gypsiferous sandstone and gypsum overlays the Diamante-Terranova Unit metasediments. The Early Miocene succession then ends with deposits dating back to the Middle Pliocene-Pleistocene, represented by sandy and conglomeratic beds. Colluvium and landslide debris covers, with a maximum thickness of approximately 10 meters, mantle the phyllite bedrock on the slopes (Figure 6.2) (Antronico et al. 2013; Gullà et al., 2017, Peduto et al., 2016).

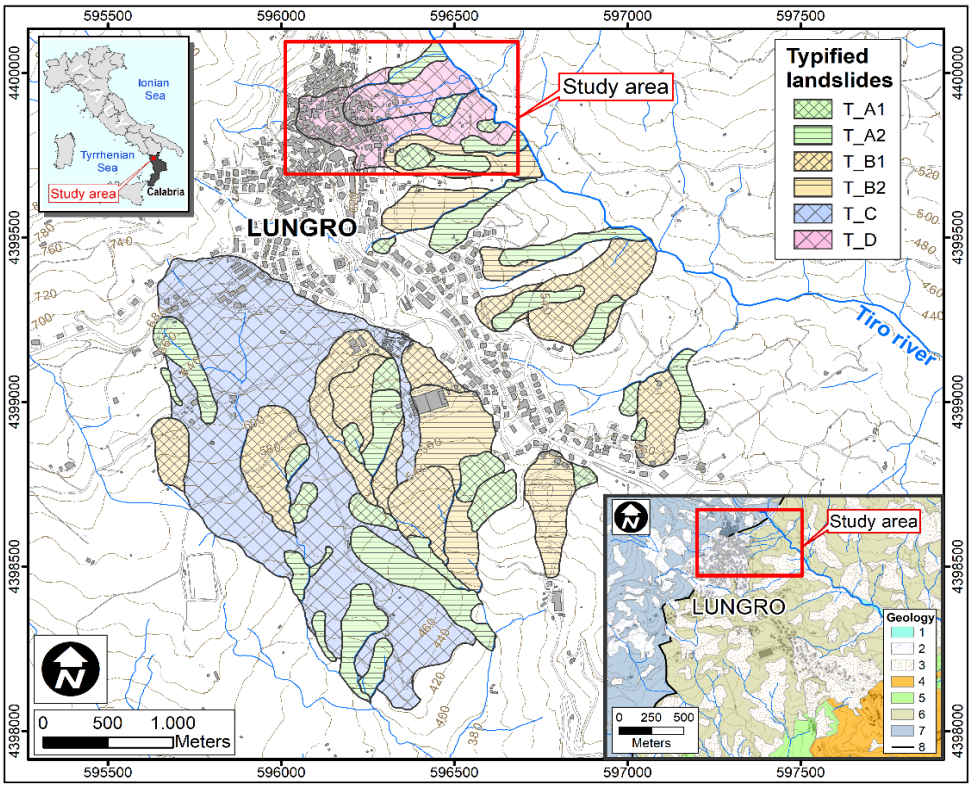

Figure 6.2: Geological and Geomorphological classification of landslides: 1) Alluvian Deposits (Holocene); 2) Detritical Carbonate Deposists (Holocene); 3) Detritical-Colluvial Cover (Holocene); 4)Middle Pliocene-Pleistocene Succession; 5)Middle Tortorian-Messinian Succession; 6) Diamante-Terranova Unit (Lower Jurassic-Cretaceous);7) Lungro-Verbicaro Unit (Anisian-Lower Burdigalian); 8) Tectonic contact. For the typified landslide categories the reader can refer to Table 6.1 (modified from Gullà et al. 2017 and Peduto et al. 2016).

Using multi-temporal aerial photographs dated 1955 (at 1:33,000 scale), 1980 (at 1:25,000 scale), 1991 (at 1:33,000 scale), 2001 (at 1:15,000 scale), and field surveys, previous studies provided the landslide inventory map of the study area (Antronico et al. 2013; Gullà et al., 2017; Peduto et al., 2016) (Figure 6.2). The area is affected by a number of landslides of various types that were classified according to Varnes (1978). Subsequently, Gullà et al. (2017) based on some of the elements that concur in defining the landslide geotechnical model (i.e., the depth of the slip surface, the width and the length of the landslide body, the involved geomaterials and the landslide type) proposed four landslide groups

("typified" landslides, hereafter) as shown in Figure 6.2. In particular, category A landslides, whose type can be ascribed to complex (slide-flow) landslides, are shallower than 10 m and affect detrital-colluvial covers; category B landslides, extending to depths between 10 m and 20 m, affect deeply weathered and chaotic phyllites and belong to the complex (slide-flow) landslide type; category C landslides, extending to depths between 20 m and 30 m, affect deeply weathered and chaotic phyllites and belong to the so called landslide zone (Antronico et al., 2013), representing an area where clustering of mass movements is so tight that it is difficult to distinguish the different bodies (mainly including landslides of the slide-flow type according to Sorriso-Valvo, 1993; Antronico et al., 1996; Greco et al, 2007); category D landslides, extending to depths between 20 m and 30 m, affect weathered and chaotic phyllites and belong to the slide type. A summary is shown in Table 6.1 (from Peduto et al., 2021).

Typified landslide	Width [m]	Length [m]	Depth [m]	Involved Soil	Kinematic type
T_A1	25-100	≤180	About 6	Detritic-colluvial covers (COV)	Slide-flow
T_A2	15-100	≥80	About 10		
T_B1	90-260	130-550	10-20	Deeply weathered and chaotic phyllites (CHAOT)	Slide-flow
T_B2	80-220	>300	10-16		
T_C	830	1500	20-30	Deeply weathered and chaotic phyllites (CHAOT)	Landslide zone
T_D	100-250	350-550	20-30	Weathered and chaotic phyllites (CHAOT)	Slide

Table 6.1: Typified landslides: COV stands for Cover and CHAOT stands for Chaotic (Peduto et al., 2021)

The COV and CHAOT geomaterials that are involved in landslide movements have similar grain size distributions (Figure 6.2a). In particular, the COV geomaterial has a variable particle size ranging from sandy silty gravel to sandy gravelly silt with clay; for the CHAOT geomaterial, the grain size varies from sandy silty gravel to sandy silt with clay. Although the COV and CHAOT geomaterials present a wide

grain size variability, we can observe in Figure 6.3a a significant presence of grain size distribution curves with a cumulative percentage of clay and silt greater than about 50%, pertaining to samples taken at depths varying from about 5 to 35 m below ground surface. In particular, the finer samples are prevalently located from 15 to 25 m below ground surface; within this latter depth range, the inclinometer measurements identify the positions of the sliding surfaces as shown in Figure 6.3b by the available geotechnical logs. This issue indicates, as expected, that the sliding surfaces develop where the COV or CHAOT geomaterials present grain size fractions mainly consisting of clay and silt.

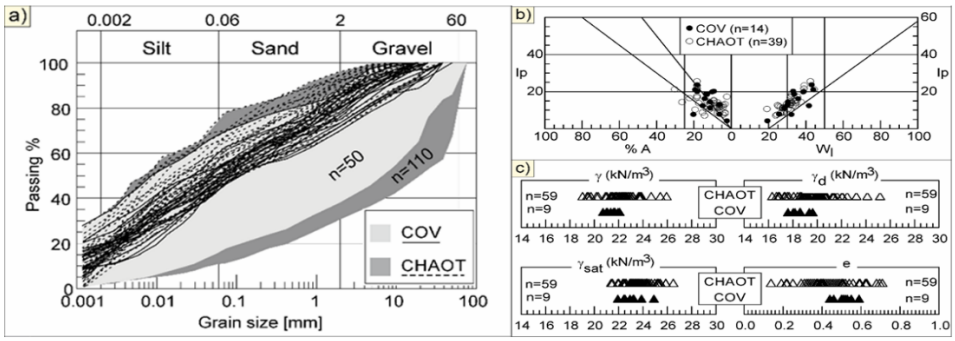

Figure 6.3: Geotechnical properties of geomaterials. a) Grain size distribution curve of the colluvial soils (COV) and degraded phyllites (CHAOT); b) activity chart and Casagrande Plasticity chart; c) natural, dry and saturated unit weight and porosity index of COV and CHAOT geomaterials.

The COV and CHAOT similarity and their general heterogeneity is confirmed by the distribution of the test points in the activity-plasticity charts (Figure 6.3b). In particular, the finer fraction of COV geomaterial is classifiable as prevalently inorganic clays with medium-low plasticity; the finer fraction of CHAOT geomaterial is an inorganic clays with medium-low plasticity. In Figure 6.3c, some index properties are shown. In particular, for the volume of geomaterials involved in the landslide bodies (i.e., COV and CHAOT geomaterials above the sliding surfaces) the representative values of the natural and saturated unit weight can be assumed 22kN/m^3 and 24kN/m^3 with reference to the average values of all COV and CHAOT tested samples (Figure 6.3c).

Figure 6.4 shows the pluviometric and piezometric data measured within the historic center of Lungro in previous studies. From these measurements it was possible to identify a maximum cumulative rainfall values of about 800 mm with piezometric levels up to 10 meters below the ground level. Under this hydrological conditions, the displacements rates increase. Therefore, it can be assumed that two or more consecutive periods of cumulative rainfall greater than 700 mm in 120 days represents a critical condition for the hydrological response of the slope. However, since it is a mainly translational kinematics with maximum depths of about 30 m, there are no evident effects in terms of changes in the crack patterns observed on the buildings (Gullà, 2014).

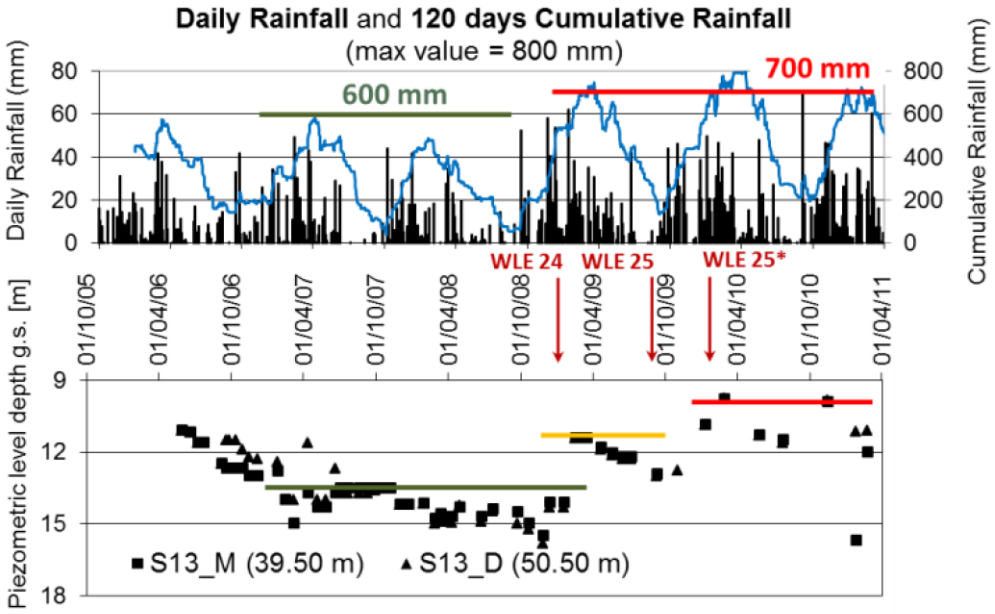

Figure 6.4: Rainfall and piezometric levels (standpipe piezometers) in the Lungro historical centre: blue line: cumulative rainfall; green, yellow and red lines: reference values of the cumulative rainfall and of the piezometric levels (from Gullà, 2014)

6.2 Geotechnical and remote sensing displacement monitoring

Within Lungro historic centre deep ground displacement measurements were performed using a network of six inclinometers (Gullà et al., 2017), Figure 6. 5a. Measurements were carried out from April 2006 until May 2014. The measured cumulative deep displacement moduli are generally constant with depth, and show sharp and well-defined slip surfaces (Figure 6. 5b). Figure 6. 5b shows the velocity values of inclinometer measurements along with their azimuthal directions with reference to the period September 2006 to May 2014 as recorded within the landslide body. As for the involved geomaterials, the six available geotechnical boreholes, equipped with inclinometers, allow recognizing the geomaterials that characterize the stratigraphic sequence of the landslide site (Figure 6. 5b). From top to bottom the stratigraphic section shows the presence of 22-68 m of degraded phyllites (called CHAOT) and subsequent 12-24 meters of colluvial and detrital soils (called COV). Along the S01 borehole, at a depth of 40 m below the ground surface, carbonate rocks are detected (i.e., dolostones and limestones).

In addition, all inclinometer data show well-defined sliding surface positions (Figure 6.5) of which the deepest ones are located approximately 18-27 m below ground surface. Inclinometers S19 and S20 show a second sliding surface approximately 10-15 m deep (Figure 6.5b).

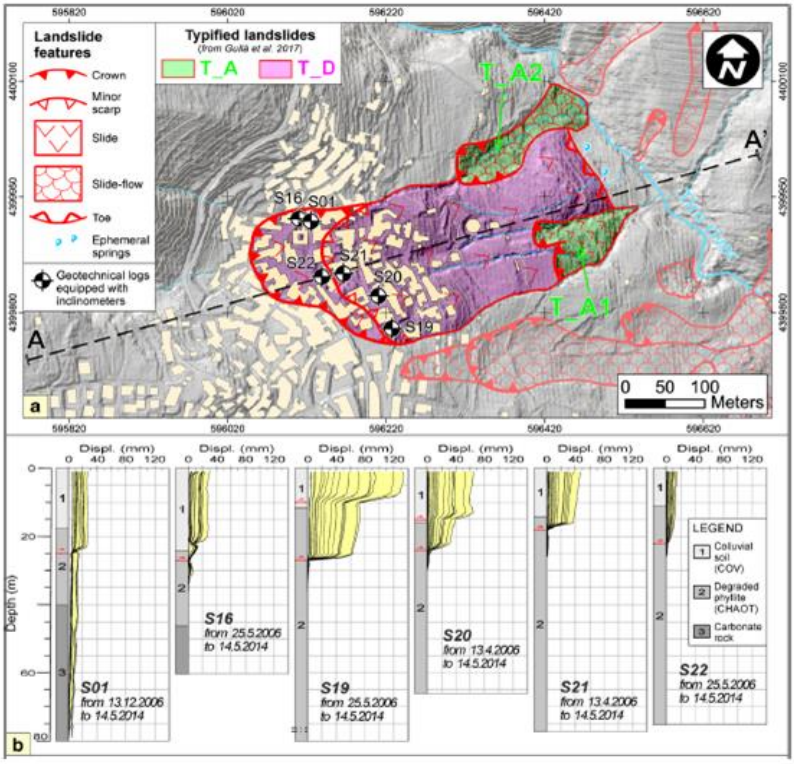

Figure 6.5: Landslide map with localization of geotechnical logs and inclinometers; b) geotechnical logs and inclinometer measurements from 2006 to 2011 (Peduto et al., 2021)

In addition, within the Lungro historic centre a rich database of remote sensing data is available. In particular, the A-DInSAR data were processed according to the SAR tomographic analysis (Fornaro et al. 2009, 2014). The A-DInSAR dataset, whose spatial velocity distribution along the Line of Sight (LOS) sensor-target direction is shown in Figure 6.6, consists of 35 ENVISAT images acquired on ascending orbit (from August 2003 to February 2010, see Fig. 4a) as well as 39 Cosmo-SkyMed (CSK) images acquired on ascending orbit (from October 2012 to April 2014, see Figure 6.6b).

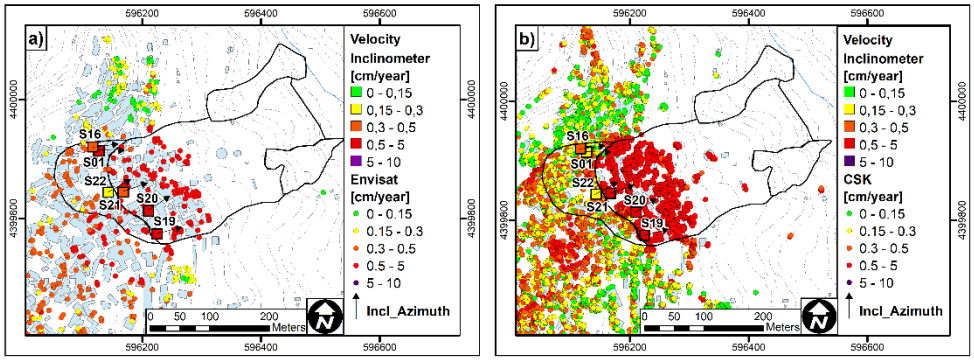

Figure 6.6: Geotechnical and remote sensing velocity monitoring in Lungro historic centre: a) inclinometers (September 2006 - March 2010) and Envisat (September 2006 - February 2010) data; b) inclinometers (October 2011 - May 2014) and Cosmo-SkyMed data (October 2012 - April 2014). A-DInSAR velocity is provided along the line of sight (LOS) direction. The black arrows indicate the azimuthal direction of the inclinometer measurement (Peduto et al., 2021)

Remote sensing data show that the landslide phenomenon does not have constant displacement rates. In fact, at the edges of the landslide, the velocities assume modest values that increase considerably within the landslide body. In addition, the velocities of the two different databases have differences in correspondence with the upstream head of the landslide phenomenon. In fact, in the upper area of the landslide, the velocity of the Cosmo Sky-Med data (Figure 6.6b) are lower than those of the ENVISAT data (Figure 6.6a).

This difference could be related to a slowdown in this part of the landslide phenomenon over time.

6.3 Damage to buildings

The buildings in the analyzed portion of Lungro historic centre belong to a rather homogeneous urban fabric composed by masonry low-rise structures (i.e., 2–3 floors), mainly made of disorganized stones (pebbles, or erratic/irregular stones), on shallow foundations with ages ranging from 70 to 300 years (Nicodemo et al., 2020; Peduto et al., 2017b).

As for damage, the available dataset resulted from a survey carried out in October 2015 over the entire urban area (Peduto et al., 2017b, 2018). In particular, building damage fact-sheets (Ferlisi et al. 2015; Nicodemo et al. 2017a) were filled in and the damage severity level of the surveyed buildings was classified according to Burland et al. (1977). As stated by the authors (Nicodemo, 2017) the classification of building damage was based only on the visible damage at a given time.

Figure 6.7 shows the damage distribution and some pictures of damaged buildings within the landslide affecting Lungro historic centre derived from damage survey studies.

By analysing the building damage level and building position in relation to the landslide phenomenon it was concluded that at the landslides edges, where there are higher differential displacements, buildings suffer from a higher level of damage severity. However, within the landslide phenomenon there are some anomalies. Indeed, for some buildings present inside or outside the landslide phenomenon, where the values of differential displacements are lower, there are very high damage levels (Figure 6.7).

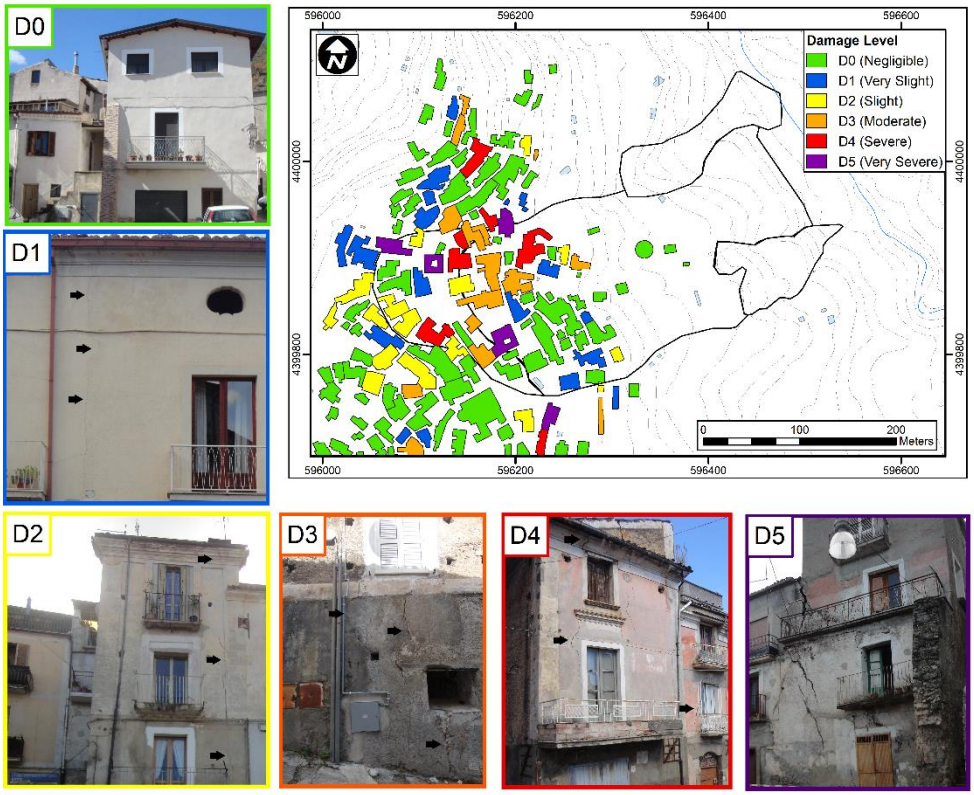

Figure 6.7: Distribution and severity level of damage to masonry buildings in the historic centre of Lungro (Peduto et al., 2021).

7. Results

7.1 Level 1: Kinematic characterization

(based on Peduto et al., 2021)

The studies carried out focus on the Lungro historic centre, where, based on geological-geomorphological criteria and geotechnical monitoring data, previous studies (e.g., Antronico et al., 2013, 2015; Peduto et al, 2016; Gullà et al., 2017) distinguished and mapped an active, medium-deep and slow-moving landslide of slide type, typified as T_D (Figure 6.2a and Table 6.1). Starting from the literature data, a new mapping of this landslide was produced (Figure 6.2a).

The landslide mapping has been updated, following geomorphological criteria proposed by Cruden and Varnes (1996), through interpretation of traditional aerial photographs, Google Earth satellite images, coupled with analyses of a high-resolution DTM (i.e., DTM with 1-m ground resolution, deriving from LiDAR scanning on an aerial platform acquired during 2012 by the Italian Ministry for the Environment, Land and Sea), and detailed multitemporal field surveys.

The landslide involves large part of Lungro historic centre, where most buildings are located (Figure 6.2a). It extends over an area of about 7 ha and occurs on a slope gradient of about 15°. The landslide, which is about 440 m long and 180 m wide, ranges from an elevation of 594 m (in the upper part of the slope) down to 488 m (at the valley bottom). Two distinct bodies (Figure 6.2a) form the landslide: a western active landslide body (~1.3 ha) and an eastern active body (~5.3 ha), which overlaps with the previous one. The landslide has a crown with an irregular shape (400 m long), the main scarp is not evident; the eastern body shows a semi-circular minor scarp with smoothed and eroded morphology.

The right and left flanks (the latter one well defined) are similarly incised and sub-rectilinear in shape with nearly straight traces and coincide with two ephemeral stream channels that drain water towards the Tiro River. Two active secondary landslides typified by Gullà et al. (2017) as T_A1 and T_A2 mask these flanks, in their terminal sector (Figure 6.2a). In this area, the emergent toe of the failure surface was only locally found (Figure 6.2a). Here, some temporary springs, characterized by an aligned drainage pattern whose flow rate increases during the rainfall period, have been observed.

The observed geomorphological features of the landslide indicate that the two bodies can be classified as translational landslides with minor rotational components. Particularly, the landslide motions are mainly translational, with slight rotational character immediately downstream of the two escarpment sectors. The longitudinal section A-A' of Figure 7.1 shows that the landslide mass moves along a low-angle (i.e., approximately 15°) mainly translational surface almost parallel to the ground surface. The total volume of the failed material is about 2 million cubic meters. The inclinometers revealed the presence of a medium-deep sliding surface at depths ranging between 18 and 27 m mainly involving the relatively finer grain fraction of COV and CHAOT geomaterials.

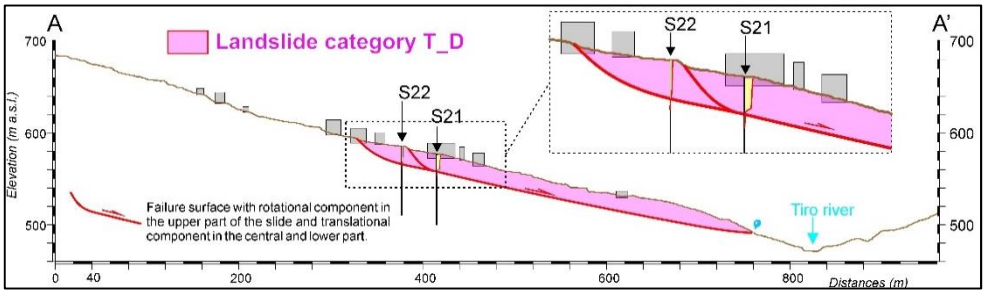

Figure 7.1: Cross-section of the landslide in the historic center of Lungro (from Peduto et al., 2021).

The integrated analysis of the landslide geomorphological features, geotechnical logs and inclinometer data allowed to confirm the kinematic model of the landslide based on geomorphological data. In particular, the longitudinal cross-section shown in Figure 7.2 highlights that the landslide mass moves along a low-angle, roughly

translational surface (at depths ranging from 18 m up to approximately 27 m) with little rotational component. Particularly, the sliding surface develops with a mainly translational component in the central and lower sector of the landslide and with slight rotational components in its upper sector immediately downstream of the two escarpments. In the lowermost sector of the landslide, the slip surface exhibits a rising toe segment.

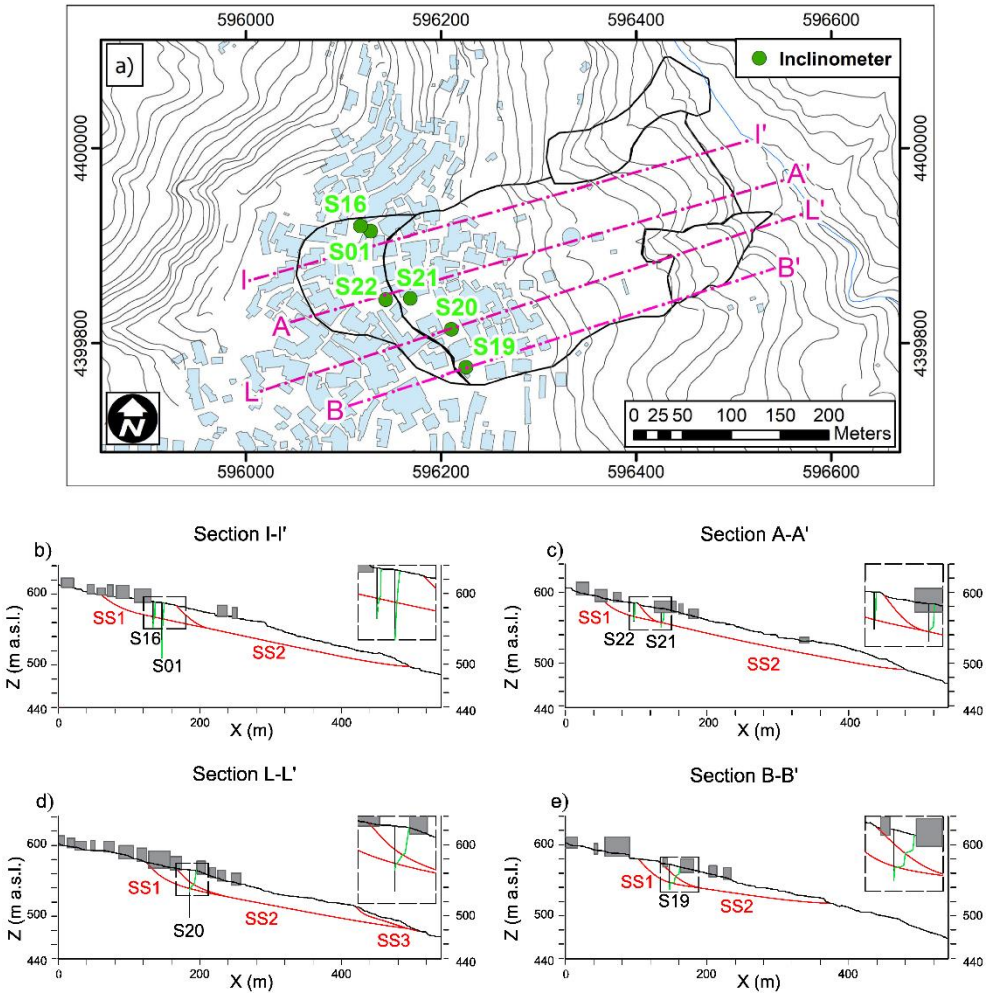

Figure 7.2: Longitudinal cross-sections of the landslide (i.e., kinematic model): positions of the inclinometers with indication of the detected sliding surfaces (SS1 and SS2) (from Peduto et al., 2021).

As a second step, Envisat and Cosmo-SkyMed data were compared with six available inclinometer measurements (Figure 6.3b). For this purpose, assuming that the landslide movement is homogeneous in areas close to the inclinometers, each inclinometer was associated with the PSs falling within a circular buffer of 20 meters. Subsequently, for each inclinometer and the associated PSs, displacement data were projected according to both TYPE I or TYPE II (see Figure 5.3) in order to find out which projection provided the best fitting (Figure 7.3). Figures 7.3 and 7.4 shows the results for inclinometers. As for the inclinometers S19 and S20 detecting two sliding surfaces (Figure 7.2), having assumed that the PSs move in the same way as the closest inclinometer, the angle in the horizontal plane (α) was assumed equal to the azimuth of the inclinometer; whereas the angle in vertical plane was assumed equal to either the slope angle (β) or the inclination angles of the upper ($\gamma 2$)/lower ($\gamma 1$) sliding surface. Then, a quantitative comparison among possible projections for all the inclinometers and the PSs included in the surrounding 20-meter buffer was performed. In particular, ΔV, which is the difference between the average annual velocity of the inclinometer and the average A-DInSAR annual velocity projected either long the steepest slope direction or lower/upper slip surfaces of those PSs included in the 20-meter buffer, was computed. The results for both Envisat and Cosmo-SkyMed data are summarized in Table 7.1 showing that the best fitting projection changes according to the position of the inclinometer in the landslide body. Indeed, it seems that when the inclinometer crosses only the lower sliding surface (S01, S16, S21, S22), the projection operations provide very similar results either along the (lower) sliding surface or the steepest slope direction (on the ground surface). This might be justified by the prevailing translational mechanism with a sliding surface sub-parallel to the ground surface in this portion of the landslide body, as it also resulted from the geomorphological analysis and was validated by the kinematic model.

As for S19-S20 inclinometers (see Figure 7.3), two (lower and upper) slip surfaces are distinguished (see Figure 7.2a) because they intersect the head of the eastern secondary landslide body and the main body of the landslide. In these cases, the projection along the upper/lower sliding surfaces seem to provide the best fitting (see Figure 7.3 and Table 7.1) revealing, in this portion of the landslide, the effects of subvertical displacement associated to the rotational component that also the geomorphological analysis pointed out.

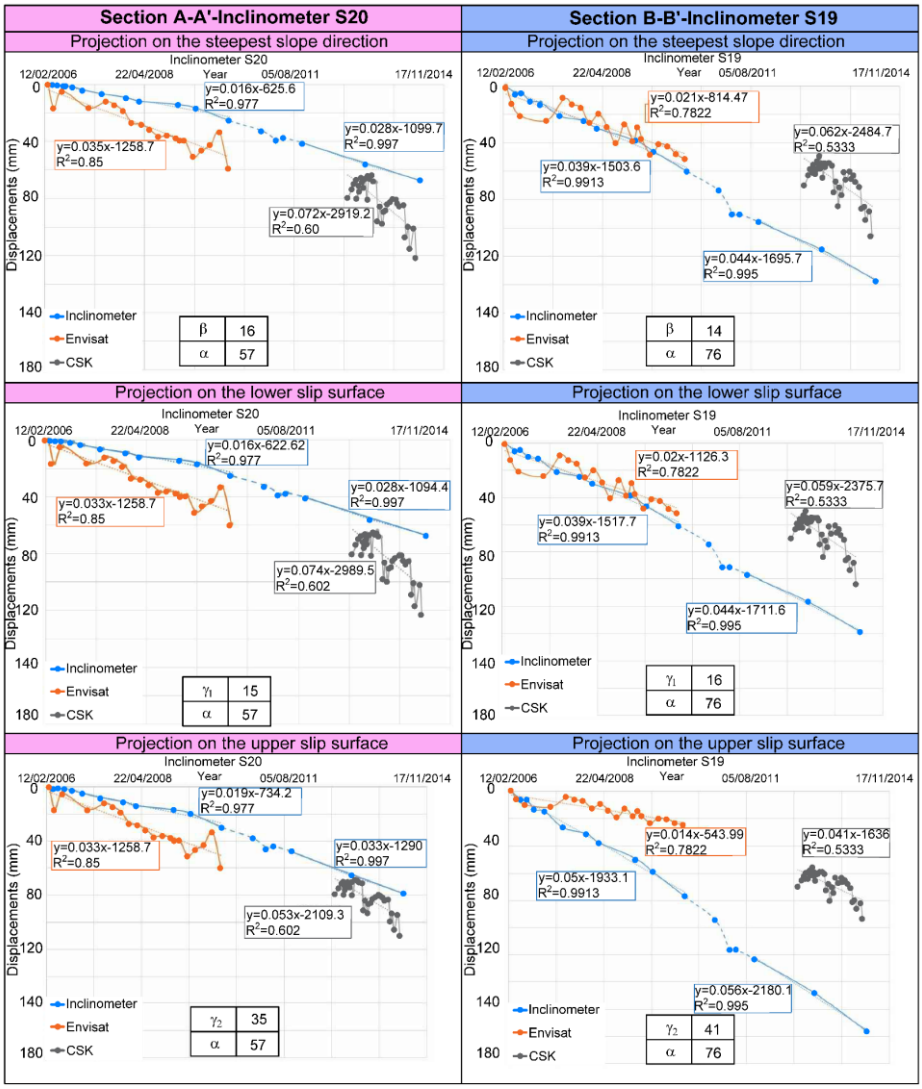

Figure 7.3: Comparison of A-DInSAR data with measurements from S19 and S20 inclinometers based on three different kinematic types (from Peduto et al., 2021).

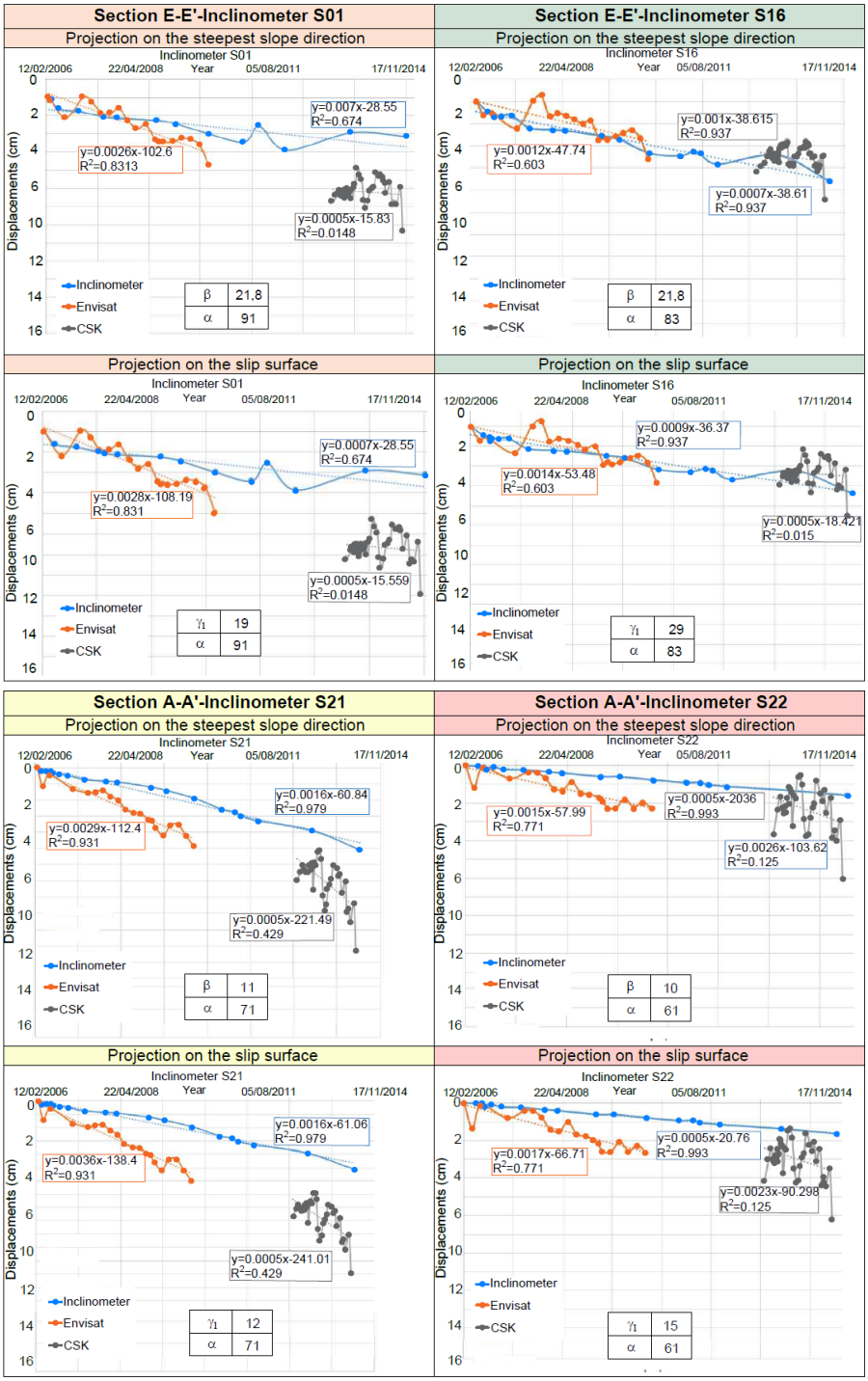

Figure 7.4: Comparison of A-DInSAR data with measurements from S01, S16, S21 and S22 inclinometers based on three different kinematic types.

Therefore, based on the above considerations, the DGV maps within the Lungro historic centre were derived by including all A-DInSAR data within both the landslide perimeter and a 30-metre buffer around the landslide boundaries to consider the errors related to landslide mapping and the localization of PSs as well. For the data projection the three kinematic types shown in Figure 5.3 were considered. Accordingly, the velocity values of PSs located on the main body of the landslide were projected along the steepest slope direction (see Table 7.1) considering both α and β angles deriving from the DEM (Type I). As for PSs positioned near either the landslide head/crown or an inclinometer, the velocity values were projected assuming the angle (α) in the horizontal plane equal to the inclinometer azimuth and the angle in the vertical plane equal to the inclination of the lower (γ1 according to TYPE IIa) or upper slip surface (γ2 according to Type IIb) in agreement with the results of the best fitting shown in Table 7.1.

		Projection on the:					
		Steepest Slope Direction		**Lower Slip Surface**		**Upper Slip Surface**	
Inclinometer	**Intercepted sliding surface**	**Δ Velocity** $_{ENVISAT}$ [cm/year]	**Δ Velocity** $_{CSK}$ [cm/year]	**Δ Velocity** $_{ENVISAT}$ [cm/year]	**Δ Velocity** $_{CSK}$ [cm/year]	**Δ Velocity** $_{ENVISAT}$ [cm/year]	**Δ Velocity** $_{CSK}$ [cm/year]
S01	lower sliding surface	0.47	0.11	0.58	0.11	-	-
S16	lower sliding surface	0.07	0.07	0.04	0.002	-	-
S19	lower/upper sliding surface	0.37	0.66	0.36	0.55	0.77	0.55
S20	lower/upper sliding surface	0.58	1.60	0.62	1.67	0.51	0.73
S21	lower sliding surface	0.003	1.30	0.88	1.27	-	-
S22	lower sliding surface	0.37	0.77	0.44	0.66	-	-

Table 7.1: Summary of the comparison between inclinometric and A-DInSAR (both Envisat and CSK) velocity taking into account the position of the inclinometer with respect to the sliding surfaces of the landslide (see the cross-sections in Fig. 8b-e) and the direction assumed for projection. Envisat data refer to 2003-2010 and CSK data refer to 2012-2014 (from Peduto et al., 2021).

By implementing the kinematic types for both datasets two vector maps were derived (Figure 7.5a and Figure 7.5b). Then, the point-wise A-DInSAR velocity data were interpolated via Inverse distance weighted interpolation method (IDW method) in GIS environment using a grid cell of 2mx2m for CSK and 10mx10m for Envisat to account for different average sensor ground resolution (i.e., ~ 6 × 24 m, respectively, in azimuth and range for Envisat and 3×3 m for CSK, Wasowski and Bovenga 2019, Peduto et al. 2015). In the IDW method cell values is determined using linearly weighted combination of a set of sample points. The interpolation weight inversely depends on distance.
The DGV maps (Figure 7.5a and Figure 7.5b) exhibit comparable velocity values during both periods (i.e., 2003-2010 and 2012-2014). In particular, both Envisat and Cosmo-SkyMed velocity maps show a non-homogeneous distribution of velocities inside the landslide with higher velocity values concentrating at the head, along the boundaries and in few areas within the landslide body (Figure 7.5c and Figure 7.5d). As expected, the results provided by Cosmo-SkyMed are more detailed (thanks to the higher ground resolution of this system), thus allowing an improved zoning of areas with different velocity values.
Moreover, the eastern landslide body exhibits higher velocity values than the western one. Accordingly, as an improvement of the landslide analysis carried out by Gullà et al. (2017), the kinematic model and the interpretation of the DGV maps allowed typifying the landslide into two different bodies T_D1 and T_D2 (Figure 7.5e). Particularly, for T_D1, the average velocity values recorded by all Envisat PSs (period 2003-2010) and CSK PSs (period 2012-2014) are both equal to approximately to 1 cm/year. As for T_D2, the average PS velocity values recorded are approximately equal to 1.6 cm/year during both considered periods. It is noteworthy that this diversity in velocity between T_D1 and T_D2 is also confirmed by the point-wise information provided by the inclinometers that show an average velocity equal to 0.32 cm/year for T_D1 (including S01, S16, S22) and 1.04 cm/year for T_D2 (including S19, S20, S21) over the period 2006-2014.

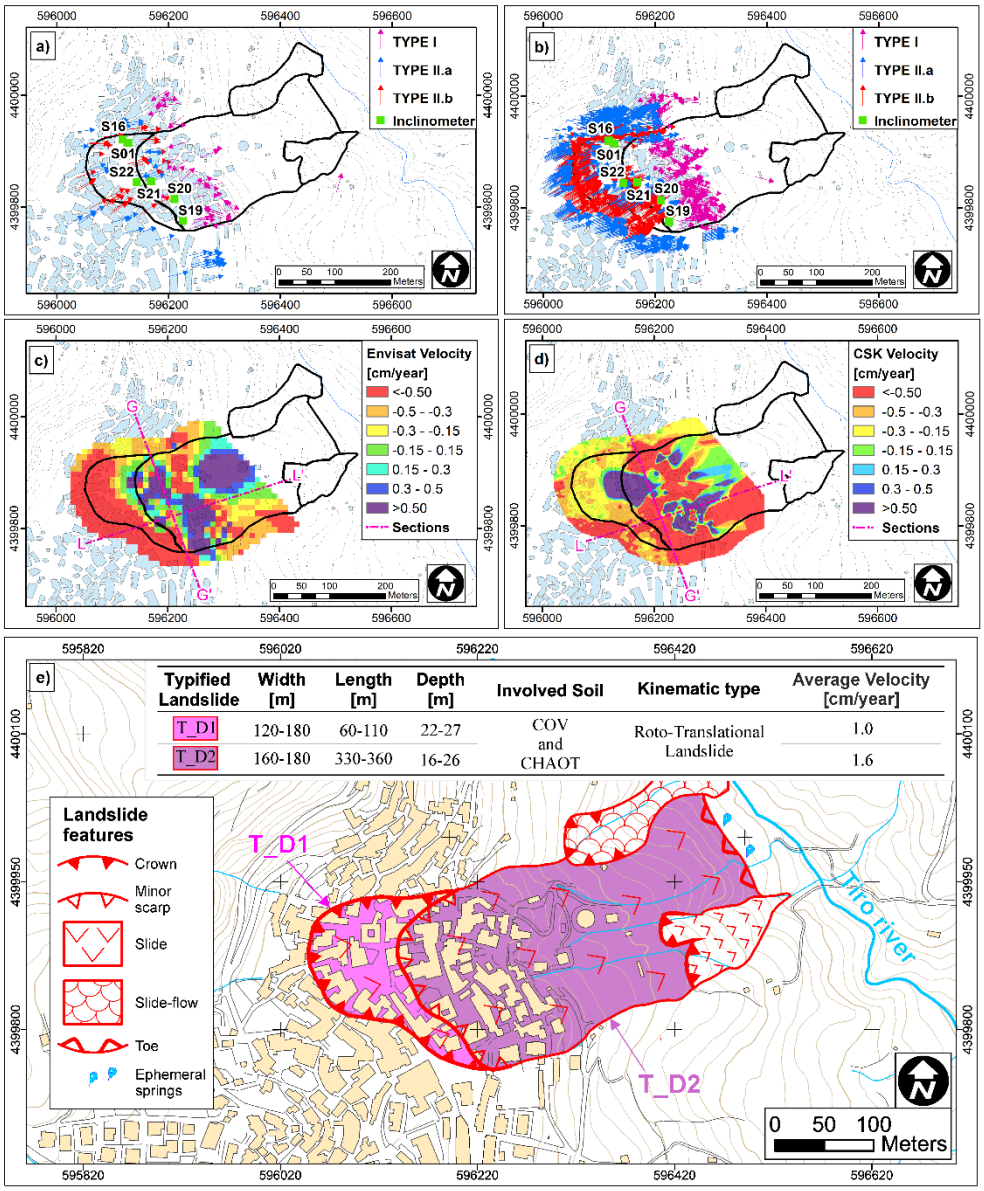

Figure 7.5: Kinematic types used for the projection of a) Envisat and b) Cosmo-SkyMed data (arrows represent velocity vectors; the colors allows distinguishing the type of projection used); c) DGV map based on Envisat data; d) DGV map based on Cosmo-SkyMed data; e) map of the typified landslide.

The purpose of the Phase Ib of Level 1 was shedding a light on the role played by the position of the buildings within the landslide on both the damage occurrence and the severity level. To this aim, the available map of damaged buildings (Peduto et al., 2017b, 2018) was analysed with respect to six sections crossing the landslide

area used to represent its kinematic model. In particular, three longitudinal (Figures 7.6c, 7.6d, 7.6e) and three transverse (Figures 7.6f, 7.6g, 7.6h) sections were analysed; these latter were selected in order to involve as many buildings as possible. Buildings were distinguished as being located on either the head, or the main body, or the boundaries of the landslide. The graph in Figure 7.6b shows a summary for the 65 analysed buildings. It can be observed that i) the buildings with D0 to D1 damage level mainly concentrate in the landslide main body and they never occur in the landslide head, ii) the percentage of D2 and D3 buildings in the main body is comparable to the sum of those in the head and on the boundaries, and iii) the number of buildings exhibiting D4 to D5 damage levels is higher in the landslide heads than in the main body or along the boundaries (see also Ciampalini et al., 2014).

The aim of this stage was to identify possible relationships between the detailed velocity field of the phenomenon and both the distribution and the severity of the damage. Thus, a comparison was made between the map of damage severity distribution and the DGV maps relevant to both Envisat (Figure 7.7a) and Cosmo-SkyMed (Figure 7.7b) data. Both Figures show that buildings with highest damage severity levels concentrate in the head and along the boundaries of the landslide; herein the highest velocity values (and their gradients) are recorded. However, some buildings with D3-D5 damage levels are present within the landslide body in correspondence of local "anomalous" higher velocity values.

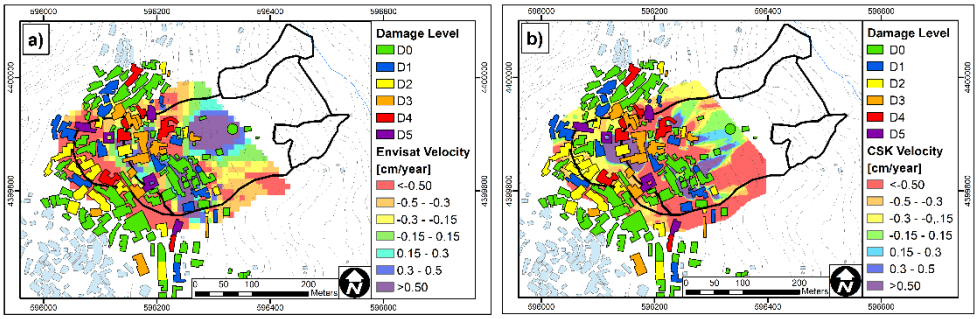

Figure 7.7: A-DInSAR-geotechnical velocity (DGV) map vs. building damage map: a) Envisat (2003-2010) data; b) Cosmo-SkyMed (2012-2014) data (from Peduto et al., 2021).

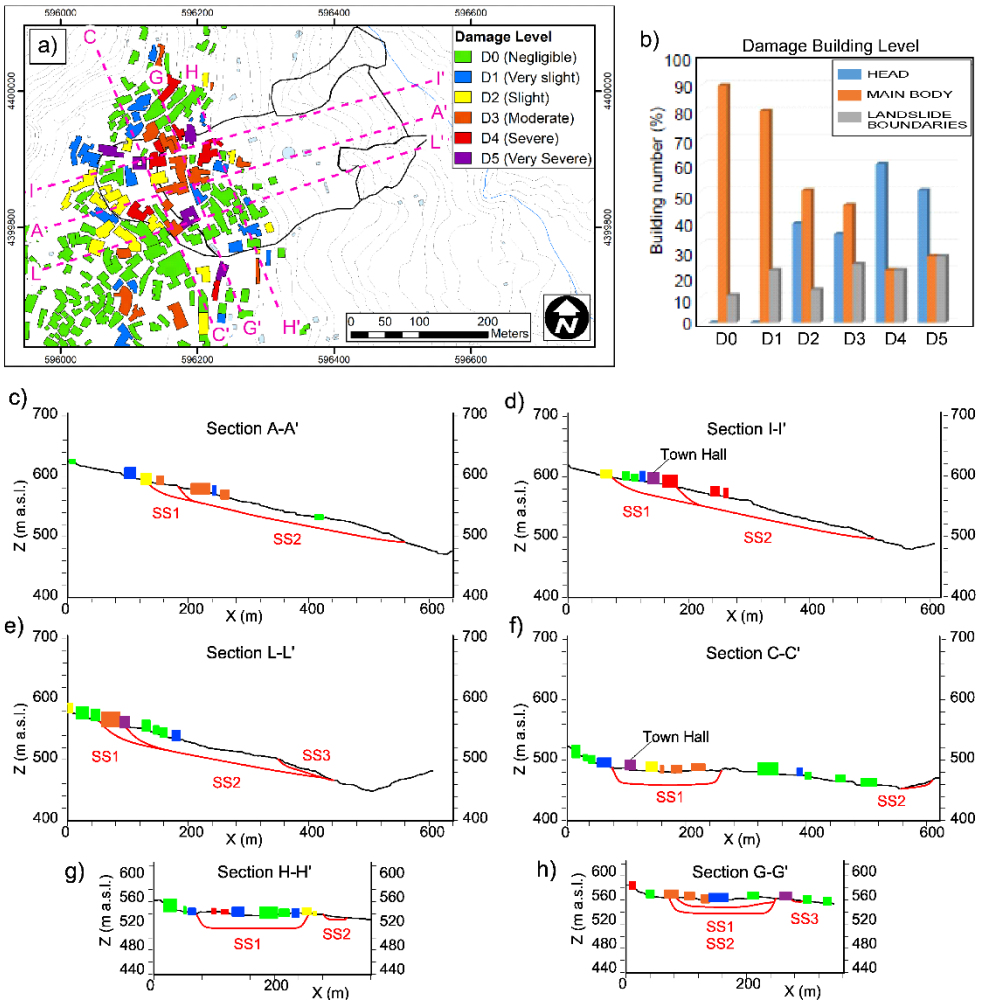

Figure 7.6: a) Distribution map of damage to buildings; b) percentage of buildings located in different landslide zones distinguished according their damage severity level; c) - h) cross sections of the landslide with damaged buildings (from Peduto et al., 2021).

The results show that beside the fact that A-DInSAR data can provide an overview of the kinematics of the landslides – as already pointed out by several Authors (among others, Cascini et al., 2010, 2013; Frattini et al., 2018; Gullà et al., 2017; Wasowski and Pisano, 2019) – their full integration with ground-based geotechnical monitoring data allows deriving the DGV map capable of applying the detailed kinematic information (deriving from inclinometers) within the boundaries of the landslide at hand. To investigate further the link between building damage and the

geometry-kinematics of the landslide phenomenon, one longitudinal and one transverse cross-sections were considered. For these sections, the damage level of the buildings and their position on the landslide profile as well as the velocity along a selected section were correlated. These operations were carried out both for Envisat (Figures 7.8a and 7.8b) and for Cosmo-SkyMed data (Figure 7.8c and 7.8d). The longitudinal section L-L' shows that damaged buildings concentrate between the head of T_D1 and the scarp of T_D2. Furthermore, the velocity trend along the section shows an alternation of negative (downward along the slip surface or downslope along the steepest slope direction, depending on the Type of projection adopted in the specific location) and positive (upward along the slip surface or upslope along the steepest slope direction, depending on the Type of projection adopted in the specific location) values of projected velocity moduli in correspondence of some sectors of the landslide that can be associated with the effects of localized rotational movements.

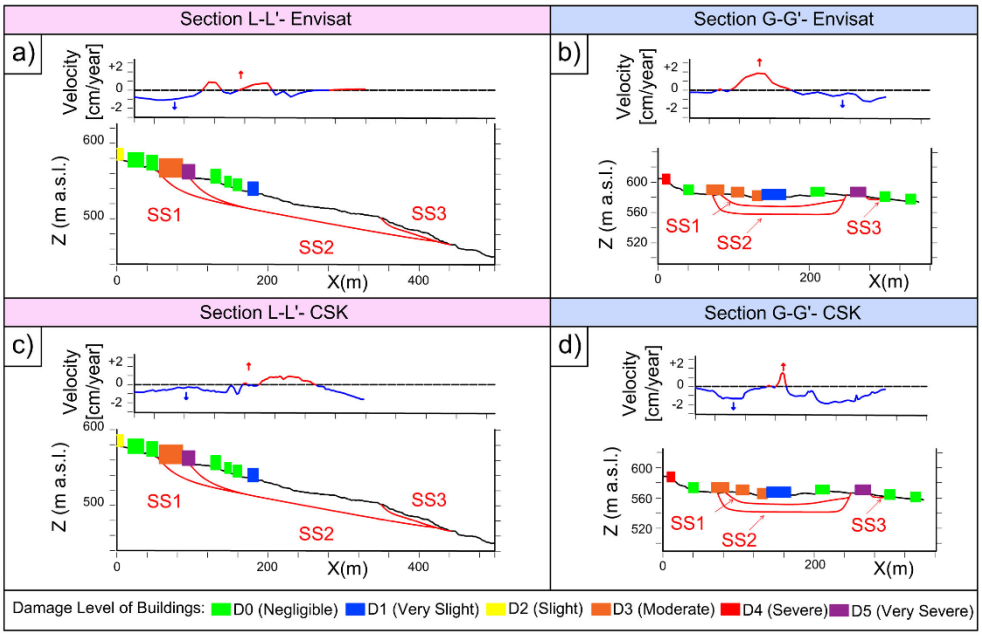

Figure 7.8: Comparison between the damage severity of the buildings and Envisat/Cosmo-SkyMed velocity from DGV map in section L-L' and G-G' (from Peduto et al., 2021).

The G-G' cross-section shows an alternation of negative (downslope/downward) and positive (upslope/upward) values of projected velocity moduli in correspondence of the landslide boundaries due to the presence of a rotational component. Furthermore, the damage distribution for section G-G' confirms that the most severe damage is recorded along (or in proximity of) the landslide boundaries.

The comparison between the damage distribution and the DGV maps showed that the buildings – of masonry type with shallow foundations – located in the landslide-affected area exhibit higher damage severity levels in correspondence of the head, the secondary scarp and the boundaries of the landslide where the highest velocity gradients are recorded and the highest differential settlements may affect buildings located therein (Nicodemo et al., 2017b). However, some local anomalies (i.e., areas with high velocity values within the landslide body) seem to provide an apparent mismatch with the overall kinematics of the phenomenon. For this reason, a more in-depth analysis of the phenomenon was necessary. Knowing that both the geology and soil mechanical properties, although chaotic, are uniformly distributed within the landslide, the presence of any possible local conditioning factors such as sub-services that could interfere with the landslide was analysed. This investigation revealed the presence of some buried channels collecting the runoff water together with the water captured by a drainage tunnel built uphill (Figure 7.9). From the comparison of the Cosmo-SkyMed DGV map (Figure 7.9a) with the tracks of the channels, it seems that the zones with local changes in velocities inside the landslide body are in correspondence of the channels. Furthermore, it also seems that the damage level is higher for buildings close to the channels (Figure 7.9b). Indeed, these latter may have been damaged by the landslide displacements in time and the point-wise water losses may have caused the localized velocity increase and the associated "anomalous" damage severity.

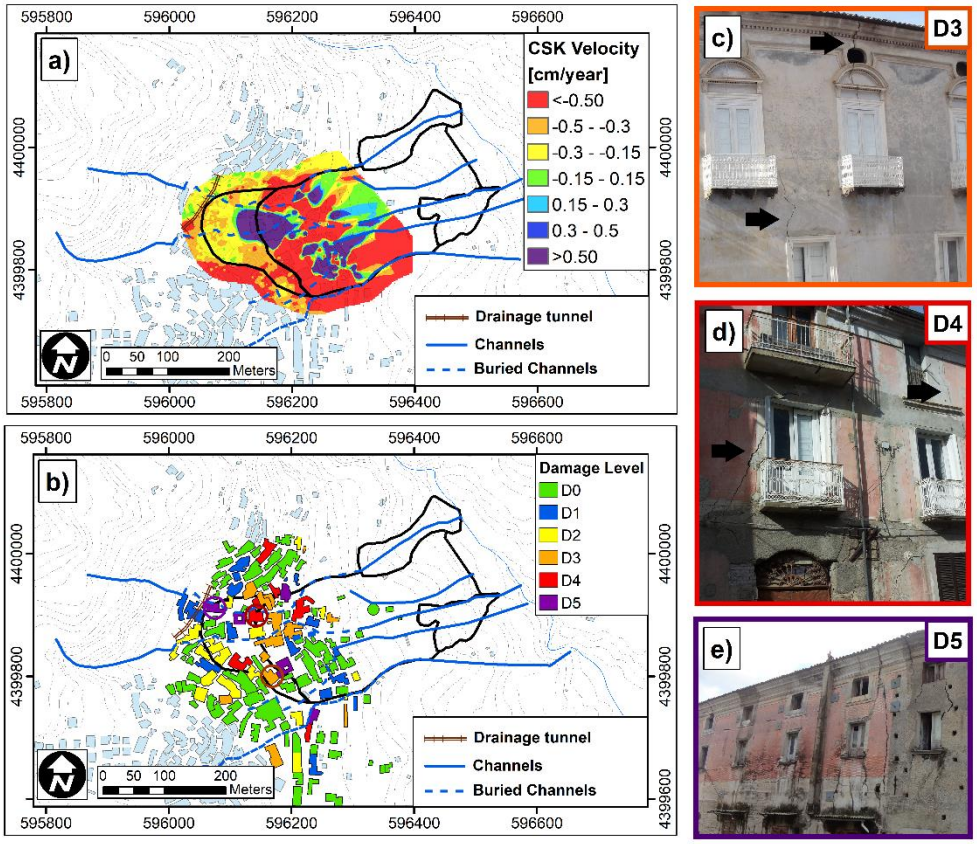

Figure 7.9: Possible conditioning factors of slope instability: a) paths of the buried channels vs. Cosmo-SkyMed velocity; b) paths of the buried channels vs. the damage severity level of the buildings; photos of damaged buildings (labelled with coloured circles in Fig.14b) in proximity of buried channels with indication of damage level: c) D3; d) D4; e) D5 (from Peduto et al., 2021).

The analysis allowed outlining the instability phenomenon affecting the historic centre of Lungro as consisting of a slow-moving landslide with two translational sliding bodies with slight rotational character immediately downstream of the two escarpment sectors.

7.2 Level 2: Limit Equilibrium Analysis

The test landslide in Lungro historical center has been defined as a medium deep of translation-rotational slide (Gullà et al., 2017; Peduto et al., 2021).
The studies carried out in the first level of analysis have made it possible to identify the most representative kinematic section (longitudinal section A-A') for stability analyses in the case of 2D problem. Based on the measurements of the piezometric levels (Figure 6.4), conducted over a significant period from 2007 to 2011 (Gullà, 2014), some possible positions of the phreatic surface have been identified, and therefore different values of pore water pressures, which can be associated with variations in the stability conditions of the analysed landslide. The identified water level, shown in Table 7.2, are identified as below and correspond to defined dates:

- Depressed Ordinary Condition: 27/11/2011
- High Ordinary Condition: 17/10/2007
- Depressed Critical Condition: 01/03/2010
- High Critical Condition: 17/02/2009

In the LEM analysis the slip surfaces of longitudinal sections (see Figure 7.10) have been imposed, fixing the position of the water level as derived from the measured piezometric levels (Table 7.2) and considering values of shear strength parameters (cohesion c' and friction angle ϕ) averagely mobilized to failure and consistent with those detected by the geotechnical laboratory experimentation carried out on the geomaterials that make up the geotechnically significant volume (Gullà and Aceto, 2009).

		Ground water level (meters from ground level)			
		Ordinary		Critical	
Piezometer		17/10/2007 (High)	27/11/2011 (Depressed)	01/03/2010 (High)	17/02/2009 (Depressed)
	S14	-40	-40,2	-39,40	-39,60
	S13	-13,5	-15,7	-9,75	-11,4
	S15	-5,1	-5,4	-4,05	-5

Table 7.2: Ground water levels

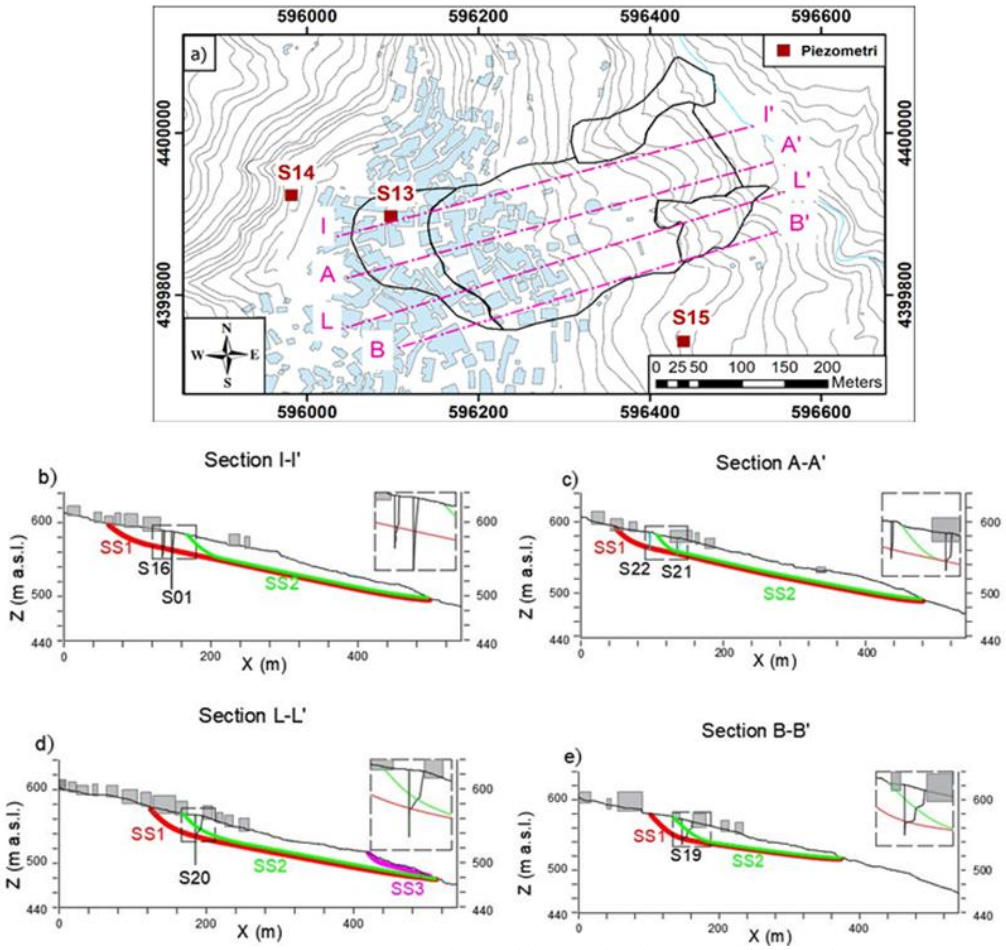

Figure 7.10: Section plan and longitudinal sections (from Peduto et al., 2021).

The analyses carried out with the limit equilibrium method allow to achieve the following goals:

1. Calibration of representative shear strength parameters (c, ϕ) for the representative longitudinal section (A-A') considering 4 phreatic levels (GOAL 1);
2. Investigation of the 3D effect on the stability conditions: comparison of the FS between the 4 different longitudinal sections (GOAL 2).

The analyses were conducted with the Geostudio Software. The analyses were carried out using the method proposed by Morgesten and Price and the materials are modelled with Mohr Coulomb's failure criterion. From the results of the phenomenological analyses it has been possible to deduce that the soil affected by the landslide phenomenon is characterized by the presence of chaotic phylladi with coarse-grained soils strongly degraded and altered in the superficial part (refer to the paragraph 6.1). Therefore, in the limit equilibrium analysis it has been assumed, in a first phase, that the subsoil could be assimilated to a homogeneous geomaterial (Figure 7.11).

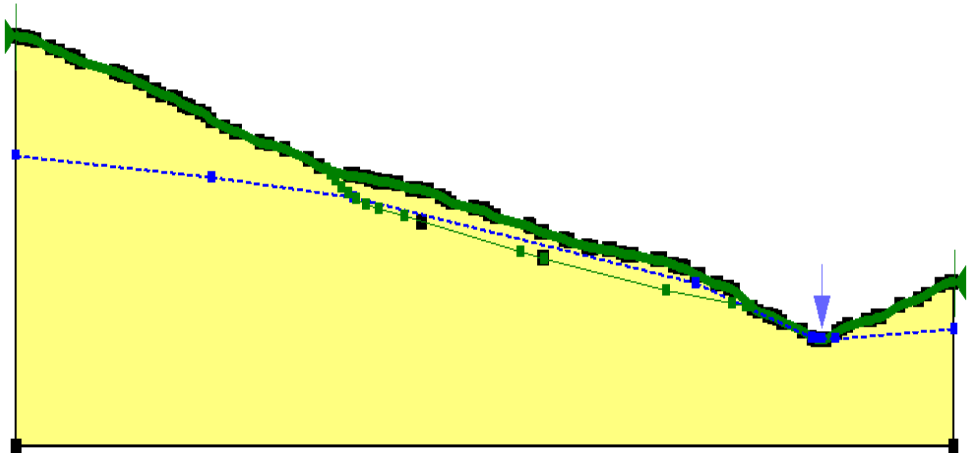

Figure 7.11: Longitudinal cross-section A-A' model on Geostudio software

For the slip surface 1 of the longitudinal section A-A' and for the 4 groundwater conditions, possible combinations of c and ϕproviding a safety factor FS=1 have been identified (Figure 7.12). These values allowed defining a "domain" of the parameters c and ϕ, which representsthe pairs of values parameters that lead, for the other fixed conditions, to a value of F = 1.

Depressed Ordinary FS=1		
c'	φ	FS
[kPa]	[°]	
0	14.5	1,002
5	13.4	1,004
10	12.3	1,000
15	11.3	1,003
18	10.6	0.999
20	10.2	1

High Ordinary FS=1		
c'	φ	FS
[kPa]	[°]	
0	15.2	1,001
5	14.1	1,000
10	13	1,000
15	11.9	1,000
18	11.3	1.004
20	10.8	1,001

Depressed Critical FS=1		
c'	φ	FS
[kPa]	[°]	
0	15.5	1,004
5	14.4	1,004
10	13.3	1,004
15	12.1	0.9999
18	11.5	1,004
20	11	1,001

High Critical FS=1		
c'	φ	FS
[kPa]	[°]	
0	16.2	1,002
5	15	0.999
10	13.9	1,002
15	12.7	1,001
18	12	1,001
20	11.5	1,000

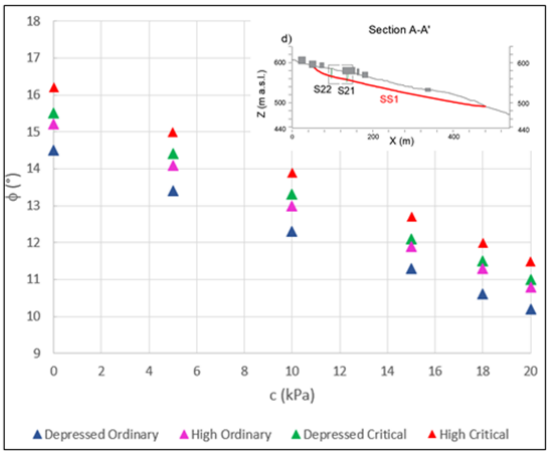

Figure 7.12: Pairs of values c and ϕ for the 4 groundwater conditions and "field of existence" for FS=1

Once defined this domain, 10 different combinations of c and ϕ values have been identified to investigate possible 3D effect on the stability conditions (Goal 2). These combinations were obtained by identifying the cohesion values obtained by intersecting the lines FS=1 for the 4 different groundwater conditions with the values of friction angle (ϕ) corresponding to a cohesion value equal to 0, i.e. equal to 14.5,15.2,15.5 and 16.2 (Figure 7.13). These parameters were assumed by referring to the set of pairs c and ϕ (peak and residue) defined for the geomaterials of interest from the laboratory experimentation.

Combination	c	ϕ
1	0	14.5
1a	3.18	14.5
1b	4.52	14.5
1c	7.27	14.5
2	0	15.2
2a	1.4	15.2
2c	4.27	15.2
3	0	15.5
3a	3	15.5
4	0	16.2

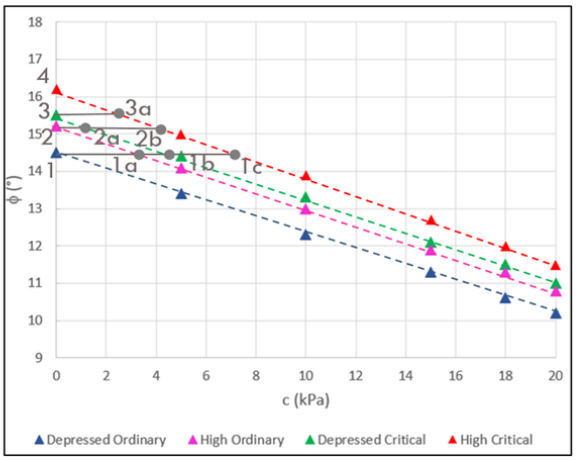

Figure 7.13: Combination of pairs c and ϕ

Stability analyses were carried out for all longitudinal sections (A-A', B-B', I-I' and L-L') in order to verify the presence of a three-dimensional effect. In particular, using the values of c and ϕ falling in the domain defined for section A-A', the safety factors FS have also been calculated for the other longitudinal sections. The analyses were carried out for the SS1 slip surface (Figure 7.9c), for all 4 groundwater conditions and for the two different water level conditions "Z" in the Tiro river, downstream of the longitudinal section A-A ' (the minimum value equal to 0 meter and the maximum value that varies depending on the groundwater condition).

In the case where the FS values of the longitudinal sections B-B', I-I' and L-L' are similar to those of section A-A', then it can be inferred that the unstable conditions are homogeneous inside the body of landslide and the three-dimensional contribution in conditions of failure in the case study is not significant. Indeed, the results obtained from the limit equilibrium analysis for all 4 longitudinal sections (Figures 7.14) show a homogeneous trend of safety factor with the variation of the resistance parameters (c, ϕ).

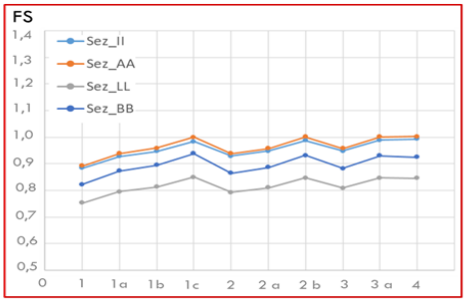

FS values for High Critical Condition and Z=3 m

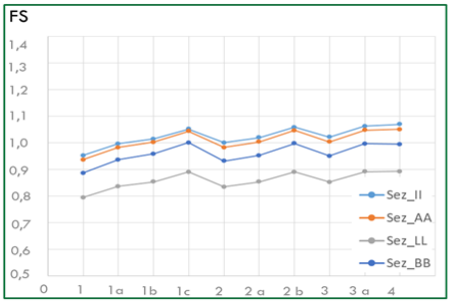

FS values for Depressed Critical Condition and Z=2 m

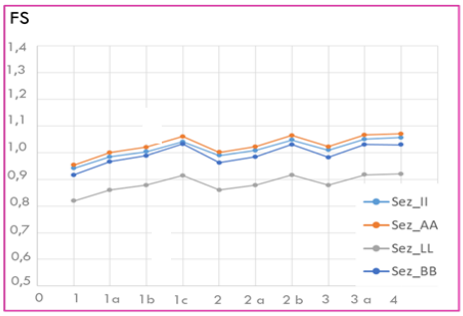

FS values for High Ordinary Condition and Z=1 m

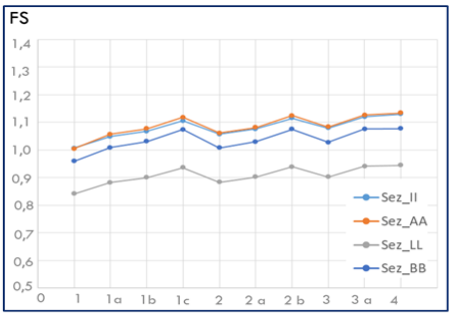

FS values for Depressed Ordinary Condition and Z=0,5 m

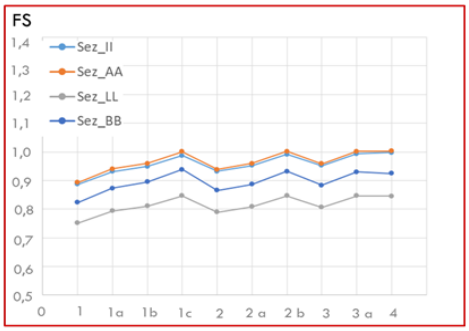

FS values for High Critical Condition and Z=0 m

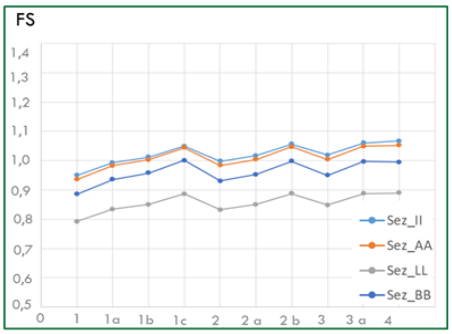

FS values for Depressed Critical Condition and Z=0 m

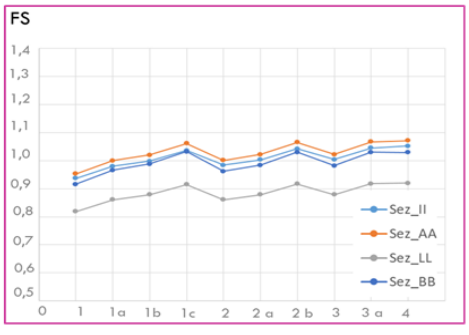

FS values for High Ordinary Condition and Z=0 m

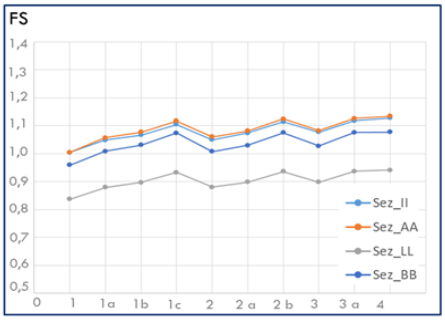

FS values for Depressed Ordinary Condition and Z=0 m

Figure 7.14: LEM Analysis Results

From the obtained results, the following conclusions can be drawn:

- for all 4 conditions of groundwater level the safety factors (FS) do not depend on the value of the water level in the Tiro river (Z);
- the spatial variability of the FS investigated for longitudinal cross sections in the Goal 2 shows that the three-dimensional effects in condition of failure are negligible. In fact, the variation of FS, with the same boundary conditions for all the sections, is irrelevant and could be linked to the different geometries of the sections or to the different degrees of soil alteration and therefore to the different resistance parameters (residual cohesion and angle of friction).

7.3 Level 3: FEM Analysis

Following the LEM analysis, with which it was possible to identify strength parameters (c and ϕ) averagely mobilized to failure, the study focused on the finite element modelling of the most representative kinematic longitudinal section (section A-A'). This analysis was carried out with the software FEM Plaxis 2D that starting from the results of the first two phases of analysis (phenomenological and limit equilibrium analysis) was carried out to calibrate the elastoplastic parameters of the soils (in particular the deformability parameters). Finite element FEM analyses have been carried out taking into account the various requirements that allow the correct definition of the stress state, including the geological history of the slope, the pore water pressure regime and a correct choice of the constitutive model to be assigned to the materials involved (Duncan, 1996; Viscardi, 2010).

For the calibration of the model, the cumulative displacement measured from the inclinometers for the period 2006 to 2010 was assumed as the control parameter. This displacement was compared with a cumulative displacement over time defined by the sum of the plastic displacements modeled with the finite

elements for the different levels of groundwater that occurred over the period of time considered. In particular, the displacements obtained from the model in correspondence of ground level in the location of S21 and S22 inclinometers along the longitudinal section A-A', were compared with those measured in situ by the mentioned inclinometers. The variation of the water level (High Ordinary, High Critical, Depressed Ordinary and Depressed Critical) that influences the measured displacements was taken into account. For this reason, the displacements of the inclinometers S21 and S22 have been plotted against the time (Figure 7.15) and it has been seen that in a time span of approximately 5 years (time interval in which inclinometric data are available) there are 3 phases with homogeneous displacement velocity; these latter were correlated to 3 different groundwater conditions: one with High Ordinary (n.2), one with High Critical (n. 3) and another with Depressed Critical (n.1). The fourth event (n.4) exhibits a slope equal to that of the event n.2 and therefore corresponds to another movement event with High Ordinary water level. Instead, the last section of the diagram refers to a still ongoing displacement phase of the landslide because the displacement rates do not show a variation. For this reason, in the analyses carried out only the first 4 events were considered.

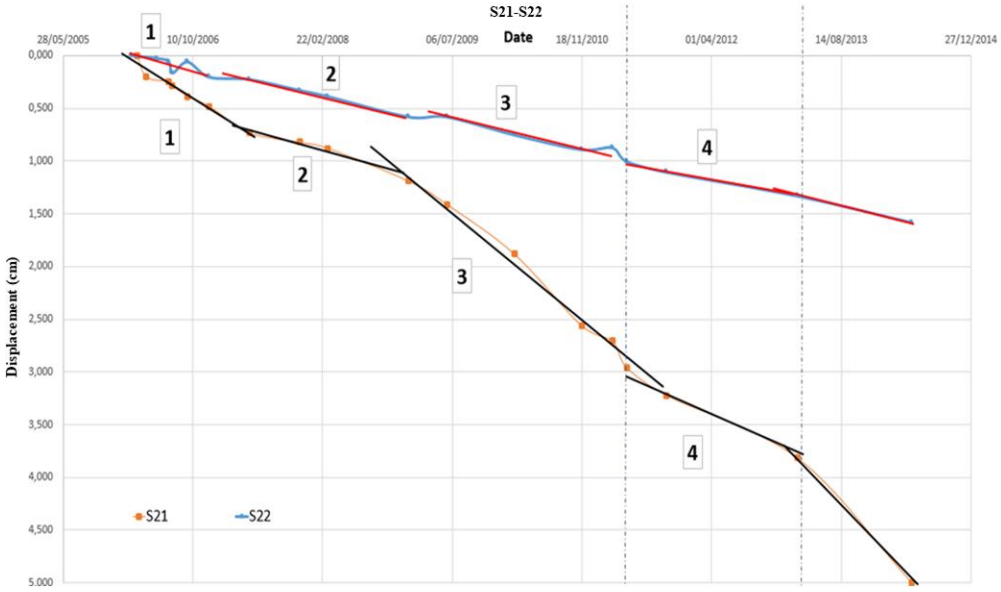

Figure 7.15: Displacement velocity of inclinometers S21 and S22

For these events and for each inclinometer, displacement velocities were calculated and the values in Table 7.3 were obtained.

Inclinometer	V_{1event} [cm/year]	$V_{2event} = V_{4event}$ [cm/year]	V_{3event} [cm/year]
S21	0,5754	0,4145	0,6148
S22	0,181	0,198	0,195

Table 7.3: Displacement velocity for different events

For the S22 inclinometer the displacement velocity difference for the various events is almost negligible, whereas for the S21 inclinometer these differences are more evident. Therefore, for the purpose of calibration of the model, the displacements cumulated at the end of each of the 3 events were considered; the cumulated displacement at the end of the 4th event was used to verify the model created on Plaxis. In the analyses carried out, the behavour of the soils has been assumed as elastic perfectly plastic behaviour with Mohr Coulomb's yield criterion and non-associated plastic flow law, in this case the friction angle ϕ' coincides with the dilatance angle ψ (Griffiths, 2007; Lollino, 2014; Bru, 2018; Conte, 2020).

For finite element modelling, it was first necessary to define the geometry of the model. So starting from the results of the Level 1 and Level 2 of the analysis, the soil stratigraphy, the shape of the slip surfaces and the strength parameters (cohesion c and friction angle ϕ) mobilized on the slip surfacewere defined. However, the presence of a high density of buildings and the particular complexity of the geomaterials present in the landslide site makes it difficult to identify some geotechnical parameters that are important for modeling in terms of stress-strain. Therefore, starting from the results of the first two levels of analysis it was necessary to calibrate the value of the Young modulus (E) and the resistance parameters (cohesion and friction angle) present before the activation of the landslide within the shear band. For this purpose, a calibration procedure "trial and error" was used. Subsequently, the values of mentioned parameters obtained from the calibration were validated through the comparison of the displacements modelled on Plaxis with those measured from the inclinometers and from the satellite data.

The geomorphological study and the inclinometric data showed that within the longitudinal section A-A' there are two different slip surfaces that in Plaxis 2D have been modelled through the construction of two shear bands, each with a thickness of about 1.5 meters (De Novellis et al., 2018, Lollino, 2014; Viscardi, 2010).

In order to take into account the different genesis of the slip surface and the different magnitude of the displacements measured in situ by the S21 and S22 inclinometers, it was necessary to consider different soil alteration. For this reason, in the two shear bands different types of soil were assigned, with different mechanical characteristics. In particular, to these soils the shear strength parameters (cohesion c and friction angle ϕ) have been assumed intermediate between peak and residual values.

In addition, to model a displacement as close as possible to inclinometric displacements, within the shear bands it was necessary to assign a value of the Young modulus much smaller than the surrounding soil (Castaldo et al.2017).

Figures 7.16 and 7.17 show the two longitudinal sections that have been taken into consideration for the finite element analysis. In particular, since the landslide evolution history is unknown, two different scenarios have been hypothesized:

- ***Hypothesis 1 - HYP 1:*** longitudinal section A-A a first deeper slip surface (SS1) was generated that still affects the entire slope and then inside it is a smaller slip surface (SS2) formed more recently;

- ***Hypothesis 2 - HYP 2***: retrogressive landslide (Figure 7.17). Within the longitudinal section A-A' first a slip surface was generated that starts from the middle of the slope (SS2) and then a sort of retrogressive smaller sliding surface (SS1) more recently originated.

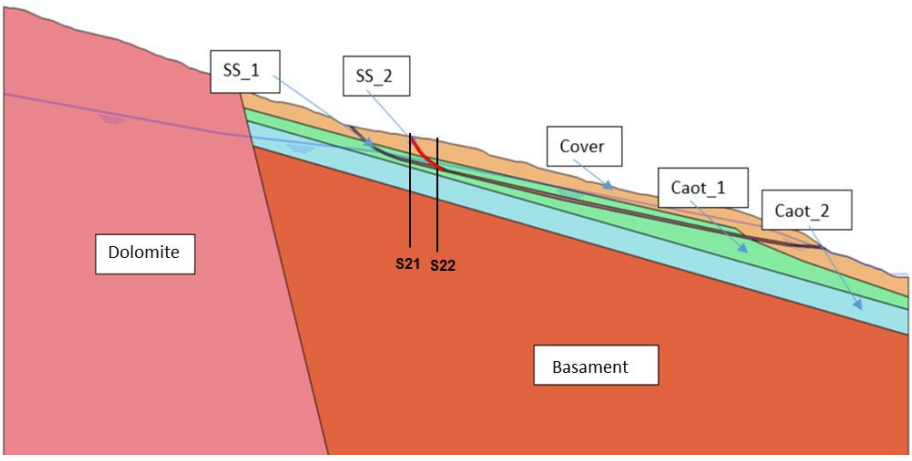

Figure 7.16: Longitudinal section model A-A' on PLAXIS 2D – Hypothesis 1

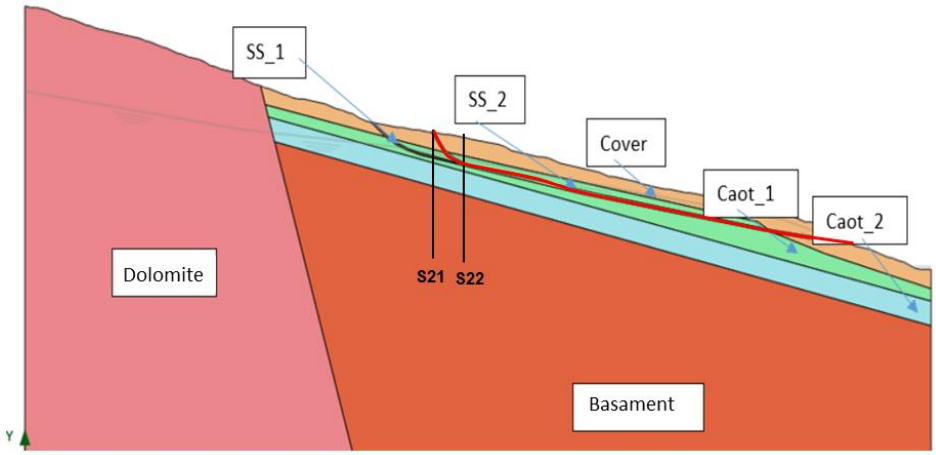

Figure 7.17: Longitudinal section model A-A' on PLAXIS 2D – Hypothesis 2

For the purpose of reconstruction of the stress strain state of the landslide soils one of the most important phases involved generation of the "***mesh"*** calculation. In order to identify a number of elements that do not alter the results and does not involve a considerable amount of time, a sensitivity analysis of the safety factor FS= 1 was carried out that led to a number of 15-node-elements equal to 2872 and a number of nodes equal to 23357. For the correct modelling of the landslide it was necessary to take into account the topographic surface trend (whose elevation varies between 600 and 200 m) and the stratigraphy of the soils. The boundary conditions of the model were represented by limited horizontal and vertical displacements and rotations along the lower edges and limited rotations and horizontal displacements along the lateral edges (Plaxis manual, 2020).

The FEM analysis was conducted for longitudinal section A-A' and was divided into two calculation stages:

- ***Initial phase***: Fundamental importance is the correct determination of the initial stress condition. For this purpose, a type of Plastic calculation called ***Gravity Loading*** was used (implemented within the calculation code PLAXIS, 9.2). This procedure generates the initial stresses based on the volumetric weight of the soil (Reference, Plaxis Manual). The value of the lateral thrust coefficient K0 is expressed by the relation (/'ν1 ν-'). Above the groundwater level, the vertical and total effective stresses coincide. Moreover, in order to generate an initial state stress a stationary water level was assumed and equal to the Ordinary Depressed;

- ***Plastic Analysis***: in order to identify the mechanisms of landslide body deformation the analyses were carried out in Plaxis using the procedure called ***Plastic***. The analyses were carried out for all 3 different levels of ground water: High Ordinary, Depressed Critical and High Critical. In this analysis the c and ϕ reduction is allowed only for the two soils present within the shear bands.

Therefore, to calibrate the FEM model a total displacement "S_{mod}" was defined, given by the sum of the displacements measured in the first 3 events correlated to the 3 groundwater conditions: High Ordinary, High Critical and Depressed Critical.

$$S_{mod} = S_{1event} + S_{2event} + S_{3event}$$

This defined displacement was then compared with that measured in situ by the inclinometers. Instead for the validation of the model a cumulative modelled displacement "$S_{mod,\ cumulated}$" was defined by adding the total displacement that was obtained in Plaxis in correspondence of the 4th event and therefore with High Ordinary water level:

$$S_{mod,\ cumulated} = S_{mod} + S_{2event}$$

This displacement was compared with the cumulated one measured by the inclinometer on the date corresponding to the end of the 4th event (Figure 7.15).

HYP 1

The calibration procedure took as input parameters those obtained from the limit equilibrium analyses. Through a "trial and error" procedure the resistance parameters shown in Table 7.4 were obtained.

Soil	E (MPa)	c (kN/m²)	ϕ (°)	v	γ_{unsat} (kN/m³)	γ_{sat} (kN/m³)
Cover	50	30	26	0,25	22	23
Caot_1	600	50	33	0,25	23	24
Caot_2	5000	100	35	0,25	23	24
Phyllite/Basament	10.000	200	45	0,30	23	24
Dolomite	40.000	900	58	0,45	27	28
SS_2	17	17	17	0,25	23	24
SS_1	12,5	12,5	15	0,25	23	24

Table 7.4: Soil parameters HYP 1

Therefore, with these values of the shear parameters (c and ϕ) and of the Young modulus (E), the horizontal displacements were calculated at the S22 and S21 inclinometers for the three different groundwater conditions as shown in Figures 7.18,7.19, 7.20, 7.21, 7.22 and 7.23.

- ***Inclinometer S22 – High Ordinary water level***

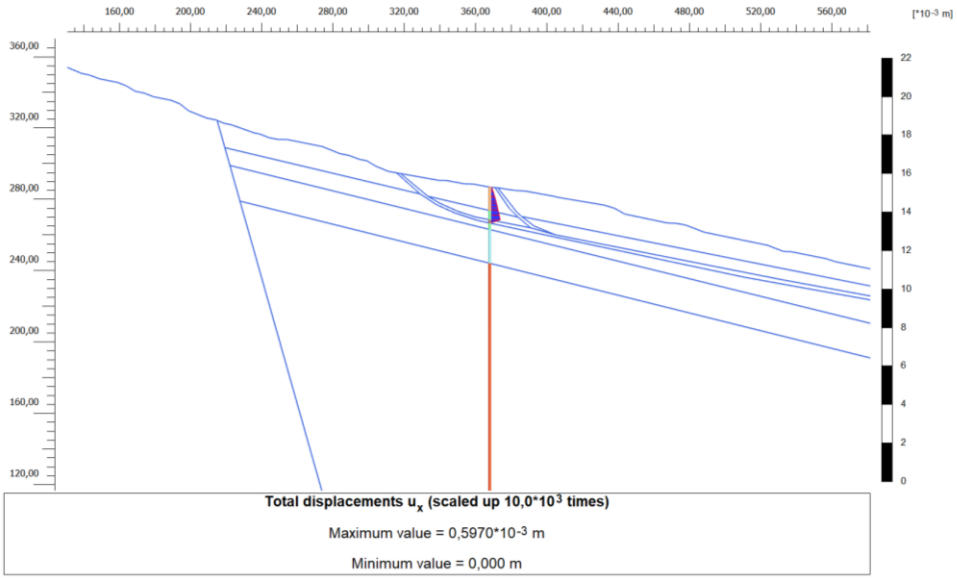

Figure 7.18: Horizontal displacements at the inclinometer S22 – High Ordinary water level HYP 1

- ***Inclinometer S22 – Depressed Critical water level***

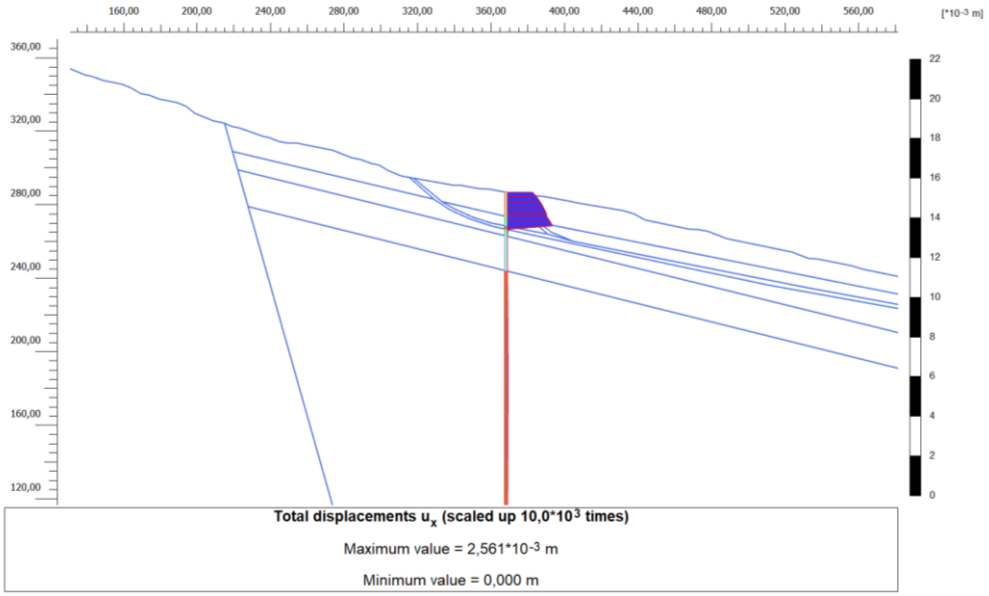

Figure 7.19: Horizontal displacements at the inclinometer S22 – Depressed Critical water level HYP 1

- ***Inclinometer S22 – High Critical water level***

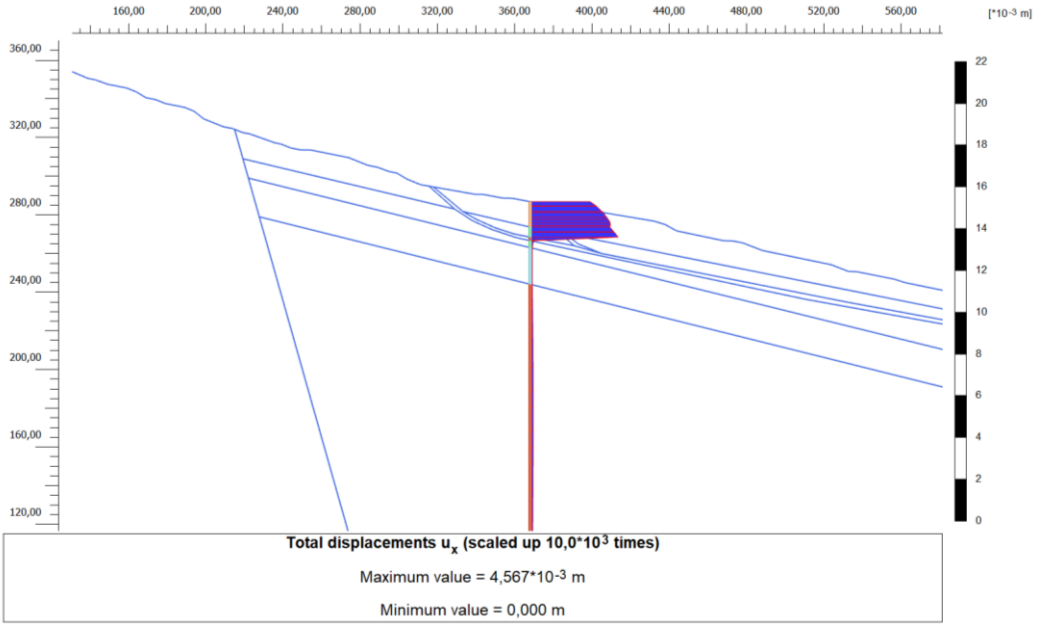

Figure 7.20: Horizontal displacements at the inclinometer S22 – High Critical water level HYP 1

- ***Inclinometer S21 – High Ordinary water level***

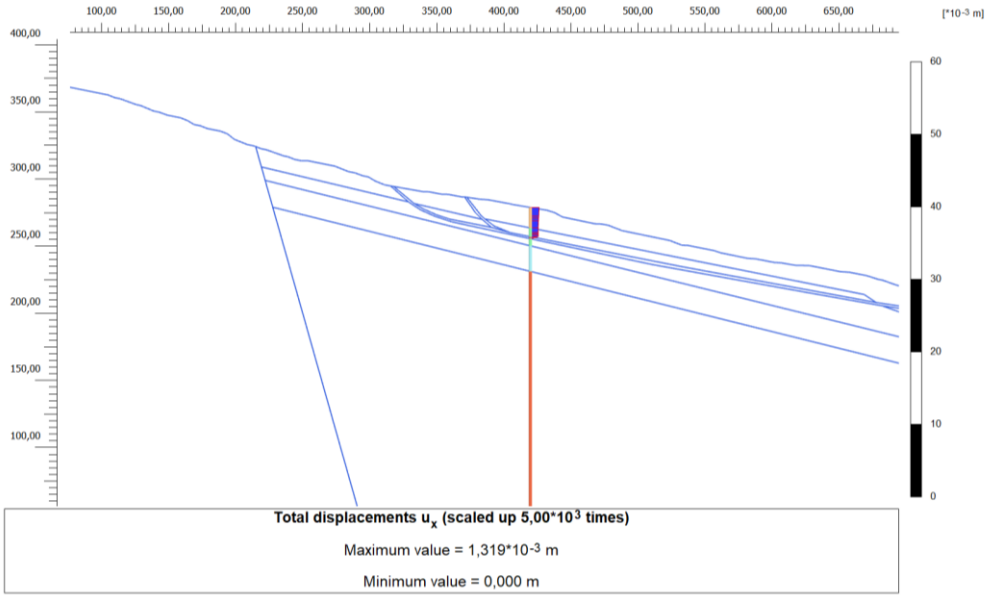

Figure 7.21: Horizontal displacements at the inclinometer S21 – High Ordinary water level HYP 1

- ***Inclinometer S21 – Depressed Critical water level***

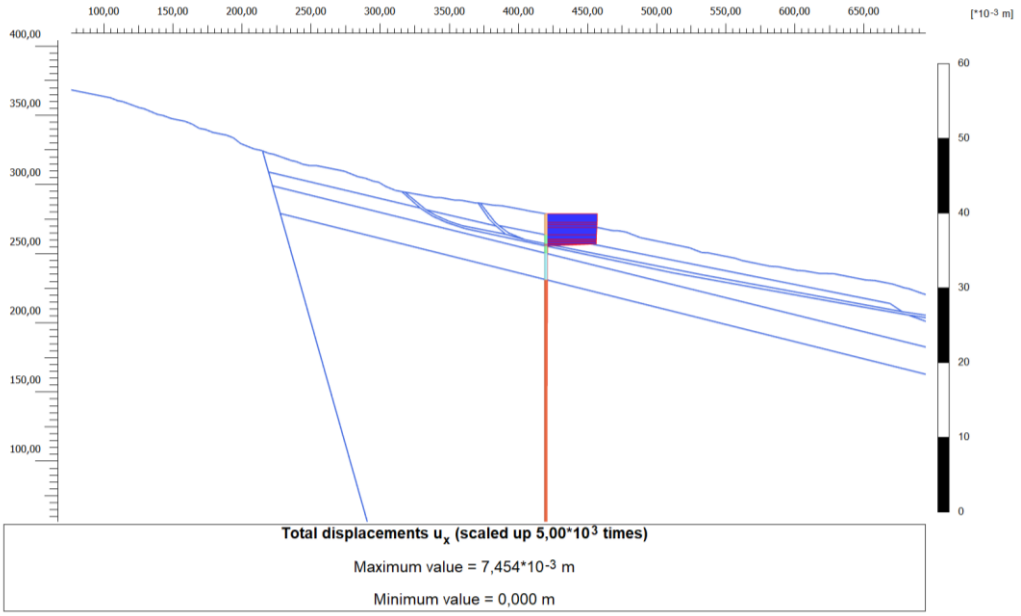

Figure 7.22: Horizontal displacements at the inclinometer S21– Depressed Critical water level HYP 1

- ***Inclinometer S21 – High Critical water level***

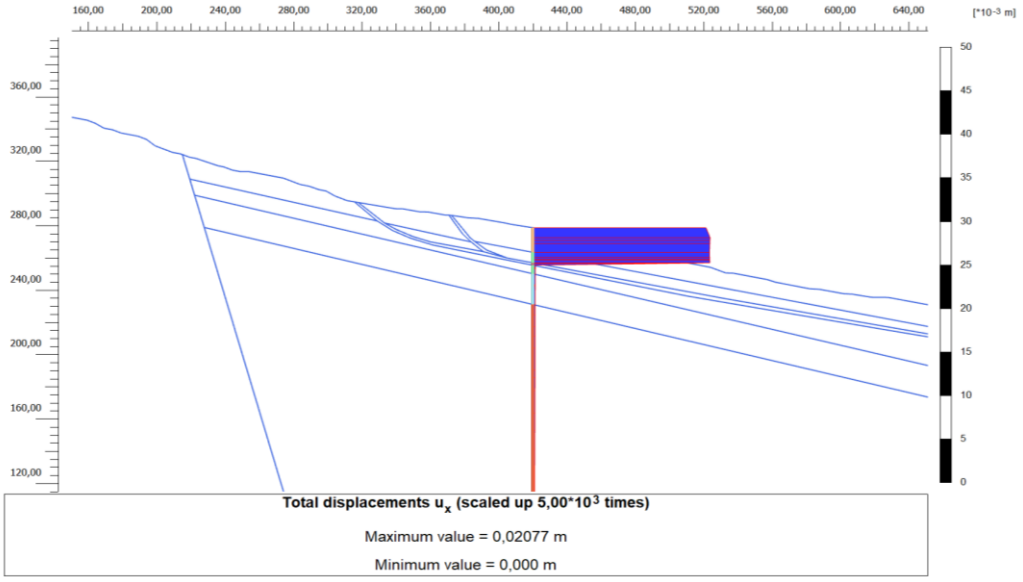

Figure 7.23: Horizontal displacements at the inclinometer S21 – High Critical water level HYP 1

Therefore the displacements modelled and those measured are as follows:

S_{incli}^{S21}= 3,00 cm S_{mod}^{S21}= 29,54 x10 -3 m= 29,54 mm= 2,96 cm

S_{incli}^{S22}= 1,00 cm S_{mod}^{S22} = 7,66 x10 -3 m= 7,66 mm = 0,77 cm

HYP 2

The same analyses were carried out for the second hypothesis of landslide and the following strength parameters and displacement values were obtained.

Soil	E (MPa)	c (kN/m²)	ϕ (°)	v	γ_{unsat} (kN/m³)	γ_{sat} (kN/m³)
Cover	50	30	26	0,25	22	23
Caot_1	600	50	33	0,25	23	24
Caot_2	5000	100	35	0,25	23	24
Phyllite/Basament	10.000	200	45	0,30	23	24
Dolomite	40.000	900	58	0,45	27	28
SS_2	15	8	16	0,25	23	24
SS_1	15	8	16	0,25	23	24

Table 7.5: Soil parameters HYP 2

With these parameters the following horizontal displacements have been calculated in correspondence of the inclinometers:

S_{incli}^{S21}= 3,00 cm S_{mod}^{S21}= 29,1 x10 $^{-3}$ m= 29,1 mm= 2,91 cm

S_{incli}^{S22}= 1,00 cm S_{mod}^{S22} = 4,8 x10 $^{-3}$ m= 7,66 mm = 0,48 cm

The results obtained from the two landslide hypotheses allow arguing that modelling version that best reflects the genesis of the sliding surfaces is the HYP 1. Interestingly, the presence of an older deeper sliding surface with a more recent originated in the upeer central part also matches satellite measurements.

In fact, from the results obtained from the first level of analysis, the DGV maps show that within the landslide the displacement velocities are not constant. In particular, for the ENVISAT database (Figure 7.5c), the displacement velocities detect a single deeper sliding surface, while with the COSMO Sky-Med (Figure 7.5d) a more superficial and faster one is found inside the deeper landslide.

Therefore, only HYP 1 was validated by considering also the 4th event. Accordingly, the following value of cumulative horizontal displacements were obtained:

S_{incli}^{S21}= 3,82 cm S_{mod}^{S21}= 29,54 + 1,32 mm= 30,09 mm= 3,09 cm

S_{incli}^{S22}= 1,33 cm S_{mod}^{S22} = 9,55 + 0,77 mm= 10,26 mm = 1,03 cm

After validating the HYP 1 model, for the kinematic representative section (section A-A') the values of total displacements were computed (Figures 7.24, 7.25 and 7.26).

- ***High Ordinary water level***

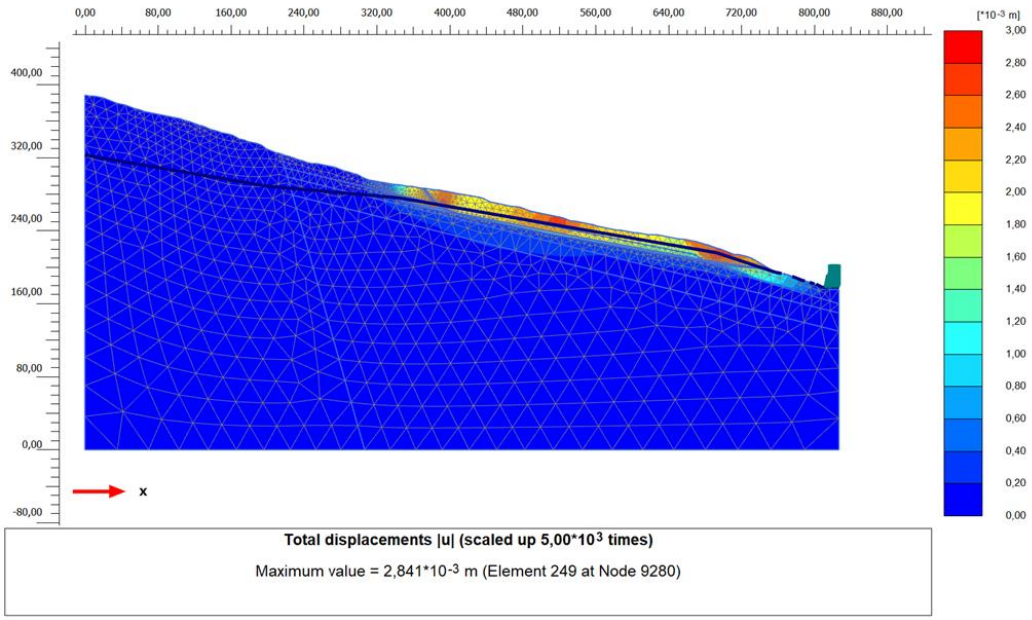

Figure 7.24: Total displacements – High Ordinary water level HYP 1

- ***Depressed Critical water level***

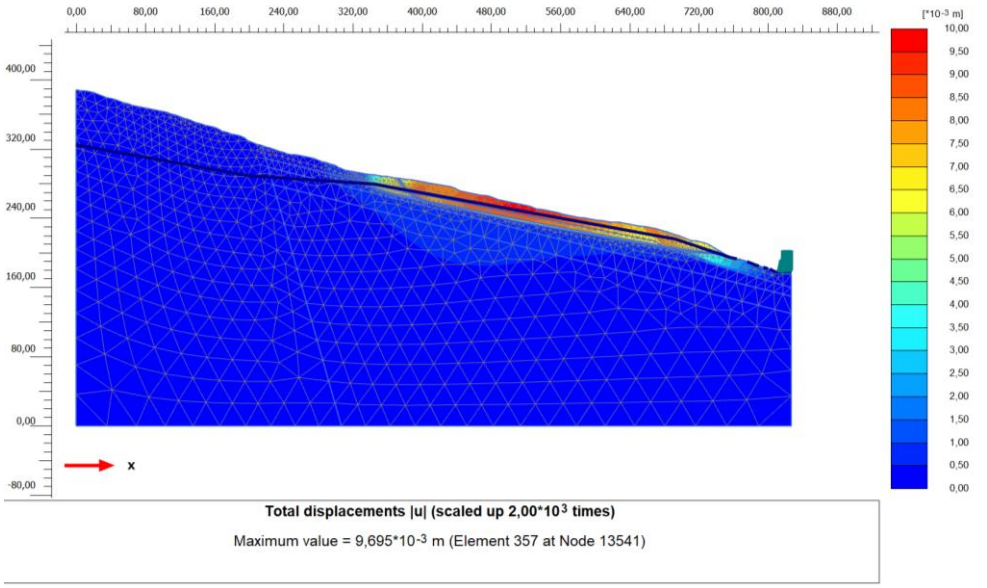

Figure 7.25: Total displacements – Depressed Critical water level HYP 1

- ***High Critical water level***

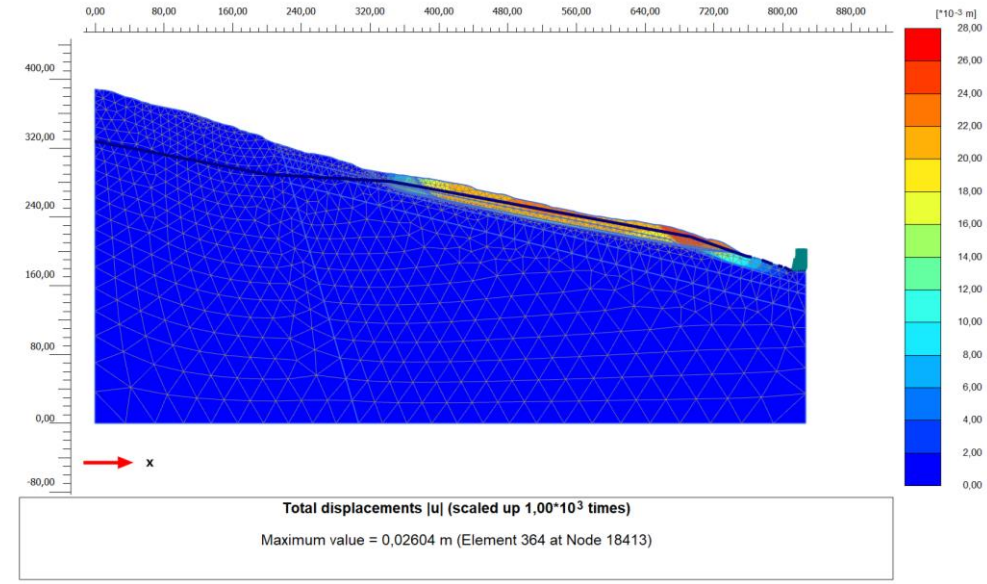

Figure 7.26: Total displacements – High Critical water level HYP 1

7.3.1 Influence Building loads

The calibration of the shear strenght parameters was carried out using a simplified finite element modelling, which disregarded the presence of the buildings. Therefore, before proceeding with the subsequent analyses it was necessary to verify the building influence on the landslide movement. In order to create a two-dimensional modelling of buildings loading, it was assumed that only half of the overall building load acts on the longitudinal section A-A '. The load for each building was calculated considering the maximum number of floors (equal to 3 floors) and assuming that the load was transferred directly below the building and at a depth equal to 2 meters from the ground floor (Figure 7.27).

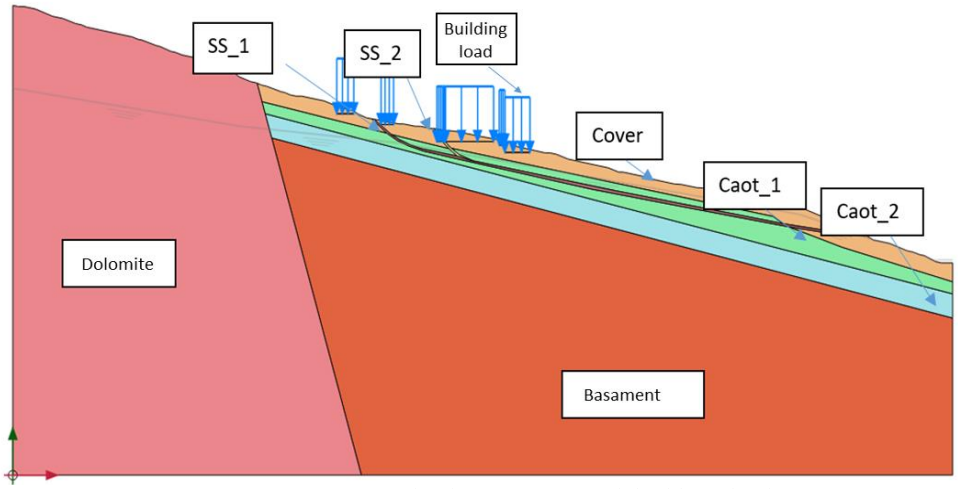

Figure 7.27: Longitudinal section A-A' with buildings loads

Taking into account the typical construction type of the Lungro historic center an inter-floor height of 3 meters and a width of 6 meters (transversal dimension to longitudinal section) was assumed. In addition, for the calculation of the building weight, a wall thickness of 60 cm was considered (Nicodemo et al. 2018).

Therefore, the total load that was applied along section A-A' in the HYP 1 in correspondence of the buildings is equal to:

$$Q_{buildings} = 80 \text{ kN/m}$$

Hereafter the plot of modelled horizontal displacements at the S21 and S22 inclinometers for longitudinal sections A-A' with buildings loads are shown (Figures 7.28, 7.29, 7.30, 7.31, 7.32 and 7.33).

- ***Inclinometer S22 – High Ordinary water level***

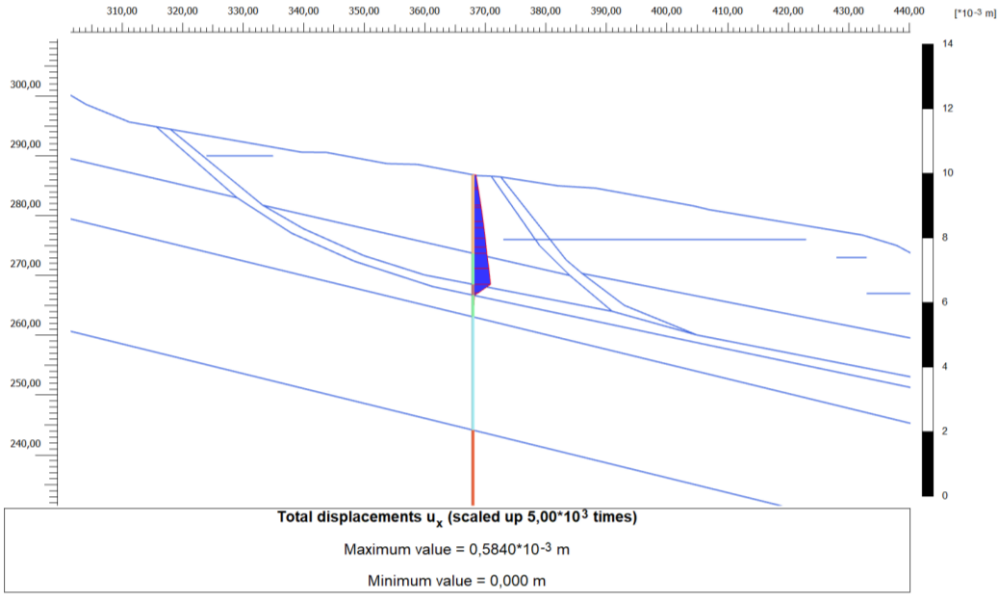

Figure 7.28: Horizontal displacements at the inclinometer S22 – High Ordinary water level HYP 1 with buildings loads

- ***Inclinometer S22 – Depressed Critical water level***

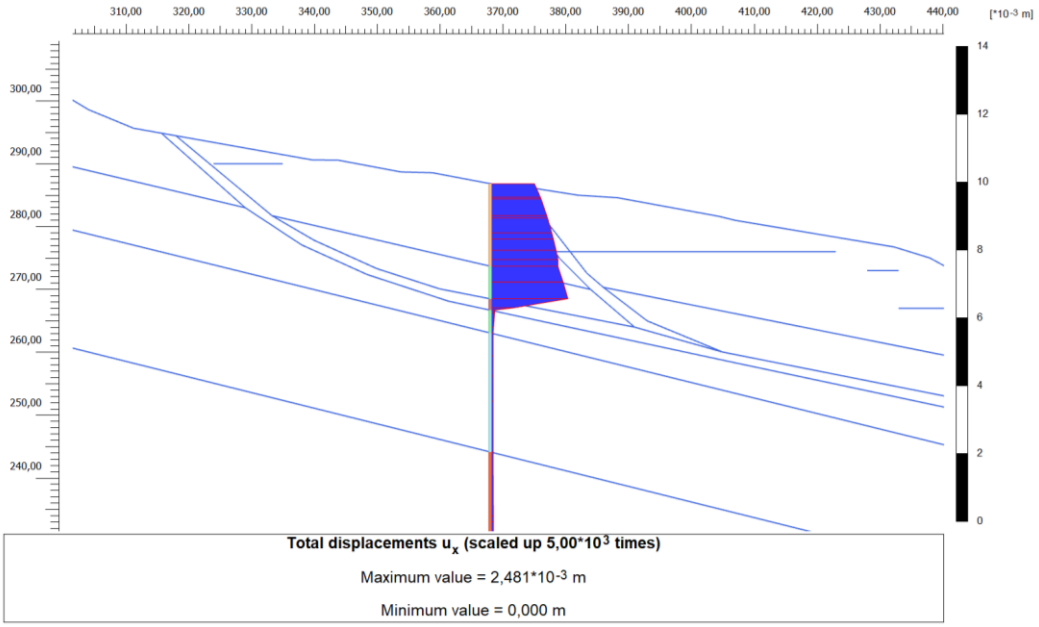

Figure 7.29: Horizontal displacements at the inclinometer S22 – Depressed Critical water level HYP 1 with buildings loads

- ***Inclinometer S22 – High Critical water level***

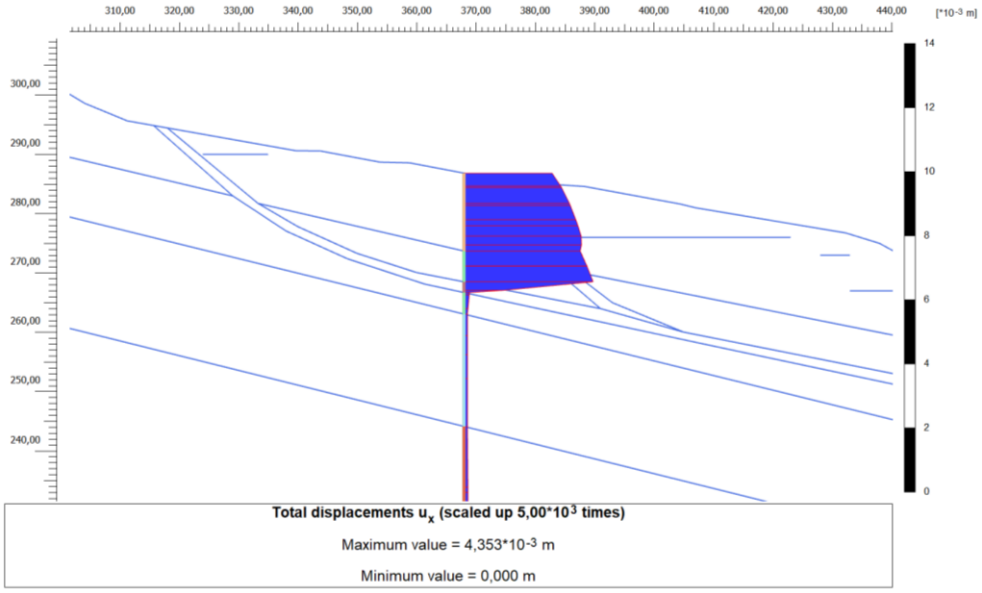

Figure 7.30: Horizontal displacements at the inclinometer S22 – High Critical water level HYP 1 with buildings loads

- ***Inclinometer S21 – High Ordinary water level***

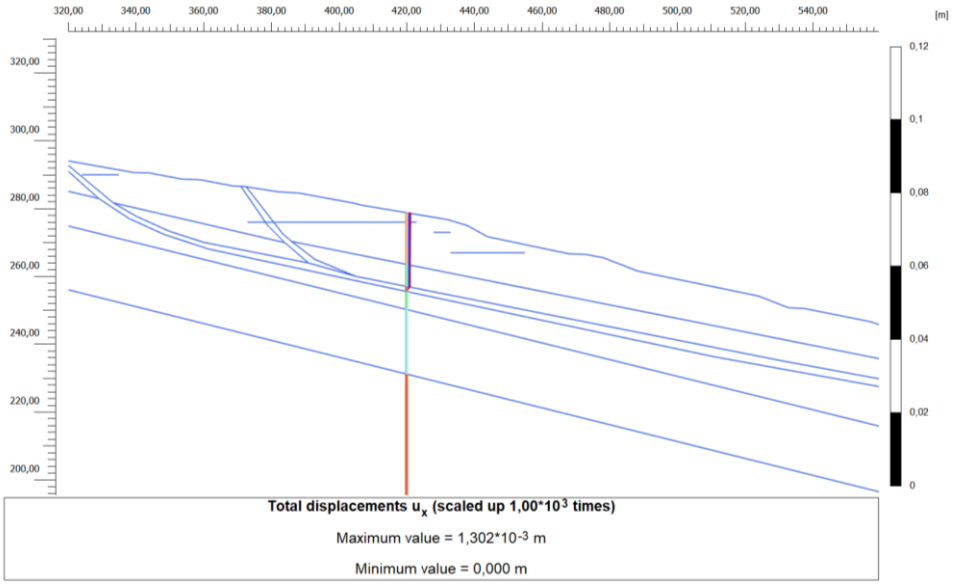

Figure 7.31: Horizontal displacements at the inclinometer S21 – High Ordinary water level HYP 1 with buildings loads

- ***Inclinometer S21 – Depressed Critical water level***

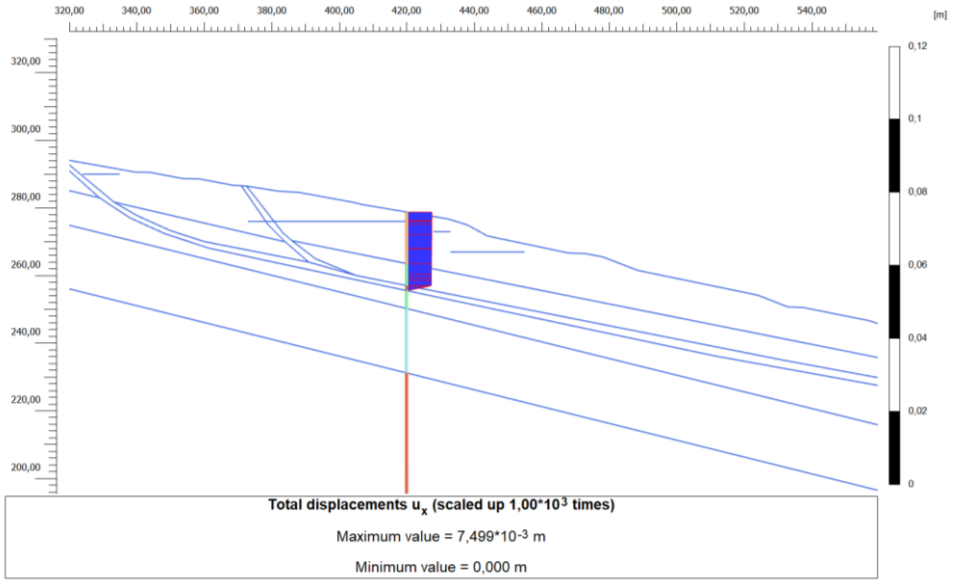

Figure 7.32: Horizontal displacements at the inclinometer S21 – Depressed Critical water level HYP 1 with buildings loads

- ***Inclinometer S21 – High Critical water level***

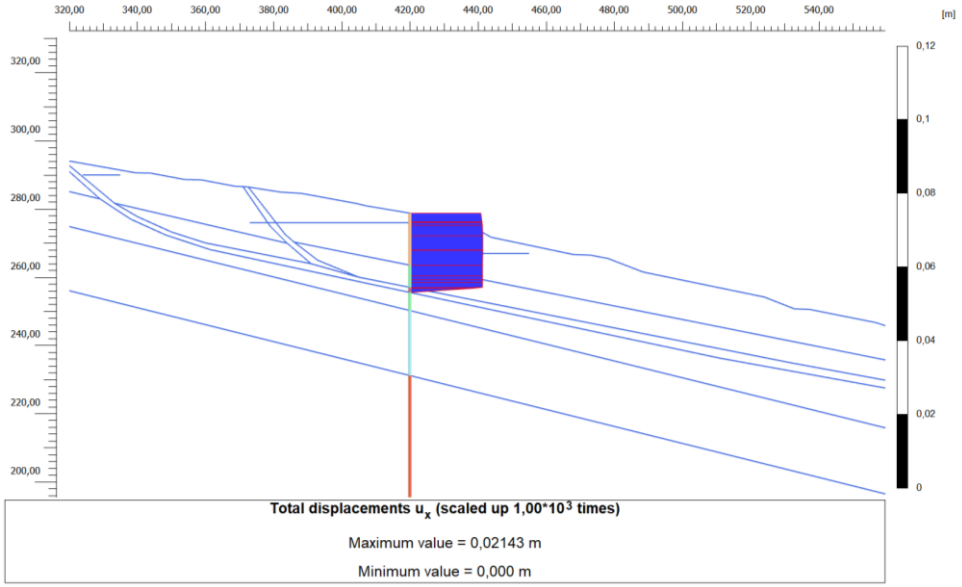

Figure 7.33: Horizontal displacements at the inclinometer S21 – High Critical water level HYP 1 with buildings loads

The displacements measured in the presence of buildings are as follows:

$S_{mod}^{S21\text{-}Nobuildings} = 2{,}96$ cm $\qquad S_{mod}^{S21\text{-}Buildings} = 35{,}23 \times 10^{-3}$ m $= 3{,}52$ cm

$S_{mod}^{S22\text{-}Nobuildings} = 0{,}73$ cm $\qquad S_{mod}^{S22\text{-}Buildings} = 8{,}57 \times 10^{-3}$ m $= 0{,}86$ cm

The results show that the difference between the displacements measured at the S21 and S22 inclinometers for the HYP 1 without buildings loads and HYP 1 with buildings loads is very small. Therefore, the subsequent analysis were carried out with the soil parameters of the HYP 1 and with the complete model that takes into account the building loads.

7.4 Level 4: FEM Model vs DInSAR data

After validating finite element modeling with inclinometric measurements, DInSAR data were compared with the results of numerical models. For this purpose, displacement indices "$I_{u,cosmo}$" and "$I_{u,mod}$" have been defined that have allowed analyzing the spatial distribution of both modelled and DInSAR-measured displacements (Figure 7.34). In particular, to define $I_{u,cosmo}$ from the COSMO DGV map the values of displacement along the longitudinal section A-A' have been derived.

$$I_{u,cosmo} = \frac{Ucosmo,i}{Ucosmo,max}$$

$$I_{u,mod} = \frac{Umod,i}{Umod,max}$$

With:

- $U_{cosmo,i}$ = cumulative Cosmo Sky-Med displacement measured within section A-A' with an interval of 2 metres (point i of the section);
- $U_{cosmo,max}$ = maximum cumulative Cosmo Sky-Med displacement along the section;
- $U_{mod,i}$ = cumulative modelled displacement with an interval of 2 metres (point i of the section);
- $U_{mod,max}$ = maximum cumulative modelled displacement along the section.

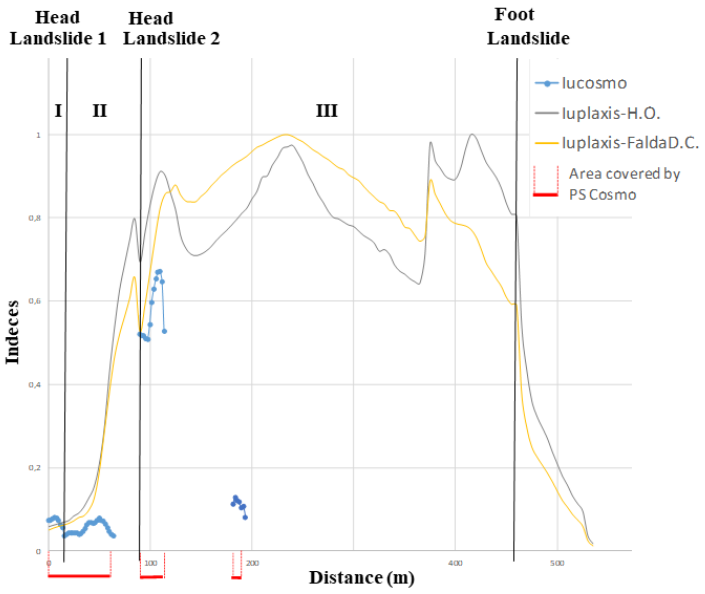

Figure 7.34: Displacement indices "Iu,cosmo" and "Iu,mod"

From the comparison, it seems that a good match is recorded in correspondence of the heads of the two landslide bodies where the two displacement indices (spatially) overlap (I and II interval). In the III interval the two displacement indices significantly differ due to a discontinuity in the spatial coverage of DInSAR data. These comparisons also made it possible to identify a satisfactory correspondence between the kinematics of the landslides phenomenon detected by the DInSAR data and that of the advanced numerical modelling. These comparisons allowed validating the modelling data and using the modelled displacement data in areas where there is no coverage of the satellite data (e.g. area downstream of the town of Lungro). Then, for the subsequent analysis, in which the vulnerability curves present in the literature and constructed with SAR monitoring data are used (Peduto et al. 2017, Nicodemo et al., 2019), the modelled settlements were used.

7.4.1 FEM Model vs Damage Level of buildings

The fourth phase of the analysis concerned the comparison of the damage severity level recorded on site to buildings with the displacements modelled with the FEM analysis. In the scientific literature there are several criteria for the assessment of building damage by means of different parameters to describe the foundation movement. The studies carried out used the international terminology defined by Burland (1995) according to the schemes shown in Figure 7.35.

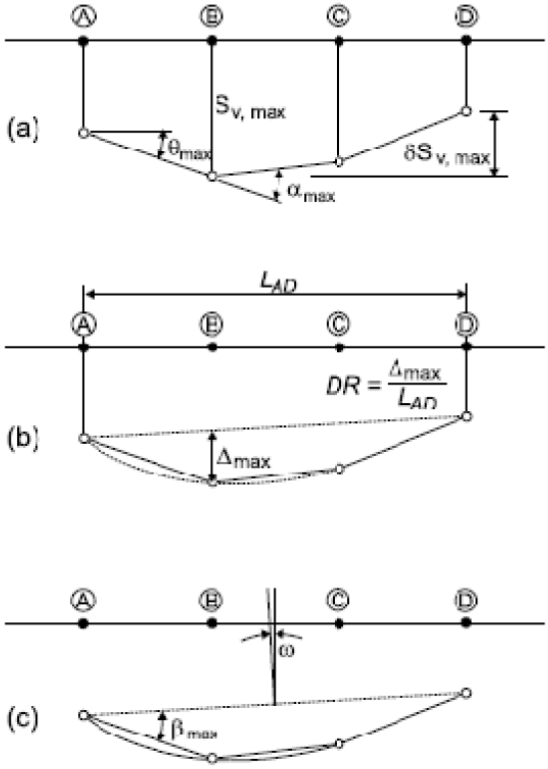

Figure 7.35: Definition of building deformation: a) settlement, differential settlement; b) relative deflection, deflection ratio; c) tilt, relative rotation (after Burland, 1995).

The following deformation parameters are defined:

- ***Settlement S_v***, defines the vertical movement of a point (positive values indicate downwards movement);
- ***Differential or relative settlement ΔS_v***, is the difference between two settlement values;
- ***Rotation or slope ϑ***, describes the change in gradient of the straight line defined by two reference points embedded in the structure;

In particular, the vertical movements (S_v) were obtained by measuring the values of the total settlements calculated by the FEM analyses at the initial and final points of buildings. Subsequently, the differential settlements and angular rotations were calculated for all buildings located on the A-A' and L-L' longitudinal sections (Figure 7.36). The analyses carried out have neglected the interaction of the building with the landslide phenomenon therefore the results pertaining to the modelled displacements turn out to be oversetimated.

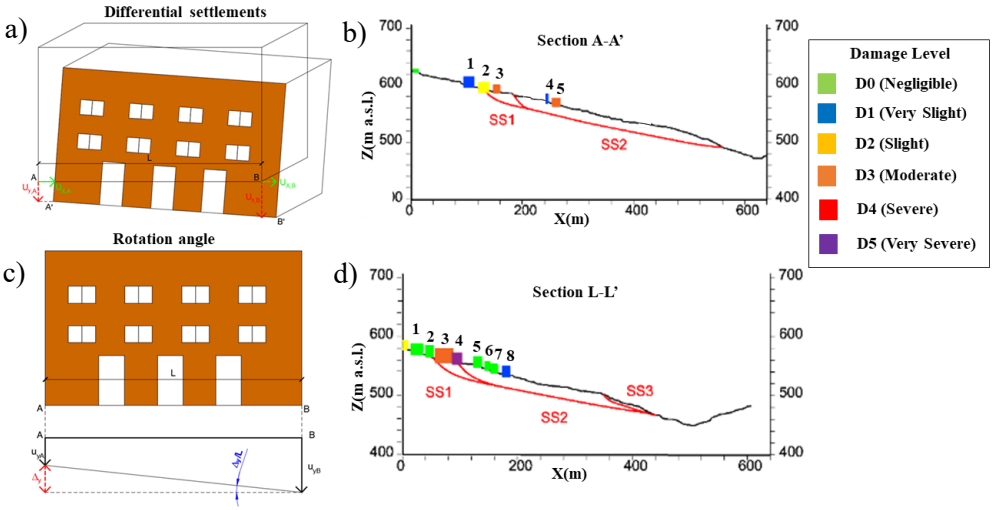

Figure 7.36: a) Differential settlements, b) longitudinal section A-A', c) rotation schematization, d)longitudinal section L-L'

The displacements calculated with the FEM modelling refer to a time interval of 5 years. Therefore, in order to compare the damage levels of the buildings with the results of FEM analysis the values displacements were amplified by a factor F that took into account the age of buildings (about 200 years) and defined as follows:

$$F = \frac{age\ of\ buildings}{5\ years}$$

$$\Delta_{tot} = S_{mod,PLAXIS} * F$$

With Δ_{tot} equal to the total settlements of buildings after 200 years.
In the tables 7.6 and 7.7 the total settlements and rotation angle of longitudinal sections A-A' and L-L' are shown.

Building number	**L[m]**	**Δ_x [mm]**	**Δ_x/L [°]**	**Δ_y [mm]**	**Δ_y/L [°]**
1	15	3,18	2,12E-04	7,50	5,00E-04
2	8	7,75	9,69E-04	61,89	7,74E-04
3	50	92,32	1,85E-03	27,20	5,44E-04
4	5	1,71	3,42E-04	5,01	1,00E-03
5	22	12,41	5,64E-04	25,72	1,17E-03

Table 7.6: The total settlements and rotation angle of longitudinal sections A-A'

Building number	**L[m]**	**Δ_x [mm]**	**Δ_x/L [°]**	**Δ_y [mm]**	**Δ_y/L [°]**
1	20	1,08	5,40E-05	7,17	3,58E-04
2	12	0,26	2,14E-05	2,78	2,32E-04
3	15	15,28	1,02E-03	14,21	9,47E-04
4	22	27,56	1,25E-03	23,28	1,06E-03
5	10	0,43	4,28E-05	1,28	1,28E-04
6	8	0,09	1,07E-05	0,34	4,28E-05
7	11	0,86	7,78E-05	2,05	1,87E-04
8	13	1,28	9,88E-05	4,28	3,29E-04

Table 7.7: The total settlements and rotation angle of longitudinal sections L-L'

The results obtained (Figure 7.37) show that generally higher differential settlements correspond to higher damage levels. The same results are also obtained for rotation angle.

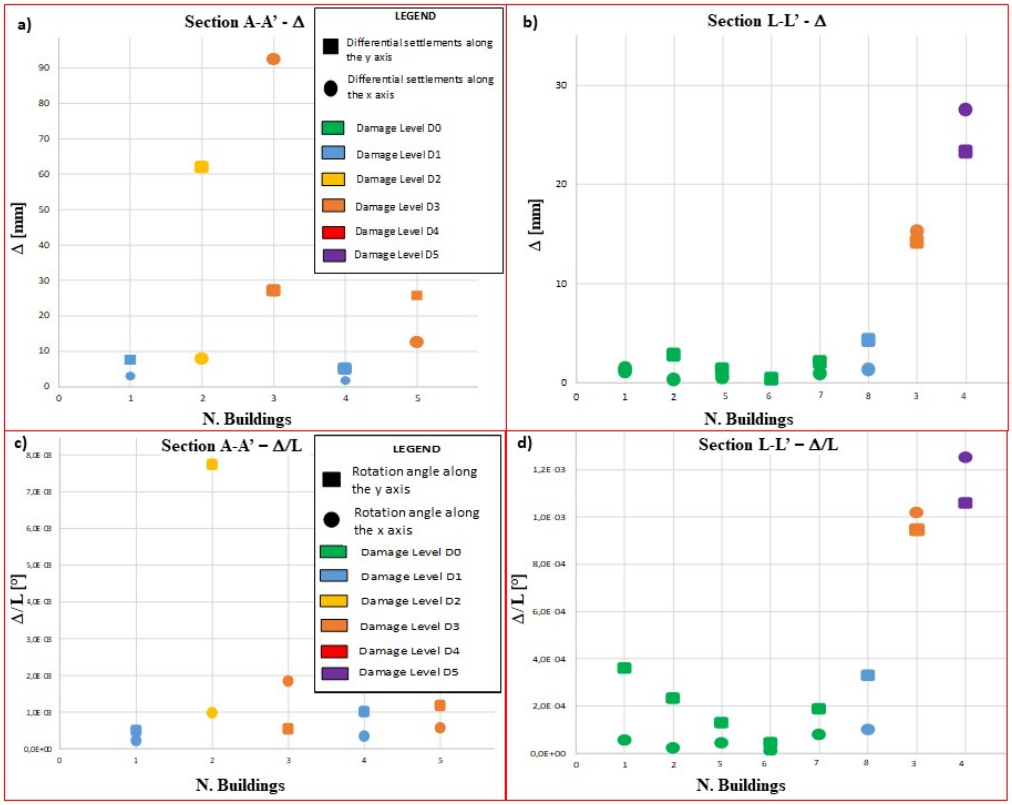

Figure 7.37: a)Damage severity VS differential settlements- Section A-A', b)Damage severity VS differential settlements- Section L-L', c) Damage severity VS rotation angle- Section A-A', d) Damage severity VS rotation angle- Section L-L'

However also from the comparison with the damage level, as well as for the comparisons with the DGV maps, some discordant resultants are present with those buildings located in correspondence of subservices. In fact, for buildings number 3 and 5 of the longitudinal section A-A' the differential settlements and rotation angle are low but the building exhibits a moderate damage level (D3). This anomaly may be related to the presence of any localized leakage of buried channels that have not been taken into account in the modelling but could result in an increase in settlement and, in turn, in the level of damage.

After checking the results of advanced modelling with the damage levels of buildings the vulnerability curve has been used (Figure 7.38). This curve, developed by previous studies for the urban area of Lungro (Peduto et al., 2017), allow reconstructing the historical path of buildings damage development and then to identify the time interval in which it reaches a moderate damage level (D3).

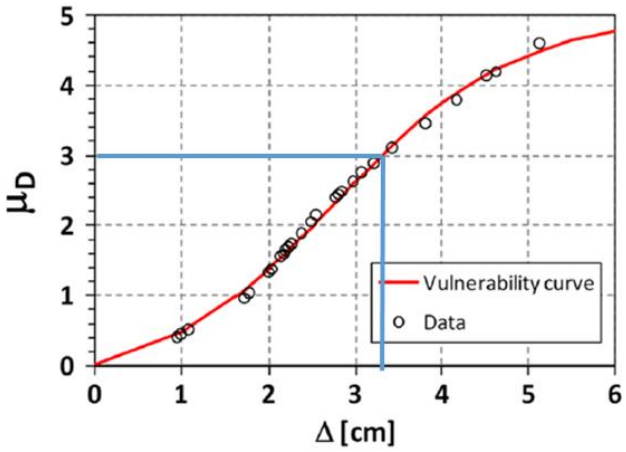

Figure 7.38: Empirical vulnerability curve with detection of displacement value corresponding to D3 damage level (modified from Peduto et al.,2017)

For example, with reference to the building n. 3 of section L-L' which has a total displacement Δ_{tot} of 1.5 cm and an annual displacement Δ_{yearly} of 0.035 cm, it is obtained that the building reaches a moderate damage (which corresponds to a displacement value of 3.2 cm) after 91 years. Instead for the building n.4 of the section L-L' which has a very severe damage (D5) the use of these curves could have avoided the achievement of the end of its life-cycle. Indeed, currently this building has been evacuated and has been shred because it is close to collapse (see Figure 7.39). But if these FEM analyses had been carried out already at the first signs of damage, it would have been obtained that the building, presenting a total displacement Δ_{tot} of 2.8 cm and an annual displacement Δ_{yearly} of 0.065 cm, already had a moderate level of damage (D3) after 49 years from the activation of the landslide.

Therefore, the use of this curve for buildings that currently have low damage level could be a valid tool to avoid the achievement of end of their life-cycle conditions through the implementation of appropriate reinforcement interventions. For example, considering the building n.1 of section A-A' with slight damage (D1) and a total displacement Δ_{tot} of 1.0 cm and an annual displacement Δ_{yearly} of 0.023 cm it can be forecasted that it reaches a displacement 3.2 cm and then a damage level D3 after 140 years. Therefore, the combined use of FEM modelling results and vulnerability curves may allow an adequate risk mitigation within the town of Lungro. To sum up, through advanced modelling it could be possible to compute the annual building displacement that compared with the displacement value of the different damage levels of the vulnerability curve allow identifying a period of time within which it is necessary to take action to prevent the loss of functionality or even the collapse of the building.

Figure 7.39: Structural interventions on building number 4 of section L-L' with damage level D5 (Peduto et al.,2017)

8. Discussion and Conclusions

This PhD Thesis was focused on the development of methodology aimed at kinematic characterization of slow-moving landslides in built-up areas.

The work first addressed: i) a literature review on the main features of the analyzed phenomena and their consequences in urban areas (Chapter 2); ii) the the principles and characteristics of conventional monitoring and remote sensing techniques that can be used for the study of slow-moving landslides. The monitoring techniques also include buildings damage surveys which can provide useful information for the characterisation of slow moving phenomenon (Chapter 3); iii) the description of the analysis methodology of slow moving landslides widespread in the scientific literature highlighting their potential and limitations (Chapter 4).

Then, based on this background and bearing in mind the main goal to be pursued, innovative methodology for the study of slow-moving landslides in urban areas was proposed (Chapter 5). In particular, focusing on the slow- moving landslide of the Lungro historic center (Chapter 6), the multi-source landslide characterization via the combination of conventional and remote sensing monitoring data, the synergistic analysis of kinematics and effects on the exposed structures and comparison of FEM modelling with innovative monitoring data were tested (Chapter 7).

The studies carried out have shown how the combined use of monitoring techniques (traditional and innovative) and numerical analysis (simplified or advanced) make it possible to derive the strength parameters of soil in the case of slow-moving landslides in urban areas where it is difficult to carry out

adequate tests on site and therefore to take high quality soil samples. In particular, with the integration of monitoring data, it was possible to define DGV maps that allow to reconstruct the spatial evolution of the landslide phenomenon. This information has proved to be a valid tool for studying the kinematics of landslides and analyzing the damage levels found on buildings. In addition, the combined use of the results of the LEM and FEM analysis, of the monitoring data and of the damage survey made it possible to calibrate the soil resistance parameters within the cutting bands without having to resort to laboratory tests. From the finite element analysis it was possible to define the total settlements that can be used for the use of fragility curves. In fact, knowing the total settlements from the results of the FEM analysis, it is possible to identify after how long a building reaches a moderate level of damage (D3) and therefore intervene before it reaches a collapse condition. Considering that most of the small villages in South Italy exhibit similar urban fabric and structural typology as the ones considered in this study, the applicability/exportability of the obtained results, although sitespecific, could be significant. In particular, using the proposed methodology developed for the study of the Lungro historical center landslide in similar geological contexts would allow a proper calibration and validation of this methodology for slow-moving landslides analysis. The use of this methodology would make it possible to understand after how long a building reaches a moderate level of damage (D3) and therefore to implement a census of buildings that require structural reinforcement to reduce the risk of collapse.

Applications

From the results obtained in the analyses carried out for the modelling of slow-moving landslides in the Lungro historical centre it is possible to deduce that modelled displacements could play as input data for a coupled geotechnical-structural analysis of buildings in landslide area. In particular, the following conclusions can be obtained:

- The in-depth knowledge on geomorphological features and geotechnical properties of involved soils, combined with multi-source (conventional and remote sensing) monitoring data and results of damage survey allows improving kinematic modelling of slow-moving landslides in urban areas;

- The proposed methodological approach could be valuably used for typifying other landslides in the same urban area and then for a sustainable management of slow-moving landslide risk at the urban scale;

- The use of the proposed methodology could be a valid tool for the census of buildings with a higher risk of collapse and for identifying the available times. In fact, with the use of settlements modelled with finite elements and vulnerability curves, it is possible to identify after how long a building reaches a moderate level of damage (D3) and then define the time frame within which it is necessary to carry out reinforcement interventions.

Further deepening and developments:

Future developments in the work carried out on the definition of a methodology for the analysis of slow-moving landslides should relate to the improvement of kinematic characterization. First of all, it is necessary to carry out finite element modelling which takes account of the viscous behaviour of soils, since the viscous component has been neglected in the studies carried out (Chapter 5). Moreover, in order to investigate the anomalies found on the severity of buildings damage respect to the kinematics of the landslide phenomenon it is necessary to model also the localized leakage of curried channels inside the historic center of Lungro which have been neglected in the following analyses (Chapter 7).
Moreover, studies carried out have made use of a two-dimensional FEM modelling, but in order to take into account possible three-dimensional effects within the landslide phenomenon it is necessary to carry out a three-dimensional modelling. Finally, it is worth mentioning the possibility of exporting the proposed methodology for slow-moving landslide analysis in urban area with similar geo-environmental contexts that are widespread in southern Italy. The use of this methodology in other similar landslides would allow to validate the approach used and to develop a methodology that would allow to calibrate the soil resistance parameters with the combined use of inclinometric data and satellite monitoring data.

REFERENCES

Abolmasov B., Milenković S., Marjanović M., Đurić U. & Jelisavac, B. (2015). A geotechnical model of the Umka landslide with reference to landslides in weathered Neogene marls in Serbia. Landslides, 12(4), 689-702.

Agostini A., Tofani V., Nolesini T., Gigli G., Tanteri L., Rosi A., Cardellini S, Casagli N. (2013). A new appraisal of the Ancona landslide based on geotechnical investigations and stability modelling. Quarterly Journal of Engineering Geology and Hydrogeology, 1- 10, ISSN:1470-9236.

Alexander D., (1986). Landslide damage to buildings. Environmental Geology and Water Science, 8: 147-151.

Angeli M.G., Gasparetto P., Pasuto A. and Silvano S. (1989). Examples of landslides instrumentation (Italy). Proceesings of the 12th International Conference on Soil Mechanics and Foundation Engineering, Rio de Janiero, Vol. 3, pp. 1531-1534.

Antronico L., Borrelli L., Peduto D., Fornaro G., Gullà G., Paglia L., Zeni G. (2013). Conventional and innovative techniques for the monitoring of displacements in landslide affected area. In: Margottini C., Canuti P, Sassa K (Eds.) Landslide science and practice – Early warning, instrumentation and monitoring. Springer-Verlag, – Vol. 2, pp. 125-131.

Antronico L., Borrelli L., Coscarelli R., Gullà G. (2014). Time evolution of landslide damages to buildings: the case study of Lungro (Calabria, southern Italy). Bulletin of Engineering Geology and the Environment, 74:47-59.

Antronico L, Petrucci O, Sorriso-Valvo M (1996) I fenomeni franosi nella tavoletta “Montalto Uffugo” (CS) risultati inattesi dall’analisi delle relazioni tra morfometria e tipologia delle frane e litologia dei versanti. Geol Appl Idrogeol 31(4):187–201.

Antronico L., Borrelli L., Coscarelli R. & Gullà, G. (2015). Time evolution of landslide damages to buildings: the case study of Lungro (Calabria, southern Italy). Bulletin of Engineering Geology and the Environment, 74(1), 47-59.

Audell H.S., (1996). Geotechnical nomenclature and classification system for crack patterns in buildings. Environmental and Engineering Geoscience, 2:225-248.

Bhattacharya, S., & Singh, M. M. (1985). Development of subsidence damage criteria. Final report (No. PB-90-147356/XAB). Engineers International, Inc., Westmont, IL (USA).

Berardino P., Fornaro G., Lanari R., Sansosti E. (2002). A new algorithm for surface deformation monitoring based on small baseline differential SAR interferograms. IEEE Transactions Geoscience Remote Sensing, 40 (11):2375–2383.

Berardino P., Costantini M, Franceschetti G., Iodice A, Pietranera, L, Rizzo V. (2003). Use of differential SAR interferometry in monitoring and modelling large slope instability at Maratea (Basilicata,Italy). Engineering Geology, 68:31-51.

Bianchini S, Cigna F, Righini G, Proietti C, Casagli N (2012) Landslide hotspot mapping by means of persistent scatterer interferometry. Environ Earth Sci 67:1155–1172.

Bonachea J., Remondo J., De Terán J. R. D., González-Díez A., & Cendrero A. (2009). Landslide risk models for decision making. Risk Analysis: An International Journal, 29(11), 1629-1643.

Borrelli L., Nicodemo G., Ferlisi S., Peduto D., Di Nocera S., & Gullà G. (2018). Geology, slow-moving landslides, and damages to buildings in the Verbicaro area (north-western Calabria region, southern Italy). Journal of Maps, 14(2), 32-44.

Bovenga, F., Wasowski, J., Nitti, D. O., Nutricato, R., & Chiaradia, M. T. (2012). Using COSMO/SkyMed X-band and ENVISAT C-band SAR interferometry for landslides analysis. Remote Sensing of Environment, 119(C), 272–285. http://dx.doi.org/10.1016/j.rse.2011.12.013

Brabb, E. E., & Harrod, B.L. (Eds.). (1989). Landslides: Extent and economic significance. Rotterdam: A.A. Balkema Publisher (385 pp.).

Bru, G., Fernández-Merodo, J. A., García-Davalillo, J. C., Herrera, G., & Fernández, J. (2018). Site scale modeling of slow-moving landslides, a 3D viscoplastic finite element modeling approach. Landslides, 15(2), 257-272.

Buckle P., Mars G., & Smale S. (2000). New approaches to assessing vulnerability and resilience. Australian Journal of Emergency Management, The, 15(2), 8-14.

Burland J.B., Broms B.B., De Mello V.F.B. (1977). Behaviour of foundations and structures. Proceedings of 9th International Conference SMFE – Vol 2. Tokyo. pp. 495-546.

Burland J. B., (1995). Assessment of risk of damage to buildings due to tunnelling and excavation. Invited Special Lecture, 1st International Conference on Earthquake Geotechnical Engineering, IS.Tokyo '95.

Canuti P., Casagli N., Farina P., Ferretti A., Marks F., Menduni G.(2006). Analisi dei fenomeni di subsidenza nel bacino del fiume Arno mediante interferometria radar. Giornale di Geologia Applicata, 4:131- 136, doi: 10.1474/GGA.2006-04.0-17.0145.

Calò F., Ardizzone F., Castaldo R., Lollino P., Tizzani P., Guzzetti F., Lanari R., Angeli M.G., Pontoni F., Manunta M. (2014), Enhanced landslide investigations through advanced DInSAR techniques: The Ivancich case study, Assisi, Italy. Remote Sensing of Environment, 142 (2014) 69–82.

Calvello, M., Peduto, D., & Arena, L. (2017). Combined use of statistical and DInSAR data analyses to define the state of activity of slow-moving landslides. Landslides, 14(2), 473-489.

Cascini L., Gullà G. (1992a). Analisi di dettaglio delle caratteristiche fisico meccaniche dei terreni prodotti dall'alterazione degli gneiss di S. Pietro in Guarano (CS). Geologia Applicata e Idrogeologia, Vol. XXVII, pp. 49-76, (in Italian).

Cascini L, Peduto D, Pisciotta G, Arena L, Ferlisi S, Fornaro G (2013) The combination of DInSAR and facility damage data for the updating of slow-moving landslide inventory maps at medium scale. Nat Hazards Earth Syst Sci 13(6):1527.

Cascini, L. (1986). Movimenti discontinui di una coltre di detrito della Sila Grande. Proceedings, 16th Convegno Nazionale di Geotecnica, Bologna, Italy, 1, 259-262.

Cascini L., Gullà G. (1992a). Analisi di dettaglio delle caratteristiche fisico meccaniche dei terreni prodotti dall'alterazione degli gneiss di S. Pietro in Guarano (CS). Geologia Applicata e Idrogeologia, Vol. XXVII, pp. 49-76, (in Italian).

Cascini l., Gullà G. (1992b). Grado di alterazione e maccanismi di rottura nei terreni prodotti dall'alterazione degli gneiss di S. Pietro in Guarano (CS). Risultati preliminari. CNR-IRPI, Rapporto interno, N.363; (in Italian).

Cascini, L., Fornaro, G., & Peduto D. (2009). Analysis at medium scale of low-resolution DInSAR data in slow-moving landslide-affected areas. ISPRS Journal of Photogrammetry and Remote Sensing, 64, 598–611. http://dx.doi.org/10.1016/j.isprsjprs.2009.05.003.

Cascini L., Fornaro G. & Peduto D. (2010). Advanced low- and full-resolution DInSAR map generation for slow-moving landslide analysis at different scales. Engineering Geology, 112(1–4), 29–42. http://dx.doi.org/10.1016/j.enggeo.2010.01.003.

Cascini L., Gullà G., Sorbino G. (2006). Groundwater modelling of a weathered gneissic cover. Can Geotech J 43:1153–1166.

Cascini L., Ferlisi S., Fornaro G., Lanari R., Peduto D., Zeni G. (2006). Subsidence monitoring in Sarno urban area via multitemporal DInSAR technique. International Journal of Remote Sensing, 27:1709– 1716.

Cascini, L. C. J. R. J. O., Bonnard, C., Corominas, J., Jibson, R., & Montero-Olarte, J. (2005). Landslide hazard and risk zoning for urban planning and development. In Landslide risk management (pp. 209-246). CRC Press.

Cascini L., Peduto D., Pisciotta G., Arena L., Ferlisi S., Fornaro G. (2013). The combination of DInSAR and facility damage data for the updating of slow-moving landslide inventory maps at medium scale. Nat Hazards Earth Syst Sci 13(6):1527.

Cascini, L., Ferlisi, S., Peduto, D., Fornaro, G., & Manunta, M. (2007). Analysis of a subsidence phenomenon via DInSAR data and geotechnical criteria. Italian Geotechnical Journal, 41(4), 50-67.

Cascini L., Fornaro G. and Peduto, D.(2010a). Advanced low- and full resolution DInSAR map generation for slow-moving landslide analysis at different scales. Engineering Geology, 112:29–42.

Castaldo R, Tizzani P, Calò F, Ardizzone F, Lanari R, Guzzetti F, Manunta M (2015) Landslide kinematical analysis through inverse numerical modelling and differential SAR interferometry. Pure Appl Geophys 172:3067–3080. https://doi.org/10.1007/ s00024-014-1008-3.

Catani F., Casagli N., Ermini L., Righini G. and Menduni G. (2005). Landslide hazard and risk mapping at catchment scale 2005 Arno River basin. Landslides, 2:329–342.

Chiocchio C., Iovine G., Parise M., (1997). A proposal for surveying and classifying landslide damage to buildings. In: Marinos, P.G., Koukis, G.C., Tsiambaos, G.C. & Stournaras G.C. (eds) Engineering Geology and the Environment, Proceedings of the IAEG International symposium on engineering geology and the environment, Athens, June, 1997. Balkema - Rotterdam, pp. 553-558.

Ciampalini A, Bardi F, Bianchini S, Frodella W, Del Ventisette C, Moretti S, Casagli N (2014) Analysis of building deformation in landslide area using multisensor PSInSAR™ technique. Int J Appl Earth Obs Geoinf 33:166–180.

Colesanti C., Ferretti A., Novali F., Prati C., Rocca F. (2003). SAR monitoring of progressive and seasonal round deformation using the permanent scatterers technique. IEEE Transactions on Geoscience and Remote Sensing, 41:1685–1701.

Colesanti C, Wasowski J (2006) Investigating landslides with space-borne Synthetic Aperture Radar (SAR) interferometry. Eng Geol 88(3-4):173–199.

Comegna L., Picarelli L., Bucchignani E., & Mercogliano P. (2013). Potential effects of incoming climate changes on the behaviour of slow active landslides in clay. Landslides, 10(4), 373-391.

Conte E., Pugliese L., & Troncone A. (2020). Post-failure analysis of the Maierato landslide using the material point method. Engineering Geology, 277, 105788.

Costantini M., Falco S., Malvarosa F., Minati F. (2008). A new method for identification and analysis of persistent scatterers in series of SAR images. In: IEEE International Geoscience & Remote Sensing Symposium, July 6–11, 2008, Boston, Massachusetts, USA, pp. 449–452.

Cotecchia F. (1989). Studio di un movimento franoso nelle Unità Irpine dell'alta valle dell'Ofanto. Italian Geotechnical Journal, 2:57-84, (in Italian).

Cotecchia, V. (2006). The Second Hans Cloos Lecture. Experience drawn from the great Ancona landslide of 1982. Bulletin of Engineering Geology and the Environment, 65:1–41.

Cotecchia F., Vitone C., Santaloia F., Pedone G. & Bottiglieri O. (2015). Slope instability processes in intensely fissured clays: case histories in the Southern Apennines. Landslides, 12(5), 877-893.

Cotecchia, F., Ferlisi, S., Santaloia, F., Vitone, C., Lollino, P., Pedone, G., & Bottiglieri, O. (2014). La diagnosi del meccanismo di frana nell'analisi del rischio'. Panel lecture, XXV Convegno Nazionale di Geotecnica,'La geotecnica nella difesa del territorio e delle infrastrutture dalle calamitanaturali', Baveno, 167-186.

Crosetto, M., Monserrat, O., Cuevas-González, M., Devanthéry, N., Luzi, G., & Crippa, B. (2015). Measuring thermal expansion using X-band persistent scatterer interferometry. ISPRS journal of photogrammetry and remote sensing, 100, 84-91.

Crosetto M., Biescas E., Duro J. (2008). Generation of advanced ERS and Envisat interferometric SAR products using the stable point network technique. Photogrammetric Engineering & Remote Sensing, 4:443–450.

Cruden D.M., Varnes D.J. (1996). Landslide types and processes. Landslides: investigation and mitigation. Transportation Research Board, Special Report, No. 247, National Research Council, National Academy Press, Washington DC, USA 36-75.

De Novellis, V., Castaldo, R., Lollino, P., Manunta, M., & Tizzani, P. (2016). Advanced three-dimensional finite element modeling of a slow landslide through the exploitation of DInSAR measurements and in situ surveys. Remote Sensing, 8(8), 670.

Del Soldato M, Solari L, Poggi F, Raspini F, Tomás R, Fanti R, Casagli N (2019) Landslideinduced damage probability estimation coupling InSAR and field survey data by fragility curves. Remote Sens 11:1486. https://doi.org/10.3390/rs11121486.

Di Maio C., Fornaro G., Gioia D., Reale D., Schiattarella M. and Vassallo R. (2018). In situ and satellite long-term monitoring of the Latronico landslide, Italy: displacement evolution, damage to buildings, and effectiveness of remedial works. Engineering Geology 245 (2018) 218-235.

Duncan, J. M. (1996). Landslides: investigation and mitigation. Chapter 13-Soil slope stability analysis. Transportation Research Board Special Report, (247).

Duncan, J. M., & Wright, S. G. (1980). The accuracy of equilibrium methods of slope stability analysis. Engineering geology, 16(1-2), 5-17.

Fell R., Hartford D., (1997). Landslide risk management. In: Cruden C, Fell R (eds), Landslide risk assessment. Proceedings of the international workshop on landslide risk assessment, Honolulu. A. A. Balkema, Rotterdam, pp. 51–109.

Fell R., Corominas J., Bonnard C., Cascini L., Leroi E. & Savage, W. Z. (2008). Guidelines for landslide susceptibility, hazard and risk zoning for land-use planning. Engineering geology, 102(3-4), 99-111.

Forte G., Pirone M., Santo A., Nicotera M. V. & Urciuoli, G. (2019). Triggering and predisposing factors for flow-like landslides in pyroclastic soils: the case study of the Lattari Mts. (southern Italy). Engineering Geology, 257, 105137.

Ferlisi, S., Gullà, G., Nicodemo, G., & Peduto, D. (2019). A multi-scale methodological approach for slow-moving landslide risk mitigation in urban areas, southern Italy. Euro-Mediterranean Journal for Environmental Integration, 4(1), 1-15.

Ferlisi, S., Marchese, A., & Peduto, D. (2021). Quantitative analysis of the risk to road networks exposed to slow-moving landslides: a case study in the Campania region (southern Italy). Landslides, 18(1), 303-319.

Ferlisi S., Peduto D., Gullà G., Nicodemo G., Borrelli L., Fornaro G. (2015). The use of DInSAR data for the analysis of building damage induced by slow-moving landslides. In: Lollino G, Giordan D, Crosta GB, J. Corominas J, Azzam R, Wasowski J, Sciarra N (Eds.), Engineering Geology for Society and Territory – Landslide Processes, © Springer International Publishing – Vol. 2, pp. 1835-1839. doi: 10.1007/978- 3-319-09057-3_325.

Ferretti A., Prati C., Rocca F. (2000). Nonlinear subsidence rate estimation using permanent scatterers in differential SAR interferometry. IEEE Transactions on Geoscience and Remote Sensing, 38 (5):2202–2212.

Ferretti A., Prati C., Rocca F. (2001). Permanent scatterers in SAR interferometry. IEEE Transactions on Geoscience and Remote Sensing, 39 (1):8–20.

Fornaro G., Reale D., Serafino F. (2009). Four-dimensional SAR imaging for height estimation and monitoring of single and double scatterers. IEEE Transactions on Geoscience and Remote Sensing., 47 (1): 212–237.

Fornaro G. and Pascazio V. (2014a). SAR Interferometry and Tomography: Theory and Applications. In: Chellapa, R., Theodoridis, S. (Eds.), Academic Press Library in Signal Processing, Vol. 2, Communications and Radar Signal Processing Chennai. New York, USA: Academic, 1034–1117.

Fornaro G., Lombardini F., Pauciullo A., Reale D., Viviani F. (2014b). Tomographic Processing of Interferometric SAR Data: Developments, applications, and future research perspectives. IEEE Signal Processing Magazine, 31(4): 41-50.

Franceschetti G. and Fornaro G. (1999). Synthetic aperture radar interferometry. In: G. Franceschetti and R. Lanari (Eds.), Synthetic Aperture Radar Processing, CRC Press. Boca Raton, FL: 167-223.

Frattini P, Crosta GB, Rossini M, Allievi J (2018) Activity and kinematic behaviour of deepseated landslides from PS-InSAR displacement rate measurements. Landslides 15(6):1053–1070.

Fredlund D. G., & Krahn J. (1977). Comparison of slope stability methods of analysis. Canadian geotechnical journal, 14(3), 429-439.

Freeman T.J., Littlejohn G.S., Driscoll R.M.C., (1994). Has your house got cracks: a guide to subsidence and heave of buildings on clay. Institution of Civil Engineers and Building Research Establishment, pp. 114.

Fruneau B., Achache J., Delacourt C. (1996). Observation and Modeling of the Saint-Etienne-de-Tinée Landslide Using SAR Interferometry. Tectonophysics, 265:181–190.

Fruneau B., Carnec C., Colesanti C., Deffontaines B., Ferretti A., Mouelic S., Le Parmentier A.M., Rudant J.P. (2003). Conventional and PS differential SAR interferometry for monitoring vertical deformation due to water pumping. The Haussmann-St-Lazare case example (Paris, France). Proc. FRINGE 2003, 1-5 December, Frascati (Italy).

Gens A., & Alonso E. E. (2006). Aznalcóllar dam failure. Part 2: Stability conditions and failure mechanism. Géotechnique, 56(3), 185-201.

García-Davalillo, J. C., Herrera, G., Notti, D., Hernández-Ruiz, M., Fernández-Merodo, J. A., Álvarez-Fernández, I., ... & Mora, O. (2013). InSAR Data for Mapping and Monitoring Landslides in Tena Valley. In Landslide Science and Practice (pp. 243-249). Springer, Berlin, Heidelberg.

Giordano D., Allasia P., Manconi A., Baldo M., Santangelo M., Cardinali M., et al. (2013). Morphological and kinematic evolution of a large earthflow: The Montaguto landslide, southern Italy. Geomorphology, 187, 61–79. http://dx.doi.org/10.1016/j. geomorph.2012.12.035.

Griffiths, D. V., & Lane, P. A. (1999). Slope stability analysis by finite elements. Geotechnique, 49(3), 387-403.

Greco R, Sorriso-Valvo M, Catalano E (2007) Logistic regression analysis in mass movement susceptibility: the Aspromonte case study, Calabria, Italy. Eng Geol 89(1–12):47–66.

Griffiths, J. S., Mather, A. E., & Hart, A. B. (2002). Landslide susceptibility in the Rio Aguas catchment, SE Spain. Quarterly Journal of Engineering Geology and Hydrogeology, 35(1), 9-17.

Griffiths, D. V., & Marquez, R. M. (2007). Three-dimensional slope stability analysis by elasto-plastic finite elements. Geotechnique, 57(6), 537-546.

Guerricchio A, Doglioni A, Simeone V (2012) Tectonic-gravitational deep-seated failures and macro-landslides in Scilla and Punta Pezzo area (Southern Calabria - Italy). Rend Online Soc Geol Ital 21(1):367–369

Gullà G., Borrelli L., & Greco R. (2004). Weathering of rock-mass as possible characterizing factor of predisposition to slope instabilities. In Proceedings of the IX international symposium on landslides, Rio de Janeiro (pp. 103-108).

Gullà G., Fornaro G., Borrelli L., Antronico L., Reale D., & Verde S. (2014). Integrazione progressiva di dati geotecnici e da satellite nell'analisi del rischio da frana in area urbana: il quartiere di Ianò - Catanzaro. Atti del XXV Convegno Nazionale di Geotecnica, Vol. 2 – La Gestione nella difesa del Territorio e delle Infrastrutture dalle Calamità Naturali. Baveno, Italia, 4-6 giugno 2014, pp. 571-578 (in Italian).

Gullà G., Peduto D., Borrelli L., Antronico L., Fornaro G. (2016). Geometric and kinematic characterization of landslides affecting urban areas: the Lungro case study (Calabria, southern Italy). Landslides, 14(1):171-188, DOI: 10.1007/s10346-015-0676-0.

Gullà, G. and Aceto L. (2009). Geotechnical characterization of the geomaterials present in the town of Lungro and its vicinity. CNR-IRPI, Internal Report no. 782, April 2009.

Gulla, G., Aceto, L., Antronico, L., Borrelli, L., Coscarelli, R., & Perri, F. (2018). A smart geotechnical model in emergency conditions: A case study of a medium-deep landslide in Southern Italy. Engineering Geology, 234, 138-152.

Gullà G., Ferlisi S., Nicodemo G., Peduto D. (2017). Un approccio metodologico per la gestione del rischio in aree urbane affette da frane a cinematica lenta. Submitted to XXVI – CNG Convegno Nazionale di Geotecnica – Roma 2017, (in Italian).

Gullà, G., Peduto, D., Borrelli, L., Antronico, L., & Fornaro, G. (2017). Geometric and kinematic characterization of landslides affecting urban areas: the Lungro case study (Calabria, Southern Italy). Landslides, 14(1), 171-188.

Guzzetti, F., Reichenbach, P., Cardinali, M., Galli, M., & Ardizzone, F. (2005). Probabilistic landslide hazard assessment at the basin scale. Geomorphology, 72(1-4), 272–299. http://dx.doi.org/10.1016/j.geomorph.2005.06.002.

Guzzetti F., Manunta M., Ardizzone F., Pepe A., Cardinali M., Zeni G., et al. (2009). Analysis of ground deformation detected using the SBAS-DInSAR technique in Umbria, Central Italy. Pure and Applied Geophysics, 166, 1425–1459. http://dx.doi.org/10. 1007/s00024-009-0491-4.

Guzzetti, F. (2000). Landslide fatalities and the evaluation of landslide risk in Italy. Engineering Geology, 58(2), 89-107.

Guzzetti F., Mondini A. C., Cardinali M., Fiorucci F., Santangelo M. & Chang, K. T. (2012). Landslide inventory maps: New tools for an old problem. Earth-Science Reviews, 112(1-2), 42-66.

Guzzetti, F., Peruccacci, S., Rossi, M., & Stark, C. P. (2007). Rainfall thresholds for the initiation of landslides in central and southern Europe. Meteorology and atmospheric physics, 98(3), 239-267.

Grünthal, G. (1998). European macroseismic scale 1998. European Seismological Commission (ESC).

Hanssen RF (2001) Radar Interferometry: Data Interpretation and Error Analysis, vol 2. Springer-Verlag, Berlin.

Herrera G., Notti D., Garcia-Davalillo J.C., Mora O., Cooksley G., Sanchez M., Arnaud A., Crosetto M. (2011). Analysis with C- and Xband satellite SAR data of the Portalet landslide area. Landslides, (8):195–206.

Herrera G, Gutiérrez F, García-Davalillo JC, Guerrero J, Notti D, Galve JP, Fernàndez- Merodo JA, Cooksley G (2013) Multi-sensor advanced DInSAR monitoring of very slow landslides: the Tena Valley case study (Central Spanish Pyrenees). Remote Sens Environ 128:31–43.

Henderson F. M and Lewis A. J. (1998). Principles and Applications of Imaging Radar. Manual of Remote Sensing, Vol. 2, New York: J. Wiley.

Howard Humphreys and Partners, (1993). Subsidence in Norwich. London, HMSO, pp. 99.

Hungr O., Leroueil S., Picarelli L. (2012). The Varnes classification of landslide types, an update. Landslides, 11:167:194.

Hilley, G., Bürgmann, R., Ferretti, A., Novali, F., & Rocca, F. (2004). Dynamics of slow-moving landslides from permanent scatterer analysis. Science, 304, 1952–1955. http://dx.doi.org/10.1126/science.1098821.

Iannace A, Bonardi G, D'Errico M, Mazzoli S, Perrone V, Vitale S (2005) Structural setting and tectonic evolution of the Apennine Units of northern Calabria. Compt Rendus Geosci 337(16):1541–1550.

Infante D, Di Martire D, Confuorto P, Tessitore S, Ramondini M, Calcaterra D (2018). Differential SAR interferometry technique for control of linear infrastructures affected by ground instability phenomena. International Archives of the Photogrammetry, Remote Sensing and Spatial Information Sciences, 42(3/W4).

Iovine G., Petrucci O., Rizzo V., Tansi C. (2006). The March 7th 2005 Cavallerizzo (Cerzeto) landslide in Calabria – Southern Italy. Proceedings of the 10th IAEG Congress, Nottingham, Great Britain, 6– 10 September 2006, 785, 1–12.

Jaboyedoff M., Oppikofer T., Abellán A., Derron M. H., Loye A., Metzger R., & Pedrazzini A. (2012). Use of LIDAR in landslide investigations: a review. Natural hazards, 61(1), 5-28.

Jaboyedoff M., Del Gaudio V., Derron M.H., Grandjean G., Jongmans D. (2019). Characterizing and monitoring landslide processes using remote sensing and geophysics. Eng Geol 259:105167.

Johnson R., (2005). Significance of cracks in low-rise buildings – what you need to know. Civil Engineering, Paper 13014, 158:30-35.

Kimura H., and Yamaguchi Y. (2000). Detection of landslide areas using satellite radar interferometry. Photogrammetric Engineering & Remote Sensing, 66(3):337–344.

Leone, F., Asté, J. P., & Leroi, E. (1996). Vulnerability assessment of elements exposed to mass-movement: working toward a better risk perception. Landslides-Glissements de Terrain. Balkema, Rotterdam, 263-270.

Leroueil S., Locat J., Vaunat J., Picarelli L., Lee H., Faure R. (1996). Geotechnical characterization of slope movements. Proceedings 7th International Symposium Land-slides, Trondheim, Norway 1:53-74.

Lillesand, T.M. and Kiefer, R.W. (1987). Remote Sensing and Image Interpretation. Sec. Ed., John Wiley and Sons, Inc., Toronto.

Lollino G., Baldo M., Giordan D., & Godone F. (2005). Utilizzo integrato di misure GPS in continuo e rilievi laser scanner per il controllo del fenomeno di crollo di Le Ayas (Bardonecchia–Torino). ASITA, 2, 1357-1362.

Lollino, G., Pasculli, A., Sciarra, N., Baldo, M., & Giordan, D. (2007). An integrated methodology based on LIDAR, GPS and photogrammetric surveys applied to large landslide in San Martino sulla Marrucina (Central Italy). In Proceedings of First North American Landslide Conference (Vol. 23, pp. 356-365). AEG Special Publication Vail Colorado.

Lollino, G., Arattano, M., Giardino, M., Oliveira, R., & Peppoloni, S. (Eds.). (2014). Engineering Geology for Society and Territory-Volume 7: Education, Professional Ethics and Public Recognition of Engineering Geology (Vol. 7). Springer.

Lollino, P., Elia, G., Cotecchia, F., & Mitaritonna, G. (2010). Analysis of landslide reactivation mechanisms in Daunia clay slopes by means of limit equilibrium and FEM methods. In GeoFlorida 2010: Advances in analysis, modeling & design (pp. 3155-3164).

Lu P., Casagli N., Catani F., Tofani, V. (2012). Persistent Scatterers Interferometry Hotspot and Cluster Analysis (PSI-HCA) for detection of extremely slow-moving landslides. International Journal of Remote Sensing, 33:466–489.

Macrì, E. (2020). Cultural Commons and Historical Identity: The Experience of the Arbëreshë Community in Southern Italy. In Cultural Commons and Urban Dynamics (pp. 205-220). Springer, Cham.

Madsen S.N., Zebker H.A., Martin J. (1993). Topographic Mapping Using Radar Interferometry: Processing Techniques. IEEE Transactions on Geoscience and Remote Sensing, 31(1):246-256.

Manzo M., Ricciardi G.P., Casu F., Ventura G., Zeni G., Borgstrom S., Berardino P., Del Gaudio C., Lanari R. (2006). Surface deformation analysis in the Ischia Island (Italy) based on spaceborne radar interferometry. Journal of Volcanology and Geothermal Research, 151(4):399–416.

Meisina C., Zucca F., Notti D, Colombo A., Cucchi A., Savio G., Giannico C. and Bianchi M.(2008). Geological Interpretation of PSInSAR Data at Regional Scale. Sensors 2008, 8:7469-7492; DOI: 10.3390/s8117469.

Merodo JAF, Davalillo JCG, Herrera G, Mira P, Pastor M (2014) 2D viscoplastic finite element modelling of slow landslides: the Portalet case study (Spain). Landslides 11:29–42.

Milone G., Scepi G. (2011). A clustering approach for studying ground deformation trends in Campania Region through PS-InSAR time series analysis. Journal of Applied Sciences, 2011 ISSN 1812/ DOI: 10. 3923/jas.

Mora O., Mallorquı J.J., Broquetas A. (2003). Linear and nonlinear terrain deformation maps from a reduced set of interferometric SAR images. IEEE Transactions on Geoscience and Remote Sensing, 41:2243–2253.

Moreira M., Prats-Iraola P., Younis M., Krieger G., Hajnsek I., Papathanass K. P. (2013). A Tutorial on Synthetic Aperture Radar. IEEE Geoscience and remote sensing magazine, pp 6-43, doi 10.1109/MGRS.2013.2248301.

Morgenstern, N. R. (2018). Toward landslide risk assessment in practice. In Landslide risk assessment (pp. 15-23). Routledge.

Nappo N, Peduto D, Mavrouli O, van Westen CJ, Gullà G (2019) Eng Geol 260 (2019), https://doi.org/10.1016/j.enggeo.2019.105244. National Coal Board, (1975). Subsidence Engineers Handbook. National Coal Board Production Dept., U.K.

Nicodemo G., Peduto D., Ferlisi S., Maccabiani J. (2016). Investigating building settlements via very high resolution SAR sensors. In: Bakker, J., Frangopol, D.M., van Breugel, K. (Eds.), Life-Cycle of Engineering Systems: Emphasis on Sustainable Civil Infrastructure. Proceedings of the Fifth International Symposium on Life-Cycle Civil Engineering (IALCCE 2016), 16–19 October 2016, Delft, The Netherlands. Taylor & Francis Group, London, pp. 2256–2263, (ISBN 978-1-138-02847-0).

Nicodemo, G. (2017). Vulnerability analysis of buildings in areas affected by slow-moving landslides and subsidence phenomena.

Nicodemo G, Ferlisi S, Peduto D, Aceto L, Gullà G (2020). Damage to masonry buildings interacting with slow-moving landslides: a numerical analysis, Lecture Notes in Civil Engineering, F. Calvetti et al. (Eds.): CNRIG 2019, LNCE 40, pp. 52–61, 2020, © Springer Nature Switzerland AG 2020, https://doi.org/10.1007/978-3-030-21359-6_6.

Nicodemo G., Peduto D., Ferlisi S., Gullà G., Borrelli L., Fornaro G., Reale D. (2017a). Analysis of building vulnerability to slow-moving landslides via A-DInSAR and damage survey data. In M. Mikos et al. (eds.), Advancing Culture of Living with Landslides, Proc. Of 4th World Landslide Forum, Ljubljana, 30 maggio – 2 giugno 2017, © Springer International Publishing

AG 2017, vol.2, set 2, pp. 899-907, https://doi.org/10.1007/ 978-3-319-53498-5_102, ISBN: 978-3-319-53497-8.

Nicodemo G., Peduto D., Ferlisi S., Maccabiani J. (2017b) Investigating building settlements via very high resolution SAR sensors. In: Bakker, Frangopol, van Breugel (eds) Life-Cycle of Engineering Systems: Emphasis on Sustainable Civil Infrastructure. Taylor & Francis Group, London, pp 2256–2263 ISBN 978-1-138-02847-0.

Nicodemo G., Peduto D., Ferlisi S., Gullà G., Borrelli L., Fornaro G. & Reale D. (2017). Analysis of building vulnerability to slow-moving landslides via A-DInSAR and damage survey data. In Workshop on World Landslide Forum (pp. 899-907). Springer, Cham.

Nicodemo G., Peduto D., Ferlisi S., Gullà G., Reale D., & Fornaro G. (2018, July). Dinsar data integration in vulnerability analyses of buildings exposed to slow-moving landslides. In IGARSS 2018-2018 IEEE International Geoscience and Remote Sensing Symposium (pp. 6107-6110). IEEE.

Nova, R., Castellanza, R., & Tamagnini, C. (2003). A constitutive model for bonded geomaterials subject to mechanical and/or chemical degradation. International Journal for Numerical and Analytical Methods in Geomechanics, 27(9), 705-732.

Olivares L., & Picarelli L. (2006, July). Modelling of flowslides behaviour for risk mitigation. In Proc 6th Int Conf on Physical Modelling in Geotechnics. Hong Kong (Vol. 1, pp. 99-112).

Palmisano F., Vitone C., Cotecchia F., (2016). Landslide damage assessment at the intermediate to small scale. Aversa et al. (eds.), Landslides and Engineered Slopes Experience, Theory and Practice, Vol. 1, pp. 1549-1557.

Pastor, M., Blanc, T., & Pastor, M. J. (2009). A depth-integrated viscoplastic model for dilatant saturated cohesive-frictional fluidized mixtures: application to fast catastrophic landslides. Journal of Non-Newtonian Fluid Mechanics, 158(1-3), 142-153.

Pecoraro, G., Calvello, M., & Piciullo, L. (2019). Monitoring strategies for local landslide early warning systems. Landslides, 16(2), 213-231.

Peduto D., Cascini L., Arena L., Ferlisi S., Fornaro G., Reale D. (2015). A general fremework and related procedures for multi scale analyses of DInSAR

data in subsiding urban areas. ISPRS Journal of Photogrammetry and Remote Sensing, Vol. 105: 186-210, ISSN 0924-2716, http://dx.doi.org/10.1016/j.isprsjprs.2015.04.001.

Peduto D, Borrelli L, Antronico L, Gullà G, Fornaro G (2016). An integrated approach for landslide characterization in a historic centre. In: Aversa S, Cascini L, Picarelli L, Scavia C (eds) Landslides and engineered slopes. Experience, theory and practice. Proc of the 12th Int Symp on Landslides, vol 3. CRC Press, Balkema, pp 1575–1581. https://doi.org/10.1201/b21520-195.

Peduto D, Nicodemo G, Maccabiani J, Ferlisi S (2017a) Multi-scale analysis of settlementinduced building damage using damage surveys and DInSAR data: a case study in The Netherlands. Eng Geol 218:117–133.

Peduto D, Ferlisi S, Nicodemo G, Reale D, Pisciotta G, Gullà G (2017b) Empirical fragility and vulnerability curves for buildings exposed to slow-moving landslides at medium and large scales. Landslides 14(6):1993–2007.

Peduto D., Santoro M., Aceto L., Borelli L. and Gullà G. (2021). Full integration of geomorphological, geotechnical, A-DInSARa and damage data for detailed geometric-kinematic features of a slow-moving landslide in urban area. Landslides. DOI10.1007/s10346-020-01541-0.

Peduto D, Elia F, Montuori R (2018a) Probabilistic analysis of settlement-induced damage to bridges in the city of Amsterdam (The Netherlands). Transport Geotech 14:169– 182. https://doi.org/10.1016/j.trgeo.2018.01.002.

Peduto D, Nicodemo G, Caraffa M, Gullà G (2018b) Quantitative analysis of consequences to masonry buildings interacting with slow-moving landslide mechanisms: a case study. Landslides 15(10):2017–2030.

Peduto D, Korff M, Nicodemo G, Marchese A, Ferlisi S (2019a) Empirical fragility curves for settlement-affected buildings: analysis of different intensity parameters for seven hundred masonry buildings in The Netherlands. Soils Found 59(2):380–397. https://doi.org/10.1016/j.sandf.2018.12.009.

Pellegrino A., Ramondini M., Urciouli G. (2004). Interplay between the morphology and mechanism of mudslides: field experiences from Southern Italy. Lacerda W. (eds.), Proceedings of the 9th International Symphosium on Landslides, Rio de Janeiro, Vol.2 Balkema, Rotterdam, pp. 1403-1409.

Petley D. N., Mantovani F., Bulmer M. H. & Zannoni A. (2005). The use of surface monitoring data for the interpretation of landslide movement patterns. Geomorphology, 66(1-4), 133-147.

Petley D. N. (2012). Global patterns of loss of life from landslides. Geology, 40(10), 927–930.

Plank S, Singer J, Minet Ch, Thuro K (2010) GIS based suitability evaluation of the differential radar interferometry method (DInSAR) for detection and deformation monitoring of landslides, in: Proceedings of Fringe 2009 Workshop, edited by: Lacoste- Francis, H., 30 November–4 December 2009, ESRIN, Frascati, Italy (ESA SP- 677), 8 pp., ISBN: 978-92-9221- 41-4, 2010.

Remondo J., Bonachea J., & Cendrero A. (2005). A statistical approach to landslide risk modelling at basin scale: from landslide susceptibility to quantitative risk assessment. Landslides, 2(4), 321-328.

Remondo J., Bonachea J., & Cendrero A. (2008). Quantitative landslide risk assessment and mapping on the basis of recent occurrences. Geomorphology, 94(3-4), 496-507.

Rosen, P. A., Hensley, S., Joughin, I. R., Li, F. K., Madsen, S. N., Rodriguez, E., & Goldstein, R. M. (2000). Synthetic aperture radar interferometry. Proceedings of the IEEE, 88(3), 333-382.

Rocca F. (2003) 3D motion recovery with multi-angle and/or left right Interferometry. In: Proceedings 3rd international workshop on ERS SAR interferometry, FRINGE 2003, Frascati, 2–5 Dec 2003. ESA SP-550.

Rott H., Scheuchl B., Siegel A., Grasemann B. (1999). Monitoring very slow slope movements bt means of SAR interferometry: A case study from a mass waste above a reservoir in the Ötztal Alps, Austria. Geophysical Research Letters, 26(11): 1629–1632.

Sorriso-Valvo M, Sylvester AG (1993) The relationship between geology and landforms along a coastal mountain front, northern Calabria, Italy. Earth Surf Process Landf 18(3):257–273.

Stramondo S., Bozzano F., Marra F., Wegmuller U., Cinti F.R., Moro M., Saroli M. (2008). Subsidence induced by urbanisation in the city of Rome detected by advanced InSAR technique and geotechnical investigations. Remote Sensing of Environment, 112:3160–3172, doi:10.1016/j.rse.2008.03.008.

Terranova C., Vilardo G., Bellucci Sessa E., Pepe M., & Ventura G. (2011). Analisi multitemporale (2006-2010) di dati LiDAR da aereo sulla frana attiva di Montaguto (AV). Geoitalia.

The Institution of Structural Engineers, (1994). Subsidence of low rise buildings. The Institution of Structural Engineers, London, pp. 106.

Tofani V., Raspini F., Catani F., Casagli N. (2014). Persistent scatterer interferometry (PSI) technique for landslide characterization and monitoring. In: Sassa, K., Canuti, P., Yueping, Y. (Eds.), Landslide Science for a Safer Geoenvironment, Vol. 2: Methods of Landslide Studies. Springer International Publishing. ISBN: 9783319050492, pp. 351– 357.

Tofani V, Raspini F, Catani F, Casagli N (2013) Persistent Scatterer Interferometry (PSI) technique for landslide characterization and monitoring. Remote Sens 5(3):1045–1065

Tommasi P., Pellegrini P., Boldini D., Ribacchi R. (2006). Influence of rainfall regime on hydraulic conditions and movement rates in the overconsolidated clayey slope of the Orvieto hill (central Italy). Canadian Geotechnical Journal, 43:70-86.

Trigila A., Iadanza C., Bussettini M., & Lastoria B. (2018). Dissesto idrogeologico in Italia: Pericolosità e indicatori di Rischio—Edizione 2018. Ispra, Rapporti, 287, 2018.

Van Rooy J.L., (1989). A proposed classification system for dolomitic areas south of Pretoria. Contributions to Engineering Geology, 1:57-65.

Van Westen, C. J., Van Asch, T.W. J., & Soeters, R. (2006). Landslide hazard and risk zonation — why is it still so difficult? Bulletin of Engineering Geology and Environment, 65, 167–184.

Van Westen C. J., Castellanos E., & Kuriakose S. L. (2008). Spatial data for landslide susceptibility, hazard, and vulnerability assessment: An overview. Engineering geology, 102(3-4), 112-131.

Van Westen, C. J. (2004). Geo-information tools for landslide risk assessment: an overview of recent developments. Landslides Eval Stab, 1, 39-56.

Varnes D. J. (1984). Landslide hazard zonation: a review of principles and practice (No. 3).

Vilardo G., Ventura G., Terranova C., Matano F. and Nardo S. (2009). Ground deformation due to tectonic, hydrothermal, gravity, hydrogeological, and anthropic processes in the Campania Region (Southern Italy) from permanent scatterers synthetic aperture radar interferometry. Remote Sensing of Environment, 113:197–212.

Viscardi A., (2010). PhD Thesis of University of Salerno. Tutor: Prof. Ing. Cascini L., Co-tutor: Ferlisi S.

Wasowski J, Pisano L (2019) Long-term InSAR, borehole inclinometer, and rainfall records provide insight into the mechanism and activity patterns of an extremely slow urbanized landslide. Landslides 17:445–457. https://doi.org/10.1007/s10346- 019-01276-7.

Wasowski J, Bovenga F, Nutricato R, Nitti DO, Chiaradia MT (2017) High resolution satellite multi-temporal interferometry for monitoring infrastructure instability hazards. Innov Infrastruc Solut 2(1):27.

Wood, H. O., & Neumann, F. (1931). Modified Mercalli intensity scale of 1931. Bulletin of the Seismological Society of America, 21(4), 277-283.